

NEUTRON SPIN-PENDELLÖSUNG RESONANCE

by

Kenneth David Finkelstein

B.S., Physics

S.U.N.Y. at New Paltz

(1977)

**Submitted in Partial Fulfillment of
the Requirements for the Degree of
Doctor of Philosophy
at the**

Massachusetts Institute of Technology

September, 1987

© Massachusetts Institute of Technology 1987

Signature of Author_____

Department of Physics, September 1987

Certified by_____

Clifford G. Shull

Thesis Supervisor

Accepted by_____

George F. Koster

Chairman, Department Graduate Committee

**MASSACHUSETTS INSTITUTE
OF TECHNOLOGY**

JUL 29 1987

LIBRARIES

This Thesis is dedicated
to the memory of a friend and colleague
Brian Cohen.

Neutron Spin-Pendellösung Resonance

ABSTRACT

The Spin-Orbit (or SO) interaction is known to produce only a very weak contribution to the scattering of thermal neutrons. In this thesis, novel effects due to SO scattering are studied by diffraction in a perfect crystal. Schwinger proposed this type of interaction in the case of high energy neutron-nuclear scattering. He suggested that the neutron would sense the atomic electric field by the (SO) interaction between the neutron magnetic moment and the magnetic field due to its motion. It is demonstrated here, using unpolarized thermal neutron, that SO effects, which are usually 4 orders smaller than those of the nuclear interaction, may be resonantly coupled with nuclear scattering in the pendellösung phenomenon of dynamical (perfect crystal) diffraction.

On the theoretical side we have included the Schwinger scattering contribution in the description of the crystal potential as it is used in the equations of dynamical diffraction. It is found that under appropriate conditions, a dramatic enhancement of the effects of SO scattering occurs when an external magnetic field is applied to the diffracting neutron. In the experimental component of this work, we demonstrate this enhancement by performing a resonance experiment in which there is observed a large change in pendellösung oscillation intensity with changes in applied magnetic field. From these measurements we obtain a more precise value for the strength of SO scattering than has been previously possible.

Thesis Supervisor: Dr. Clifford Shull

Title: Professor of Physics

Table of Contents

CHAPTER I-Introduction to Neutron Spin-Pendellösung Resonance	6
References	10
CHAPTER II-A Review of the Concepts Leading to NSPR	11
Section (2.1)-Diffraction with Plane Wave Illumination	12
(2.1.1)-Dynamical Diffraction in a Nuclear Lattice	12
(2.1.2)-The Type 1 Solutions to the T.T. Equations	17
(2.1.3)-The Type 2 Solutions to the T.T. Equations	26
Section (2.2)-Diffraction with Point Source Illumination	31
Section (2.3)-The Crystal Potential	38
(2.3.1)-The Neutron-Nuclear Crystal Potential	38
(2.3.2)-The Spin-Orbit Potential of the Lattice	42
Appendix	56
Section (2.4)-Experimental Antecedents to NSPR	47
(2.4.1)-Neutron Pendellösung Fringe Measurements	47
(2.4.2)-Spin-Orbit Scattering of Slow Neutrons	53
References	60
CHAPTER III-Neutron Spin-Pendellösung Resonance	61
Section (3.1)-Introductory Concepts of NSPR	61
Section (3.2)-Dynamical Diffraction Description of NSPR	64
Appendix	87
Section (3.3)-The NSPR Wavefunction; Predictions of Resonant Behavior	72
Section (3.4)-An Alternative Derivation of NSPR Theory	79
References	90

CHAPTER IV-The Experimental Investigation of NSPR	91
Section (4.1)-Necessary Conditions for Observation of NSPR	93
(4.1.1)-Considerations in Controlling Pendellösung Phase	93
(4.1.2)-Requirements on Controlling the Magnetic Field	98
Section (4.2)-The NSPR Experimental Arrangement	104
(4.2.1)-The Spectrometer System	107
(4.2.2)-The Magnet and Magnet Control System	109
(4.2.3)-The Temperature Control System	113
References	116
CHAPTER V-Results of Experimental Study	117
Section (5.1)-Pendellösung Fringe Measurements	119
Section (5.2)-NSPR Field Scanning Results	121
Section (5.3)-Quantitative Analysis of NSPR Data	124
References	130
CHAPTER VI-Summary	131
Acknowledgements	134
Biographical Note	135

Chapter I - Introduction to Neutron Spin-Pendellösung Resonance

In this thesis is presented a description and as well the results from measurements of a new phenomenon in neutron scattering called Neutron Spin-Pendellösung Resonance (NSPR). This effect occurs when an external magnetic field is used to couple interactions between a neutron and a perfect crystal. The two interactions involved are, the short ranged neutron-nuclear interaction, and second the interaction between the neutron magnetic moment and the electric field of an atom which is known as the neutron spin-neutron orbit interaction.

The description of NSPR to be discussed here is an extension of a theory used to predict the behavior of neutrons diffracting in crystals with perfect periodic structure. This extension is itself a reformulation of the better known dynamical diffraction theory for x-rays. This theory, formulated by Darwin [1], Ewald [2], and von Laue [3] in the early part of this century has been reviewed more recently by James [4] and Batterman and Cole [5]. The theory accounts for the electromagnetic interaction of scattered waves in crystals with one another and with the lattice itself. An important contribution to the x-ray theory was made by Kato [6] who developed a spherical wave approach to diffraction and extended the important notion of pendellösung oscillations well beyond its original definition due to Ewald. The latter author had observed that solutions to the equations of

dynamical diffraction bear striking similarity to the normal mode solutions associated with coupled pendula in classical mechanics, thus the name pendellösung.

The first formulation of neutron dynamical diffraction, in which it is the nuclear force that mediates in the scattering process, was given by Goldberger and Seitz [7]. On the experimental side, the definitive studies of pendellösung oscillations were carried out by Shull [8] and it is these investigations that provide a foundation for the present experimental work.

In a realm generally considered far removed from the perfect crystal physics of pendellösung is found the idea of a spin-orbit contribution to the scattering of thermal neutrons. Schwinger [9] proposed that the spin-orbit (SO) interaction should play a part in neutron-nuclear scattering. That is, in scattering by a nucleus, the neutron travels through the atomic electric field and thus senses, by way of its magnetic moment, the magnetic field due to its motion. The resulting contribution of SO scattering to the total scattered intensity is expected to be about four orders smaller than the nuclear component. A good, physical treatment of SO scattering for the case of high energy protons has been given by Fermi [10]. It was not until 1963 when Shull [11] carried out a series of measurements using mosaic (imperfect) crystals, that this effect was demonstrated to exist in slow neutron scattering.

This thesis makes a synthesis between SO scattering and dynamical neutron diffraction. On the theoretical side we have

included the Schwinger scattering contribution in the description of the crystal potential as it is used in the equations of dynamical diffraction. It is found that under appropriate conditions, a dramatic enhancement of the effects of SO scattering occur when an external magnetic field is applied to the diffracting neutron. In the experimental component of this work, we demonstrate the enhancement by performing a resonance experiment in which there is observed a large change in pendellösung oscillation intensity with changes in applied magnetic field. From these measurements we obtain a more precise value for the strength of SO scattering than has been previously possible.

Before proceeding with our treatment of these subjects it is worth outlining the presentation that follows. Chapter II, broken into four sections, is simply a review of the features of dynamical diffraction that are relevant to this study. In the last section of this chapter we review two experiments that to a great extent have motivated the present work. Chapter III is new material; the formal description of NSPR is presented as well as (in the last section) an alternative derivation of the formal results. This alternative picture is especially useful in that it provides insight into the physics underlying the NSPR effects. In Chapter IV the principal considerations that go into designing an experiment to measure this effect are outlined. The results of measurements performed using a silicon crystal and 1Å wavelength unpolarized neutrons are reported in Chapter V. One of the results given is a measurement of the ratio of SO to

nuclear scattering and this value is compared to the results of a first principles calculation based on the charge density of the silicon atom. Finally Chapter VI summarizes the presentation given in the previous chapters.

Because of a limitation in the word processing system used to prepare this document it was necessary to represent Planck's constant as h when numerically it should be $\hbar/2\pi$.

End Notes

1. C.G. Darwin, Phil. Mag. [6] **27**, 315, 675, (1914).
2. P.P. Ewald, Ann. Physik [4] **49**, 1, 117 (1916); **54**, 159 (1917).
3. M. von Laue, Ergeb.Exact.Naturw. **10**, 133 (1931).
4. R.W. James, Solid State Phys. **15**, 53 (1963).
5. B.W. Batterman, H. Cole, Rev. Mod. Phys. **36**, 681 (1964).
6. N. Kato, Acta Cryst. **14**, 526, 627 (1969).
7. M.L. Goldberger, F. Seitz, Phys. Rev. **71**, 294 (1947).
8. C.G. Shull, Phys. Rev. Lett. **21**, 1585 (1968).
9. J. Schwinger, Phys. Rev. **73**, 407 (1948).
10. E. Fermi, IL Nuovo Cimento Series 10, Supple. 2 (1955).
11. C.G. Shull, Phys. Rev. Lett. **10**, 297 (1963).

Chapter 2 - A Review of the Concepts Leading to NSPR

The present chapter reviews the description of neutron diffraction in perfect crystals by presenting dynamical diffraction theory from a point of view in which the neutron-crystal interaction potential is primary. The discussion begins with what is often called the "plane wave" theory. This name comes from the tradition of assuming that it is the nature of the waves incident at the boundary of the crystal that defines the mathematical description of the diffraction process [1]. However, the formulation of dynamical diffraction presented here does not refer to boundary conditions in deriving the equations of diffraction and thus the formalism can be applied with greater ease to a variety of experimental situations. The important results of this first (plane wave) section come with the description of pendellösung phenomena and here they are seen to result from plane wave excitation of the crystal.

The second section of this chapter discusses the in-crystal effects caused by point source illumination on the crystal face. Many authors refer to this subject as "spherical wave" theory. Again, it is pendellösung oscillation effects that are emphasized in our treatment, and this is because it is necessary to observe such oscillations before one can attempt to detect the action of NSPR.

In the third section it is the features of the interaction potential energy felt by the neutron in the NSPR process that

are presented. The final section of the chapter reviews two experiments that predate the present work and that provide at least partial motivation for our study.

Section 2.1.1 - Dynamical Diffraction in a Nuclear Lattice

We now begin our study of the quantum mechanical description for wave propagation in perfect crystals. Assume that the neutron (plane wave) outside the crystal has associated with it a total energy E , typically about 1/40 electron volt (eV) and propagation vector \vec{k} . The crystal will be thought of as a periodic potential and is expanded in a Fourier series in the reciprocal lattice vectors \vec{c} . A detailed discussion of this view of the crystal will be presented in Section (2.3). At present it is sufficient to state that the magnitudes of the Fourier potential coefficients range in size between 10^{-8} and 10^{-10} eV.

The Schrödinger equation (SE) is written

$$\left(-\frac{\hbar^2}{2m} \nabla^2 + V(\vec{r}) - E \right) \psi(\vec{r}) = 0. \quad (2.1.1)$$

The following definitions are used to simplify the notation and introduce the periodic potential.

$$k^2 = \frac{2mE}{\hbar^2} \quad , \quad v(\vec{r}) = 2m \frac{V(\vec{r})}{\hbar^2} \quad , \quad v(\vec{r}) = \sum_{\vec{G}'} v_{\vec{G}'} e^{i\vec{G}' \cdot \vec{r}}. \quad (D2.1.1)$$

The solutions of (2.1.1) that are appropriate in this discussion are in the form of expansions in plane waves,

$$\psi(\vec{r}) = \sum_{\vec{G}} a_{\vec{G}}(\vec{r}) e^{i(\vec{K} + \vec{G}) \cdot \vec{r}} \quad (2.1.2)$$

where the plane wave amplitude $a_{\vec{G}}(\vec{r})$ is a function of position in the crystal. It is further assumed that these amplitudes vary slowly on the scale of the neutron wavelength (about 1Å). \vec{K} is a wave vector in the crystal which satisfies Bragg's law exactly; it is defined in Fig.(2.1). Substitution of (D2.1.1) and (2.1.2) into (2.1.1) yields

$$\sum_{\vec{G}'} \left\{ \left[\left(-(\vec{K} + \vec{G})^2 + \nabla^2 + k^2 \right) a_{\vec{G}}(\vec{r}) + 2i\vec{\nabla} a_{\vec{G}}(\vec{r}) \cdot (\vec{K} + \vec{G}) \right] e^{i(\vec{K} + \vec{G}) \cdot \vec{r}} - \sum_{\vec{G}'} v_{\vec{G}'}(\vec{r}) e^{i(\vec{K} + \vec{G} + \vec{G}') \cdot \vec{r}} \right\} = 0. \quad (2.1.3)$$

If $a(\vec{r})$ varies slowly, then $\nabla^2 a(\vec{r})$ will be small in magnitude relative to the other terms in the square brackets and can be ignored [2]. It can be shown that these plane waves are orthogonal and this implies that coefficients of each plane wave component separately equal zero [3]. It follows that

$$\left[-a_0 K^2 + 2i\vec{\nabla} a_0 \cdot \vec{K} - \sum_{\vec{G}'} v_{\vec{G}'} a_{-\vec{G}'} + k^2 a_0 \right] e^{i\vec{K} \cdot \vec{r}} = 0 \quad (2.1.4)$$

$$\left[-a_{\vec{G}_1} (\vec{K} + \vec{G}_1)^2 + 2i\vec{\nabla} a_{\vec{G}_1} \cdot (\vec{K} + \vec{G}_1) - \sum_{\vec{G}'} v_{\vec{G}'} a_{\vec{G}_1 - \vec{G}'} + k^2 a_{\vec{G}_1} \right] e^{i(\vec{K} + \vec{G}_1) \cdot \vec{r}} = 0$$

where \vec{G}_1 is any $\vec{G} \neq 0$.

A great simplification results when we consider the case of diffraction occurring from only one set of diffracting planes (one \vec{G}). In this case only two amplitude functions, a_0 and a_c , are of appreciable size. The coupled set of differential equations becomes

$$(-K^2 - v_0 + k^2) a_0(\vec{r}) + 2i\vec{\nabla} a_0 \cdot \vec{K} - v_{-c} a_c(\vec{r}) = 0 \quad (2.1.5)$$

$$(-(\vec{K} + \vec{G})^2 - v_0 + k^2) a_c(\vec{r}) + 2i\vec{\nabla} a_c \cdot (\vec{K} + \vec{G}) - v_c a_0(\vec{r}) = 0.$$

The equation (2.1.5) can be simplified by defining $K^2 \equiv -v_0 + k^2$. This definition links the magnitude of the vector \vec{K} with the total energy of the neutron and the mean crystal potential parameter $v(0) = \frac{2mV(0)}{h^2}$.

Given the size of $V(0)$ (see (2.3.2)) this implies that the magnitudes of the two vectors \vec{k} and \vec{K} differ by about one part in 10^4 . The final form of (2.1.5) is thus written

$$i\vec{\nabla}a_0 \cdot \vec{K} - \frac{v-c}{2}a_c(\vec{r}) = 0$$

(2.1.6)

$$i\vec{\nabla}a_c \cdot (\vec{K} + \vec{G}) - \frac{v_c}{2}a_0(\vec{r}) = 0.$$

This first order pair of coupled differential equations is known as the Taupin-Tagaki (T.T.) equations[4]. The two vectors \vec{K} (forward) and $\vec{K} + \vec{G}$ (Bragg direction) define a "plane of scattering" and restrict the amplitude functions to be dependent on only two spatial variables. In Fig.(2.1) the geometry which will be used in discussing wave solutions inside the crystal is illustrated.

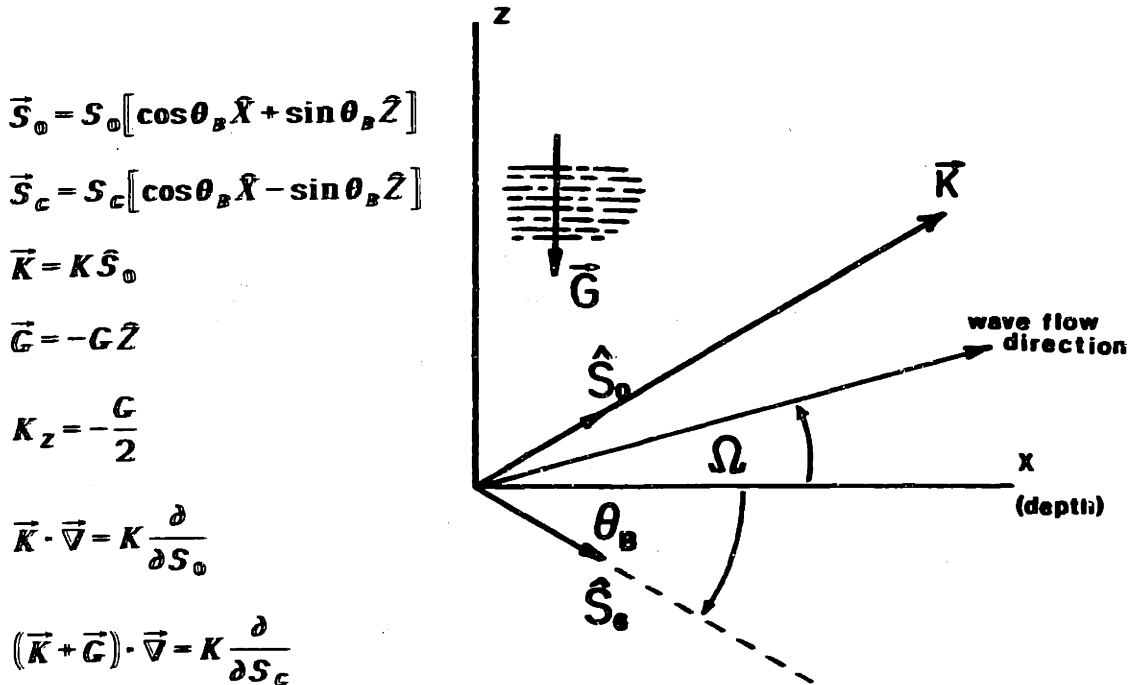


Fig.(2.1) Crystal coordinate system used in describing the 2-beam neutron wave solutions of the T.T. equations. The Z-axis points anti-parallel to the reciprocal lattice vector and the X-axis points into the crystal depth. The origin corresponds to an entrance point on the crystal surface. Both the Bragg angle and the angle of wave flow Ω are indicated, as are the oblique coordinates S_0 , S_c .

There are three types of functions that are useful as solutions for (2.1.6): 1) complex exponential, 2) trigonometric, and 3) Bessel functions. Before proceeding to discuss type 1) solutions a comment about the nature of the potential coefficients is in order. In general these coefficients can be complex, representing the effects of crystal symmetry, and beam attenuation as well as purely coherent nuclear (real) scattering. For our purposes it is appropriate to restrict the generality of the form of the coefficients by defining the potential parameter $v_{\pm c} = |v_c| e^{\pm i2\alpha}$.

With this definition (2.1.6) may be written

$$ie^{i\alpha} \frac{\partial}{\partial S_0} a_0(\vec{r}) - \frac{|v_c|}{2K} e^{-i\alpha} a_c(\vec{r}) = 0 \quad (2.1.7)$$

$$ie^{-i\alpha} \frac{\partial}{\partial S_c} a_c(\vec{r}) - \frac{|v_c|}{2K} e^{+i\alpha} a_0(\vec{r}) = 0.$$

Section 2.1.2 - The type 1 Solutions for the T.T. Equations

A particular solution of (2.1.7) is

$$a_0(\vec{r}) = e^{-i\frac{A}{2}\left(RS_0 + \frac{S_G}{R}\right) + i(\phi - \alpha)} \quad (2.1.8)$$

$$a_G(\vec{r}) = R e^{-i\frac{A}{2}\left(RS_0 + \frac{S_G}{R}\right) + i(\phi + \alpha)}$$

where R is a parameter to be determined, and $A = \frac{|v_G|}{K} \sim 10^{-6}k$.

By re-writing (2.1.8) using the coordinates (X,Z) one finds that the 2-beam wavefunction (2.1.2) is

$$\Psi(\vec{r}) = e^{-i\frac{A}{2}\left[\frac{Z}{\sin\theta_B}\left(R - \frac{1}{R}\right) + \frac{X}{\cos\theta_B}\left(R + \frac{1}{R}\right)\right] + i\phi} \left\{ e^{i\vec{K}\cdot\vec{r}} + R e^{i(\vec{K}+\vec{G})\cdot\vec{r}} \right\} \quad (2.1.9)$$

where α has been absorbed into the parameter R.

Note that R is the magnitude of the ratio of the two plane wave components of $\Psi(\vec{r})$. It is important to understand what (2.1.9) tells us about the neutron wave "flow" and probability distribution in the crystal. By setting $\alpha=0$, we make R real; normalization of the wavefunction over a volume (U) containing an integral number of unit cells gives

$$\Psi(\vec{r}) = \frac{1}{\sqrt{U}\sqrt{1+R^2}} \alpha_0(\vec{r}) \left\{ e^{i\vec{K}\cdot\vec{r}} + R e^{i(\vec{K}+\vec{G})\cdot\vec{r}} \right\}. \quad (2.1.10)$$

Now (2.1.10) is used to calculate the expectation value of the momentum defined as $\langle \vec{P} \rangle = -i\hbar \langle \Psi | \vec{\nabla} | \Psi \rangle$.

This calculation yields

$$\langle \vec{P} \rangle = \hbar \left\{ \vec{K} + \left(1 + \frac{1}{R^2} \right)^{-1} \vec{G} \right\}$$

If Ω is defined as the angle of wave flow relative to the crystal planes (see Fig.(2.1)) we may define

$$\tan \Omega = \frac{\langle P_z \rangle}{\langle P_x \rangle} = \frac{K_z - \left(1 + \frac{1}{R^2} \right)^{-1} G}{K_x} \quad (D.2.1.2).$$

Again referring to Fig.(2.1) and using the definition of \vec{K} given in that figure one may obtain the relation between Ω and R namely

$$\tan \Omega = \tan \theta_B \left\{ \frac{1 - R^2}{1 + R^2} \right\}.$$

We now define a trajectory parameter Γ as

$$\Gamma = -\frac{\tan \Omega}{\tan \theta_B} = \frac{R^2 - 1}{R^2 + 1}. \quad (D2.1.3)$$

The relationship between Γ and R is then written

$$R = \pm \sqrt{\frac{1 + \Gamma}{1 - \Gamma}}.$$

Two points about these relations are worth noting.

1) R is a doubled valued function of Γ . For a single flow direction Γ there are two values of R (two amplitude ratios for the wavefunction).

2) For R to be real and finite it must be true that $|\Gamma| \leq 1$. This condition then implies that $|\tan \Omega| \leq |\tan \theta_B|$.

Thus this solution has wave flow direction relative to the lattice planes which may not exceed the angle θ_B .

We shall now turn our attention to the overall amplitude function in (2.1.10), i.e. $a_0(\vec{r})$. We write the wavefunction out to display the 2-dimensional nature of the wave vectors.

$$\psi(\vec{r}) = \frac{1}{\sqrt{U}\sqrt{1+R^2}} e^{-i(\Delta K_X X + \Delta K_Z Z) + i\phi} \left\{ e^{i\vec{K} \cdot \vec{r}} + R e^{i(\vec{K} + \vec{C}) \cdot \vec{r}} \right\} \quad (2.1.11)$$

where referring to (2.1.9) we see that

$$\Delta K_z = -\frac{A(R - 1/R)}{4\sin\theta_B}$$

$$\Delta K_x = -\frac{A(R + 1/R)}{4\cos\theta_B}.$$

These wave vector increments add to the wavevectors in the forward and Bragg directed plane waves of the wavefunction (2.1.11). It is clear that the magnitude of the increments change depending on the neutron trajectory since R does. It will be convenient to introduce a new parameter y , the meaning of which will soon be made clear. Let

$$2y = R - 1/R \quad \text{which implies} \quad R = y \pm \sqrt{y^2 + 1}. \quad (D2.1.4)$$

In terms of this parameter y , the wavevector increments are

$$\Delta K_z = -\frac{A}{2\sin\theta_B} y$$

$$\Delta K_x = \mp \frac{A}{2\cos\theta_B} \sqrt{y^2 + 1}.$$

Eliminating y between these two quantities leads to the well known dispersion hyperbola (or dispersion surface) of dynamical diffraction.

$$\frac{\frac{\Delta K_x^2}{\Lambda^2}}{2 \cos \theta_B} - \frac{\frac{\Delta K_z^2}{\Lambda^2}}{2 \sin \theta_B} = 1 \quad (2.1.12)$$

For consistency with the geometry of Fig.(2.1) we draw this dispersion hyperbola, in Fig.(2.2), centered on the tip of the wavevector \vec{k} in K-space. An identical hyperbola will exist centered at $\vec{k} + \vec{G}$ which we will not discuss further. This hyperbola defines all the wavevectors that are associated with solutions (of this type) to equation (2.1.7) for a fixed energy E.

In the following discussion we consider a solution to the diffraction problem which corresponds to a single point (known as a tie point) on the hyperbola and refer to the hyperbola in emphasizing some important features of such a solution.

a) The scale of the wavevector increment $\Delta \vec{k}$ relative to the wavevector \vec{k} is indicated at the bottom of the figure. It is seen that in ranging widely over the hyperbola a change in the wavevector of only a few parts in 10^4 will occur.

b) The surface is composed of two branches. Wavevectors terminating on the left side branch, called the β branch, are shorter than the central vector \vec{k} . On the right, or α branch, they are longer than \vec{k} . Another way to say this is, β solution neutrons have associated with them a smaller kinetic energy than do α solution neutrons.

c) From the relation between y and the wavevector increments, it is seen that the y -parameter axis points along the $-\Delta K_z$.

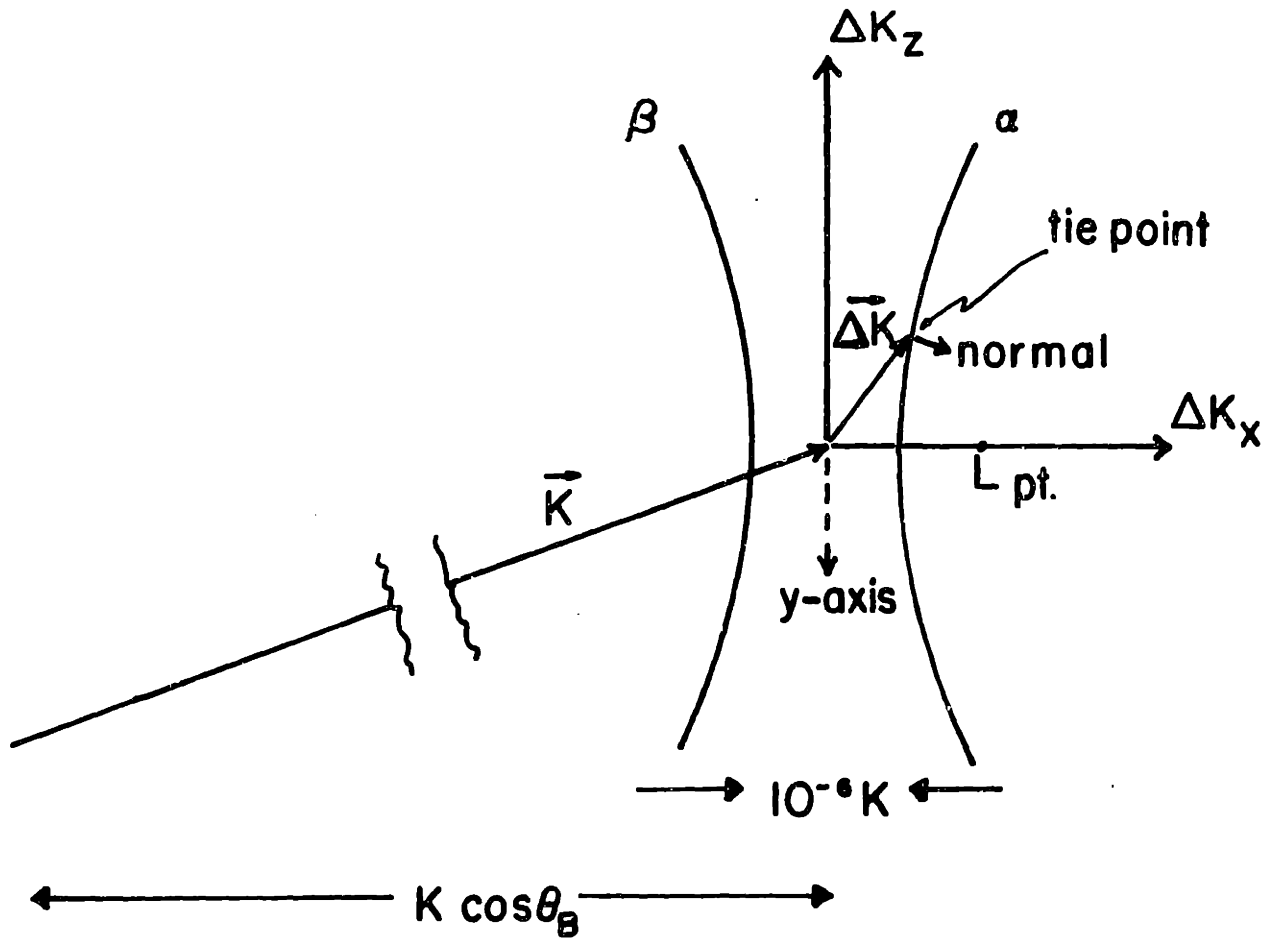


Fig.(2.2) The dispersion hyperbola, in reciprocal space, that represents all plane wave solutions of the T.T. equations. The center point is located by the tip of the wavevector K while the two branches α and β are separated along the diameter by about $10^{-6}K$.

direction in the figure. For a given value of y there are two associated tie points, one on each branch.

d) Using (D2.1.4), one finds an important relationship between a tie point and the relative amplitudes of the two plane wave components of the corresponding solution.

For the α branch: $R = y + \sqrt{y^2 + 1}$.

Therefore as y increases (above zero) R gets larger, thus we expect Bragg directed radiation to dominate in the solution.

For the β branch: $R = y - \sqrt{y^2 + 1}$.

In this case as y increases (above zero) R gets smaller, thus we expect forward directed radiation to be dominant. For y less than zero the behavior described above is reversed. In the limit of very large $|y|$ it can be shown that these solutions become those expected for undiffracted radiation.

Two analytical properties of the hyperbola lead to interesting physical predictions.

e) The first result was pointed out by Ewald[5] and by Kato [6]. It is that the normal to the hyperbola, for any tie point, points in the direction of the neutron (wave) trajectory corresponding to that solution. This is easy to show using (2.1.12). The slope of the normal at a point is:

$$-\left(\frac{\partial \Delta K_x}{\partial \Delta K_z}\right)^{-1} = \tan \theta_B \frac{y}{\pm \sqrt{y^2 + 1}} \quad (2.1.13)$$

$$= \pm \tan \Omega.$$

The significance of the asymptotes is now made clear; the normal to the asymptotes point in the limiting direction of wave flow, that is in the undiffracted directions given by \vec{K} and $\vec{K} + \vec{G}$.

f) Another property is the curvature of the hyperbola; it is a measure of the rate of change of the neutron trajectory with respect to changes in ΔK_z . Taking the derivative with respect to ΔK_z on both sides in (2.1.13) leads to

$$d\Gamma = \pm (1 + y^2)^{-\frac{3}{2}} dy.$$

Using (D2.1.2,3,4) one finds

$$d\langle P_z \rangle = \pm (1 - y^2)^{-\frac{3}{2}} 2h \sin^2 \theta_B \left(\frac{E}{V_G} \right) d(\Delta K_z).$$

Let us assume the change $d(\Delta K_z)$ is due to a force applied to the neutron, and use the following relation [7] to relate this force to the time (T) derivative of $\Delta \vec{K}$.

$$\vec{F} = h \frac{d\vec{K}}{dT}.$$

One then finds using the relation between expectation values for acceleration and momentum, $\langle \vec{a} \rangle = \frac{1}{m} \frac{d\langle \vec{P} \rangle}{dT}$,

$$\langle a_z \rangle = \pm \frac{2 \sin^2 \theta_B}{m} \left(\frac{E}{V_G} \right) [1 + y^2]^{-\frac{3}{2}} F_z = \frac{F_z}{m^*}.$$

This last expression can be considered a form of Newton's second law for neutrons diffracting in a perfect crystal. It says that these neutrons behave as though their mass were reduced (as compared to the free space value) by a factor of as much as a million! Furthermore, this "effective mass" has two signs, one associated with each branch of the hyperbola. Experiments have been carried out which demonstrate this greatly enhanced acceleration [8].

The last feature of these (single tie point) solutions to be discussed, is the distribution of probability density in the lattice. Using (2.1.10) again with $\alpha=0$, we find

$$|\Psi(\vec{r})|^2 = \frac{1}{U} \left\{ 1 + \left(\frac{2R}{1+R^2} \right) \cos \frac{2\pi z}{d} \right\}$$

where d is the distance between diffracting planes. Because R is double-valued (see (D2.1.3)) this expression has two values; one corresponding to each branch of the hyperbola. We plot the two probability density functions (for $y=0$) in Fig.(2.3).

Note that the α solution has maximum probability halfway between lattice planes; the β solution is peaked on these planes. An earlier comment on the kinetic energy (or

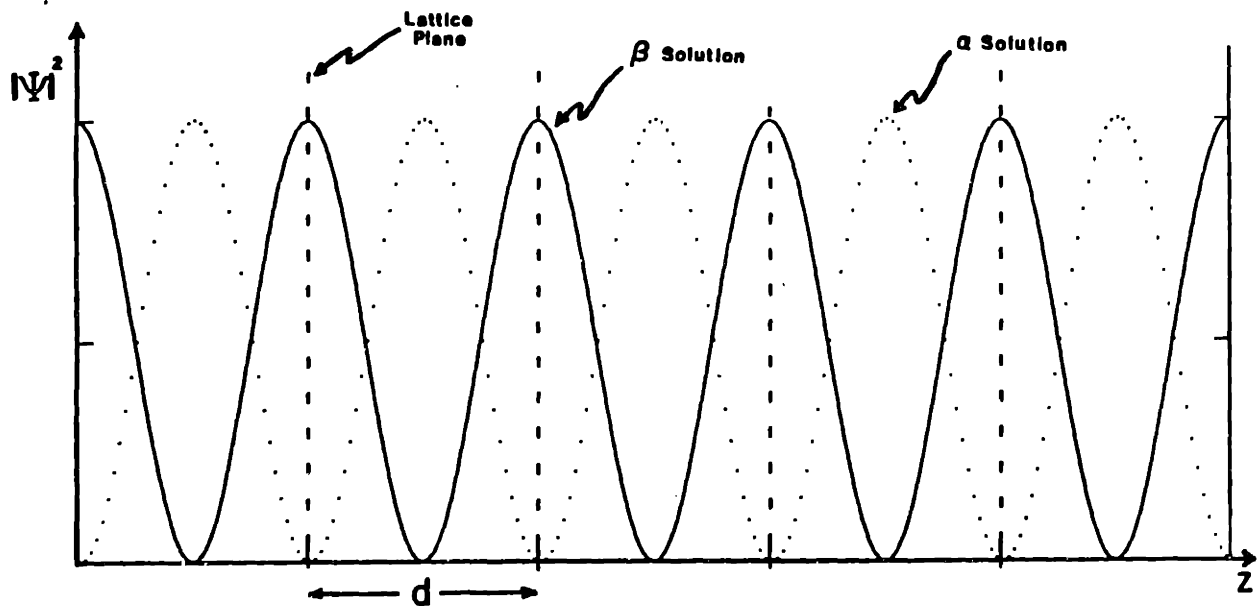


Fig.(2.3) The probability density corresponding to the plane wave solutions α and β plotted along the z direction in the crystal lattice. The α and β solutions display the periodicity of the lattice and are peaked respectively half way between and on the lattice planes.

propagation vector magnitude) associated with these two solutions can be seen to follow from energy conservation and the repulsive nature of the neutron-nuclear potential in silicon. In the previous expression the pre-factor of the cosine function simply changes the contrast of the probability oscillations. The oscillation amplitude gets smaller with increasing $|\gamma|$.

Section 2.1.3 - The Type 2 Solutions to the T.T. Equations

We now move on to discuss another type of solution for the T.T. equation in the two beam approximation. It will be useful to write out the two beam wave function explicitly in terms of the y parameter. Using (2.1.11) and (D2.1.4) we obtain

$$\psi_{\left(\begin{smallmatrix} \beta \\ \alpha \end{smallmatrix}\right)}(\vec{r}) = e^{-i\frac{A}{2}\left(y\frac{z}{\sin\theta_B} \pm \sqrt{y^2+1}\frac{x}{\cos\theta_B}\right) + i\phi} \left\{ e^{i\vec{k}\cdot\vec{r}} + \left(y \pm \sqrt{y^2+1}\right) e^{i(\vec{k}+\vec{G})\cdot\vec{r}} \right\} \quad (2.1.14)$$

where the +/- signs are associated with the β and α solutions respectively.

Up to now the discussion of diffraction made no reference to the world outside of the crystal. To discuss this second type of solution, often called the pendulum solution, it is necessary to consider the crystal boundaries.

In Fig. (2.1) the diffracting planes were related to the (X,Z) coordinates by assigning $\vec{G} = -G\hat{z}$. The physical meaning of the y parameter becomes apparent when the crystal front surface is also included with the coordinate system. In this discussion (and our experiments) the crystal is oriented for symmetric Laué transmission, that is, \vec{G} is parallel to the crystal surface. Below, Fig. (2.4) illustrates this geometry. The vector \vec{k} represents the propagation vector of an incident plane wave. For this discussion the incident wave front, and

the crystal surface are to be considered as infinite in extent.

The boundary condition for waves satisfying the SE requires that the component of \vec{k} parallel to the surface be continuous across the boundary. Then in order to match with (2.1.14), the outside wave (of energy E and wave vector \vec{k}) must satisfy the equation

$$k_z = -\frac{A}{2\sin\theta_B}y + K_z. \quad (2.1.15)$$

In Fig. (2.4) $\Delta\theta = \theta - \theta_B$, where θ_B is the exact Bragg angle for this neutron energy. It is assumed that $\Delta\theta$ is very small. Previously \vec{k} was chosen such that $|K_z| = G/2$, but with the incident wave slightly off exact Bragg incidence, $k_z = k\sin(\theta_B + \Delta\theta)$, and thus equation (2.1.15) becomes

$$y = \frac{-2\sin\theta_B}{A} \left\{ k\sin(\theta_B + \Delta\theta) + \frac{G}{2} \right\} \cong \left(\frac{2\pi\cos\theta_B}{A} \right) \frac{2\sin\theta_B}{\lambda} (\theta_B - \theta)$$

We now define an important quantity, the pendellösung length Δ_0

$$\Delta_0 = \frac{2\pi\cos\theta_B}{A} \quad (D2.1.5)$$

where again, $A = \frac{|v|}{K} \sim 10^{-6} K$.

Using Bragg's law and (D2.1.5) to simplify the expression for y one finds

$$y = \frac{\Delta_0}{d(hkl)} (\theta_B - \theta) \quad (2.1.16)$$

For typical wavelengths and crystals the pendellösung length is about 1/10 mm. Therefore the ratio in (2.1.16) has a magnitude of about one million. Thus the y parameter is a very sensitive measure of the degree of off-Braggness of the incident radiation.

Referring back to the dispersion surface (Fig. (2.2)), we note that it is oriented so that the diameter (the line connecting the tie points at $y=0$) is perpendicular to \vec{c} . The boundary condition (2.1.15) then implies that a single incident plane wave (a single y) will excite two solutions (one for each branch), each solution being made up of two plane wave components. These solutions are also known as wavefields and since the two wavefields are excited by the same source wave, they are coherent and their amplitudes must be added to determine the total wave field inside the crystal. For radiation incident exactly on Bragg the diameter points are excited and the wave momentum travels along the lattice planes (perpendicular to the dispersion surface at $y=0$). For

the case where the incident wave is slightly off exact Bragg incidence, the α and β wavefields propagate at equal and opposite angles ($\pm\Omega$) relative to these planes.

For an incident plane wave of unit amplitude outside the crystal the appropriate superposition of α and β wavefields gives

$$\begin{aligned} \psi(\vec{r}) = e^{-i\frac{\Delta}{2}y\frac{z}{\sin\theta_B} + i\phi} \{ & e^{i\vec{K}\cdot\vec{r}} \left(\cos \frac{\pi X}{\Delta_0} \sqrt{y^2 + 1} + \frac{iy}{\sqrt{y^2 + 1}} \sin \frac{\pi X}{\Delta_0} \sqrt{y^2 + 1} \right) \\ & + e^{i(\vec{K} + \vec{c})\cdot\vec{r}} \left(-i \frac{1}{\sqrt{y^2 + 1}} \sin \frac{\pi X}{\Delta_0} \sqrt{y^2 + 1} \right) \}. \end{aligned} \quad (2.1.17)$$

Note the following features of this type of solution.

1) The two plane wave amplitudes in (2.1.17) are to be found everywhere inside the crystal since no spatial restriction was placed on the incident wave.

2) The α and β wavefields, have equal and opposite ΔK_x components and therefore interfere (or beat against each other) as the waves propagate into the crystal. The characteristic spatial frequency of this interference is Δ_0 .

3) The interference between wavefields implies a periodic swapping, back and forth, of amplitude between the forward and Bragg directed waves (see (2.1.17)). Ewald has given this phenomenon the name pendellösung oscillations.

4) The boundary condition (2.1.15) must also apply at the back face of the crystal. In general two waves will exit the crystal, one forward directed, the other Bragg directed. Their relative intensities are determined by the pendellösung amplitudes at the exit face. For a fixed thickness crystal the brightness in either beam can vary depending on the wavelength (through Δ_0), and the incident wave direction (through y).

We end the discussion by plotting the probability density associated with this type of solution. For the case of radiation incident on the crystal exactly satisfying the Bragg condition ($y=0$) one finds

$$|\Psi(x,z)|^2 = 1 - \sin^2 \frac{2\pi x}{\Delta_0} \sin^2 \frac{2\pi z}{d}.$$

This expression is plotted in Fig. (2.5) which illustrates the periodic nature of the wave propagation.

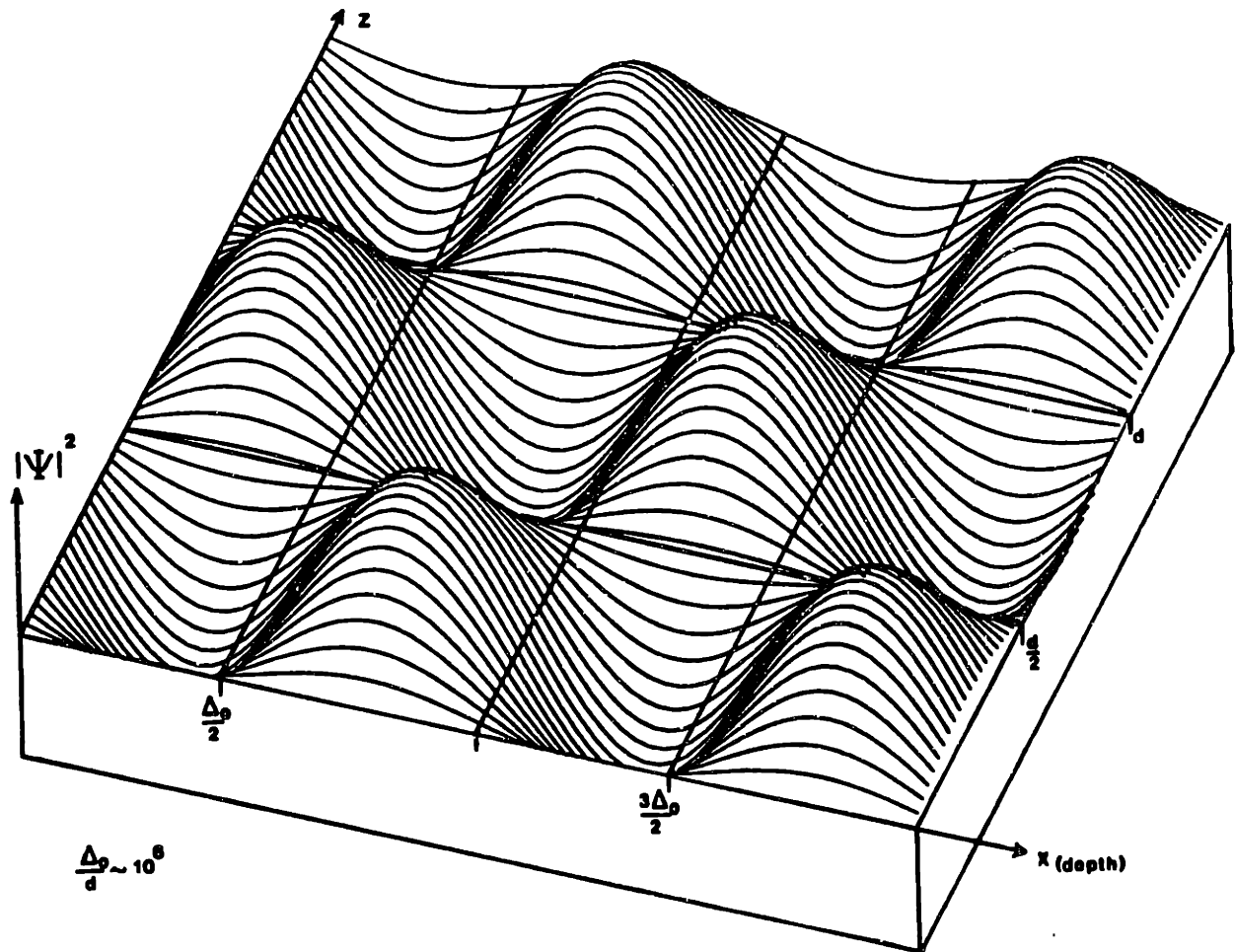


Fig.(2.5) The probability density associated with the wavefunction (2.1.17) for the case of exact Bragg incident radiation ($y=0$). The length scales along the X and Z axes differ by approximately one million with the pendellösung length (x -axis) the larger. The 2-dimensional nature of the oscillations suggests that plane wave pendellösung behavior discussed in the text.

Section 2.2 Diffraction with Point Source Illumination

The third and final solution to the diffraction problem, the point source solution, is discussed in this section. This solution will help in understanding some features of the pendellösung oscillations as they occur in the NSPR experiment. This type of solution has been extensively studied by Kato who generally referred to the subject as spherical wave theory. An important result of this section is the connection between the point source solutions considered below and the waves fields thus far considered.

We begin by reviewing some properties of plane and spherical waves. A plane wave implies a single direction of propagation while a spherical wave propagates from some source in all directions. The spatial extent of a plane wave (front) is infinite, the spherical wave starts from a point and is finite except at infinite distances. These two types of elementary waves are of course interconnected. On the one hand, a plane wave can be constructed (in the Huygens sense) by assembling an infinite set of point sources distributed on a plane surface. If these sources radiate in phase, a plane wave will propagate normal to the source plane. On the other hand, a spherical wave can be made up from equal contributions of plane waves propagating in all possible directions all with the same phase. This suggests a comparable connection, for the case of in-crystal wave fields, between those generated by

plane wave and by spherical wave illumination.

Since the description of diffraction presented in this thesis is 2-dimensional in nature, the plane waves considered have wave fronts that are lines. In the same way for this discussion, the spherical waves will be considered to have circular fronts.

The distinction between plane and spherical waves begins to break down as soon as one spatially restricts the plane wave with an aperture. The consequences of slit and edge diffraction are particularly striking when the medium beyond the slit is a crystal. To see this, note that the angular range over which a perfect crystal will accept neutron radiation for Bragg diffraction is only about 0.5 seconds of arc, the Darwin width. It is interesting to estimate the width (s) of a slit required to diffract a single plane wave front to this extent. For waves of 1\AA wavelength and a diffraction broadening angle $\Delta\theta = \pm 0.25$ sec.

$$s \sim \frac{\lambda}{\Delta\theta} \sim 0.08\text{mm}.$$

A slit of this size or smaller, even when illuminated by an on-Bragg plane wave is equivalent to a point source for in-crystal wave propagation. In the language of Section (2.1), (which strictly speaking is not appropriate here) effectively all the points on the dispersion hyperbola are excited

simultaneously and coherently. The solution appropriate to such illumination conditions is often called the quasi-point source solution. It was first given by Kato[9] in 1960. The wave function is again of the form (2.1.2), but now, instead of the amplitudes (2.1.8), we have for the forward and Bragg amplitudes

$$a_o(\vec{r}) = -\frac{A}{2}\sqrt{\frac{S_o}{S_c}}J_1(A\sqrt{S_oS_c}) \times [\theta(S_o)-\theta(-S_c)]+\delta(S_c) \quad (2.2.1a)$$

$$a_c(\vec{r}) = -i\frac{A}{2}J_0(A\sqrt{S_oS_c}) \times [\theta(S_o)-\theta(-S_c)] \quad (2.2.1b)$$

where A was defined in (D2.1.5). Referring to Fig. (2.6) for the meaning of the spatial variables S_o, S_c , the full two beam wavefunction is written

$$\begin{aligned} \psi(\vec{r}) = e^{i\vec{K}\cdot\vec{r}} & \left\{ -\frac{A}{2}\sqrt{\frac{S_o}{S_c}}J_1(A\sqrt{S_oS_c}) \times [\theta(S_o)-\theta(-S_c)]+\delta(S_c) \right\} \\ & + e^{i(\vec{K}+\vec{c})\cdot\vec{r}} \left\{ -i\frac{A}{2}J_0(A\sqrt{S_oS_c}) \times [\theta(S_o)-\theta(-S_c)] \right\} \end{aligned} \quad (2.2.2)$$

Here $J_0(W)$ and $J_1(W)$ are respectively Bessel functions of the first kind of order 0 and 1. The θ functions are unit

amplitude step functions which restrict the non-zero wave amplitudes to a triangular region, known as the Borrmann fan, between the lines $S_0=0$ and $S_c=0$. The delta function accounts for the point source on the surface of the crystal. Note that for the case of the quasi-point source there is only one solution (corresponding to one point of illumination on the crystal face) as compared to the family of solutions (allowed tie points) found in the plane wave case.

To discuss some of the important features of this solution we illustrate the three coordinate systems previously defined in Fig. (2.1), below in Fig. (2.6).

The first feature to notice is that for both the forward and Bragg amplitudes, the Bessel functions have a common argument, $A\sqrt{S_0 S_c}$.

In terms of the coordinates (X,Z) one finds

$$S_0 S_c = \frac{1}{4} \left(\frac{X^2}{\cos^2 \theta_B} - \frac{Z^2}{\sin^2 \theta_B} \right).$$

If the left hand side is equal to a constant, (2.2.3) is the equation of a hyperbola in real (or crystal) space. Thus one can see that the Bessel functions (separately) have constant amplitude on these hyperbolas.

Let us consider specifically the Bragg diffracted amplitude (2.2.1b) because in The NSPR experiment we measure the Bragg directed radiation. Fig. (2.7) is a plot of (2.2.3) with $\theta_B = 45^\circ$.

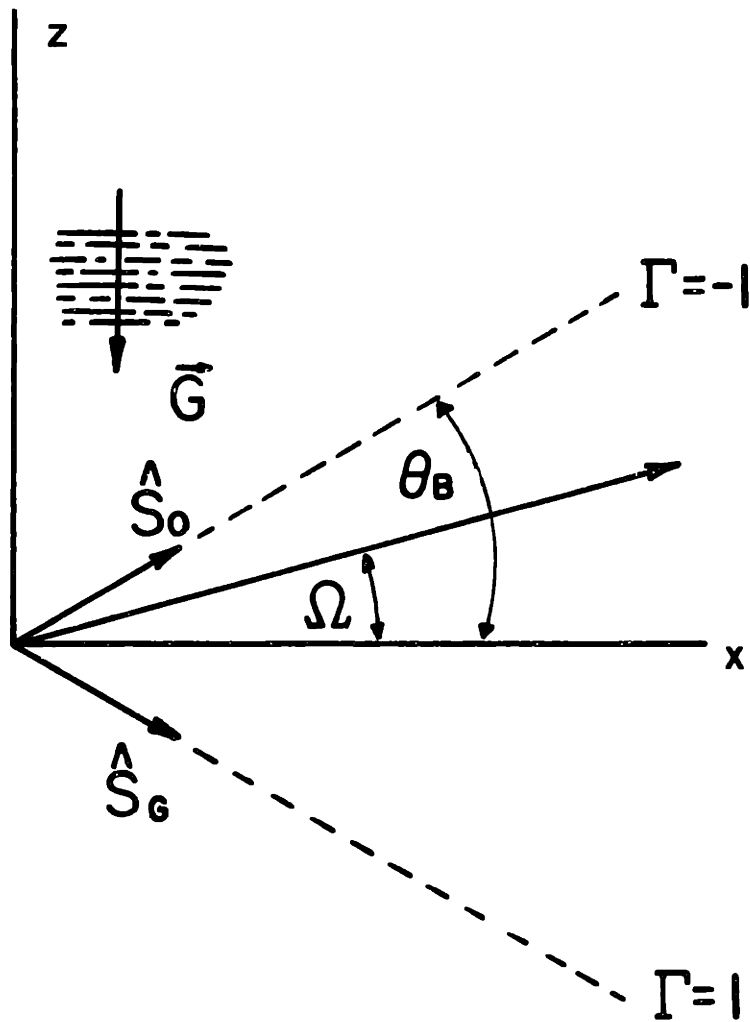


Fig.(2.6) The three coordinate systems used in the discussion of the point source solutions outlined in the text. The coordinates (Γ, X) are especially useful when considering the radiation pattern at the back face of a crystal where X = the crystal thickness. In general $\Gamma = -\frac{\tan \Omega}{\tan \theta_B}$.

The curves in this figure represent the first 10 nodes in the Bragg amplitude inside the crystal. For each curve, successive zeros of the Bessel function $J_0(W)$ [10] have been set equal to the product $A\sqrt{S_0 S_c}$.

Henceforth, these curves of constant amplitude will be called fringes.

Although it is difficult to see it in the figure, the separation between successive fringes approaches a constant value, on the X axis for large X . Recognizing that the separation between zeros of $J_0(W)$ for large argument approaches π , equations (2.2.1b), (2.2.3) and the definition of A (D2.1.5) imply that this constant fringe spacing is just the pendellösung length originally defined for the plane wave case. Thus, for $z=0$, the Bragg amplitude oscillates in depth with period equal to Δ_0 .

Another point comes from examination of the fringes at constant X . Moving along the Z axis (for some X) reveals that there should be amplitude oscillations. However, the fringes are no longer evenly spaced; they "pile up" upon approaching the edges of the fan. This can be clearly seen in Fig. (2.7).

Let us now switch to the (X, Γ) coordinate system first introduced in Fig. (2.6). The Bragg amplitude function (2.2.1b) can be written

$$a_c(X, \Gamma) = -i \frac{A}{2} J_0 \left(\frac{\pi X}{\Delta_0} \sqrt{1 - \Gamma^2} \right) \times [\theta(1 - \Gamma) - \theta(-(1 + \Gamma))]. \quad (2.2.4)$$

An observation which can be made from examining Fig. (2.7), in particular from the line drawn at constant $\Gamma (\neq 0)$ is that the separation between successive fringes changes as Γ changes. Thus, for $|\Gamma| > 0$, the "effective pendellösung length" (distance between fringes) increases with increasing Γ .

The bulk of this discussion has neglected mention of the forward amplitude function (2.2.1a). After the first few nodes of $J_1(W)$, one finds that this function oscillates 90 degrees out of phase with $J_0(W)$. Thus the fringes illustrated in Fig. (2.7) apply equally well to the forward amplitude. However, while these fringes coincide with nodes of the Bragg amplitude inside the crystal, they locate maxima and minima in the forward amplitude. This situation, where the spatial distribution of forward and Bragg amplitudes differ in phase by 90 degrees, is simply pendellösung behavior.

In the experiment discussed in Chapter IV a silicon crystal with parallel front and back faces is used. The crystal thickness and neutron wavelength are chosen so that the distance is about $25\lambda_0$ from front to back. In this case it is appropriate to use the large argument expansions for the Bessel functions. Thus the Bragg amplitude is written

$$a_c(X, \Gamma) = -i \left\{ \left(\left[\frac{1}{1-\Gamma^2} \right]^{\frac{1}{2}} \sin \left(\frac{\pi X}{\lambda_0} \sqrt{1-\Gamma^2} + \frac{\pi}{4} \right) + \text{Order} \left(\frac{1}{\left(\frac{\pi X}{\lambda_0} \sqrt{1-\Gamma^2} \right)} \right) \right) \times [\theta(1-\Gamma) - \theta(-(1+\Gamma))] \right\}. \quad (2.2.5)$$

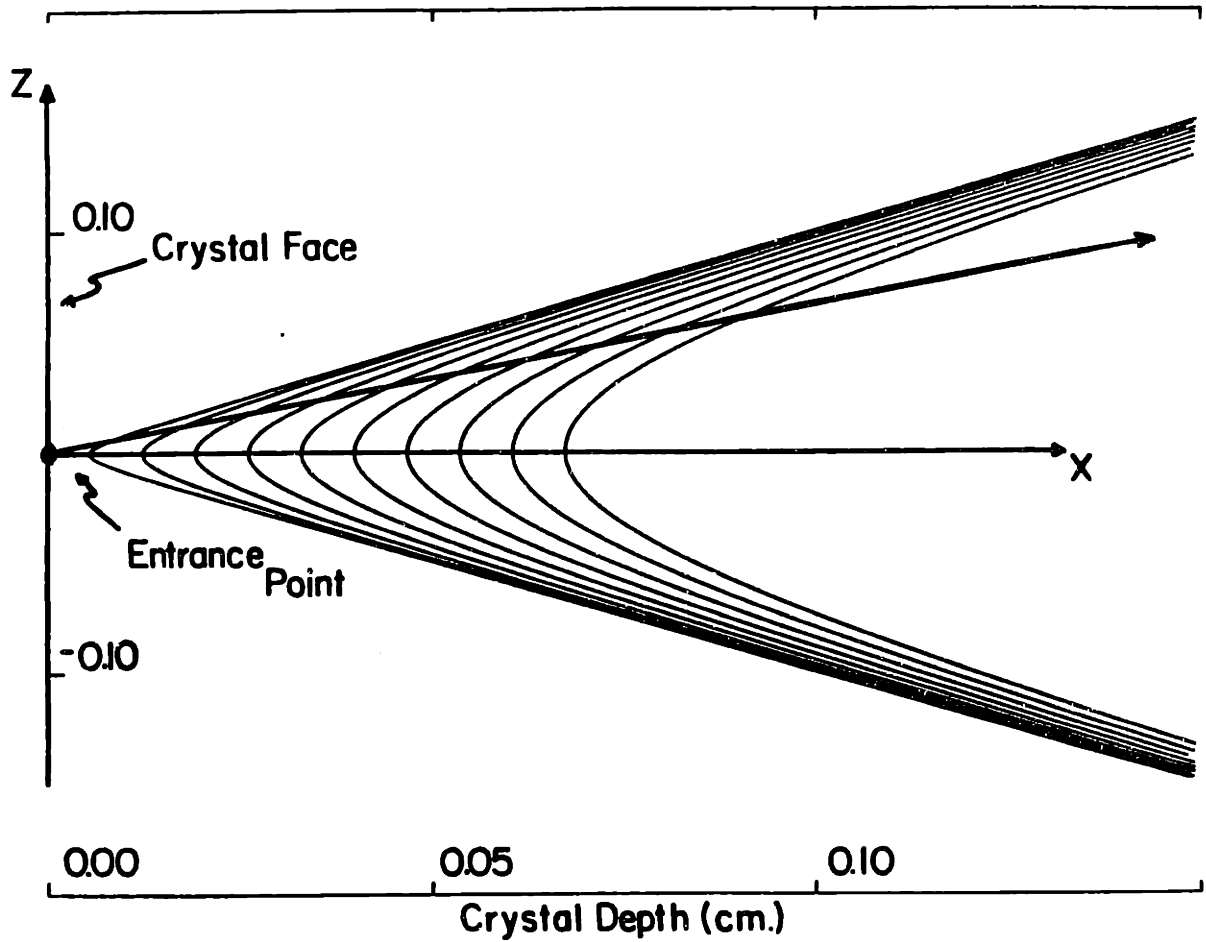


Fig.(2.7) Curves of constant Bragg amplitude form hyperbolas in a crystal illuminated by a point source of radiation. These curves asymptotically approach the edges of the Borrmann fan. The first 10 nodes in the Bragg amplitude are shown for the case of a 45 degree Bragg angle.

Note that the form of the error in (2.2.5) implies the trigonometric function is not a valid approximation very close to the edges of the fan, even in the case of a very thick crystal.

The intensity of radiation exiting the crystal in the Bragg direction is illustrated in Fig. (2.8). This profile comes from squaring the magnitude of (2.2.5) when $\lambda = 25\text{\AA}$. It is this intensity that one would expect to measure by counting neutrons and moving a very narrow slit along the back face of a crystal which is being illuminated by a point source of radiation. If the slit were too wide, one would instead see the averaged (Kato) intensity profile indicated in the figure. Such measurements are discussed in Section (2.4).

We conclude this section by remarking on the relation between plane and spherical waves in and outside a crystal. In Section (2.1), the in-crystal wave fields were derived under the assumption that a plane wave was incident on an unrestricted crystal face. In this section we have illustrated the Bessel function wave fields present inside a crystal which is being illuminated (through a fine slit) by a spherical wave. At the beginning of this section the relation between plane and spherical waves in vacuum was recalled. They are just appropriate superpositions of each other. Likewise, it has been shown[11] that the wavefields of Section (2.1) and the Bessel function solutions of this section can be constructed as superpositions of one another.

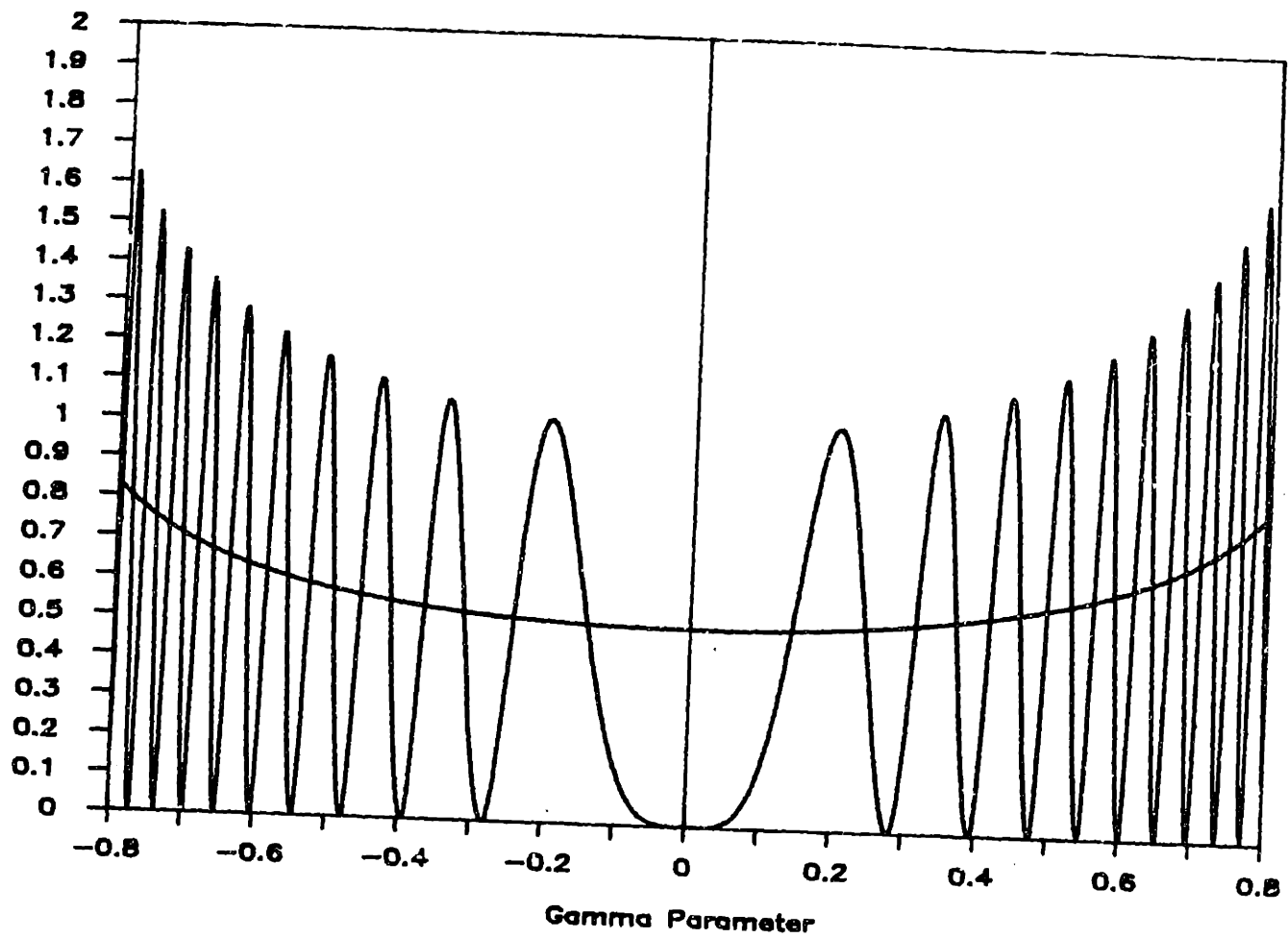


Fig.(2.8) The intensity pattern, along the back face of a parallel sided crystal, for radiation exiting in the Bragg direction when a point source illuminates the front surface. The crystal thickness is 25 pendellösung length units and the intensity oscillations are plotted versus the Gamma parameter. An additional curve, known as the Kato profile, which represents the averaged oscillations is also displayed.

Section 2.3**The Crystal Potential**

In dynamical diffraction, we use the coefficients of the Fourier transform of the neutron-crystal potential to characterize the neutron interaction with the crystal. It is of particular interest here to determine the coefficients which are appropriate for the NSPR problem. This section begins first with the Fourier analysis of a crystal composed of nuclei (a nuclear crystal), then we consider the SO potential felt by the neutrons, and finally we shall present the potential representing the effects of an external magnetic field acting on the neutron. There are other interactions "felt" by the neutron which we will not discuss here, but a good survey of them has been given by Shull [12].

Section 2.3.1 - The Neutron-Nuclear Crystal Potential

The interaction between the neutron and the nuclei of a crystal, resulting from the strong nuclear force, is usually described by using the Fermi pseudo-potential [13]. This was first done by Goldberger and Seitz [14] who wrote the potential as a sum of delta function contributions, one for each nucleus in the crystal. For a monoatomic crystal (like silicon) the form of this potential at \vec{r} is

$$V(\vec{r}) = \frac{2\pi h^2}{m} \sum_j b \delta(\vec{r} - \vec{R}_j). \quad (2.3.1)$$

Where b is the bound coherent scattering length of the nucleus. The vector \vec{R}_j ranges over the positions of all nuclei in the crystal.

We obtain the Fourier coefficient $V(\vec{G})$ by Fourier transforming $V(\vec{r})$ using the reciprocal lattice vectors \vec{G} .

$$\begin{aligned} V(\vec{G}) &= \frac{2\pi h^2}{m} \sum_j b \frac{1}{U} \int_{\text{crystal}} e^{-i\vec{G} \cdot \vec{r}} \delta(\vec{r} - \vec{R}_j) d^3\vec{r} \\ &= \frac{2\pi h^2}{mU} \sum_j b e^{i\vec{G} \cdot \vec{R}_j} \end{aligned}$$

In this expression U is the volume of the crystal. This sum can be broken into two parts, first a sum over the vectors pointing to the origin of each unit cell in the crystal; this sum yields N , the number of unit cells in the volume U . The second sum is over vectors from the origin in the unit cell to each atom of the cell. This sum gives $F(\vec{G})$, the nuclear structure factor of the unit cell. Thus, the G -th Fourier potential coefficient is

$$V(\vec{G}) = \frac{2\pi h^2}{m v_c} F(\vec{G}) \quad (2.3.2)$$

where we have defined the volume per unit cell $v_c = \frac{U}{N}$.

In our experiment the (111) reflection in silicon shall be used. Assuming the value for the coherent nuclear scattering length in silicon real and equal to that given by Shull [15] — one finds

$$V(0) = 5.4070 \times 10^{-8} \text{ eV}$$

$$V(111) = (1 - i) \times 2.6722 \times 10^{-8} \text{ eV}$$

$$V(\bar{1}\bar{1}\bar{1}) = (1 + i) \times 2.6722 \times 10^{-8} \text{ eV}.$$

From (2.1.7) and (D2.1.1) it is seen that for the two-beam approximation only the potential coefficients $V(0)$, $V(\vec{G})$, $V(-\vec{G})$ are important. Then for dynamically diffracting neutrons, the nuclear crystal appears as the simple corrugated potential which is illustrated in Fig.(2.9). In the expression for this potential the Debye-Waller factor e^{-W}

is associated with thermal oscillations of the nuclear centers. In addition, it may be noted that the complex nature of the coefficients for the (111) reflection simply shift the corrugation maxima off the lattice planes. Further it is noteworthy that the effect of thermal oscillations of the nuclei on the lattice potential is simply to diminish the corrugation amplitude.

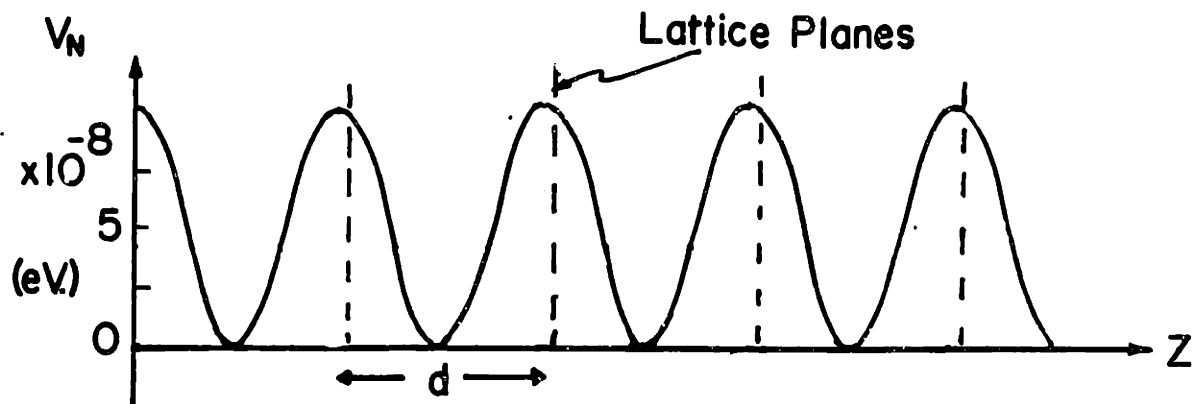


Fig.(2.9) The crystal lattice appears as a corrugated potential along the Z -direction in the dynamical diffraction description of neutron propagation in a perfect crystal when only the neutron-nuclear interaction is considered. The period of the oscillation is d , the lattice spacing; the amplitude is typically about $10^{-8} eV$.

$$\begin{aligned}
 V(Z) &= V(0) + V(\vec{G})e^{i\vec{G}\cdot\vec{r}} + V(-\vec{G})e^{-i\vec{G}\cdot\vec{r}} \\
 &= V(0)\left(1 + \frac{e^{-W(111)}}{\sqrt{2}} \cos \frac{2\pi}{d(111)}\left(Z - \frac{d(111)}{8}\right)\right)
 \end{aligned}$$

Section 2.3.2 - The Spin-Orbit Potential of the Lattice

The second potential needed for our discussion is that due to the neutron spin-neutron orbit interaction. Schwinger [16] introduced this interaction in order to suggest a new mechanism for the polarization of fast (1 Mev) neutrons. In moving through the electric field surrounding a nucleus the neutron magnetic moment senses a magnetic field. Because the electric field is radial about the nucleus, the magnetic field sensed by the moving neutron is asymmetrical across the scattering center. In contrast to the nuclear (force) potential which is symmetric; this SO potential is antisymmetric, with sign dependent on the orientation of the neutron spin. This asymmetry implies that the SO scattering amplitude is imaginary, that is 90 degrees out of phase with the nuclear scattering.

Shull [17] explored this SO scattering with slow (thermal energy) neutrons. He pointed out that the Schwinger expression for the SO scattering amplitude must, in this case, be modified to include the effect of electron charge screening of the nuclear charge. The Schwinger interaction potential is written

$$V_{so}(\vec{r}) = \mu \frac{eh}{2m^2 c^2} \vec{\sigma} \cdot (\vec{E} \times \vec{p}). \quad (2.3.3)$$

It should be emphasized that this potential has the form of a magnetic moment in a magnetic field, that is $-\vec{\mu} \cdot \vec{B}$.

It contains the quantum mechanical operators:

$$\vec{p} = -i\hbar \vec{\nabla}$$

$$\vec{\sigma} = \sigma_x \hat{x} + \sigma_y \hat{y} + \sigma_z \hat{z}$$

where the sigmas are the Pauli spin matrices for spin 1/2 . In the expression $\mu = -1.91$ and is the numerical value of the neutron magnetic moment in nuclear magnetons. The electric field of the crystal \vec{E} may be written in terms of the electric potential $\phi(\vec{r})$ as

$$\vec{E}(\vec{r}) = -\vec{\nabla}\phi(\vec{r}) = -\vec{\nabla} \left\{ \int_{crystal} \frac{N(\vec{R})}{|\vec{r} - \vec{R}|} d^3\vec{R} + \int_{crystal} \frac{n(\vec{r}')}{|\vec{r} - \vec{r}'|} d^3\vec{r}' \right\}.$$

Where $N(\vec{R})$ is the nuclear charge density, and $n(\vec{r}')$ the electron charge density inside the crystal.

We again want the Fourier potential coefficients. The derivation of these is found in Appendix (A2.3), the results are

$$V_{so}(0) = 0$$

$$V_{so}(\vec{G}) = -CF'(\vec{G}) \frac{\vec{\sigma} \cdot (\vec{G} \times \vec{\nabla})}{G} \quad (2.3.4a)$$

$$V_{so}(-\vec{G}) = +CF'(-\vec{G}) \frac{\vec{\sigma} \cdot (\vec{G} \times \vec{\nabla})}{G} \quad (2.3.4b)$$

where, $F'(\vec{G}) = \frac{F(\vec{G})}{b_{\text{silicon}}}$

and from the appendix, $C = 2\pi\mu \left(\frac{eh}{mc} \right)^2 \frac{1}{v_c} \{Z - f(G)\}.$

To proceed with the evaluation of these coefficients we recognize that the potentials operate on a wavefunction of the form (2.1.2). As was seen in Sections (2.1) and (2.2), the amplitude functions a_0 and a_c vary (in space) about 100,000 times more slowly than do the plane waves they multiply. Therefore after operating on such a wavefunction the quantity in parenthesis may be written $i(\vec{G} \times \vec{R})$. We note two properties of the SO interaction as represented by these coefficients.

a) The coefficients (2.3.4), which come from the Fourier expansion of (2.3.3), represent the interaction associated with a magnetic moment in a periodic magnetic field. The field varies with the same length scale as the crystal lattice and it is therefore described by two Fourier coefficients in G .

b) This magnetic field is polarized normal to the plane of scattering along the direction $(\vec{G} \times \vec{R})$. It has a strength dependent on the neutron wavevector, the geometrical structure

factor of the crystal, and the atomic charge density.

The size of these potential coefficients, for the silicon (111) reflection used in our experiment and a Bragg angle of 8.75 degrees, is

$$|V_{so}(111)| = 2.99 \times 10^{-10} \text{ eV}.$$

The SO potential is therefore about 100 times weaker than the neutron-nuclear potential discussed earlier. In Fig. (2.10) we illustrate the SO potential sensed by neutrons with magnetic moment polarized up, normal to the plane of scattering. In this figure the SO potential has been multiplied by 10 so that it may be seen relative to the nuclear potential (previously shown in Fig. (2.9)) which is included along with a third potential to be discussed shortly. Note that the two periodic potentials are shifted relative to one another by 1/4 lattice spacing.

$$V_{so}(Z) = |V_{so}(111)| \cos \frac{2\pi}{d(111)} \left(Z + \frac{d(111)}{8} \right)$$

The last potential we consider is that of a neutron magnetic moment in a uniform external magnetic field. This potential is named V_{ext} , it is written

$$\begin{aligned}
 V_{ext} &= -\vec{\mu} \cdot \vec{B}_{ext} \\
 &= -\mu \left(\frac{eh}{2mc} \right) \vec{\sigma} \cdot \vec{B}_{ext}.
 \end{aligned}$$

This potential is a constant in space, it is included in Fig. (2.10) to indicate its size when the external magnet field is 6000 Gauss.

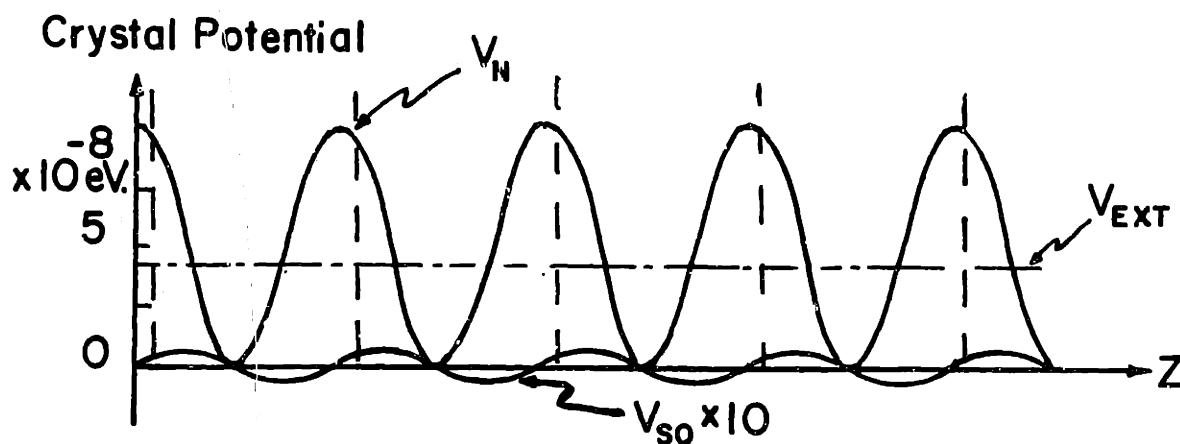


Fig.(2.10) The three crystal potentials used in the description of NSPR are the nuclear potential V_N , the spin-orbit (SO) potential V_{SO} , and a potential due to the applied magnetic field V_{ext} . The SO potential is multiplied by 10 so that it may be seen relative to the other potentials in the figure. Note that the two periodic potentials are displaced from one another by one-quarter lattice spacing.

1 Section 2.4 - Experimental Antecedents to NSPR

The Neutron Spin-Pendellosung Resonance (NSPR) phenomenon which will be discussed in Chapters III, IV, and V utilizes pendellösung oscillations to amplify the effects of the spin-orbit (SO) interaction in thermal neutron scattering. To understand the connection between these two seemingly distinct processes and, in particular, to set a foundation for appreciating the NSPR experiment, we outline two measurements that predate the present work. These two experimental studies were pioneering endeavors in their field and both were performed by the same person. In the first experiment to be discussed the existence of pendellösung fringe structures in neutron diffraction was demonstrated. The second experiment, which preceded the first, was the earliest in which the neutron spin-neutron orbit interaction was observed in slow neutron scattering.

Section 2.4.1 - Neutron Pendellösung Fringe Measurements

The neutron pendellösung fringe measurements were carried out by Shull between 1967 and 1974. In these experiments he studied the spatial and wavelength dependence of the fringes, explored the applicability of plane wave (Section (2.1)) and spherical wave (Section (2.2)) theory to experimental

conditions, and made the most precise determination of the coherent nuclear scattering amplitude b for silicon.

The experimental arrangement of the pendellösung crystal is illustrated below in Fig. (2.11). A crystal of thickness t is cut for symmetric Laue transmission and very narrow (0.13mm) slits are positioned on the front and back faces. A wide spectrum, highly collimated incident beam enters the front slit (which is fixed in location). The Bragg diffracted radiation exiting the crystal through the back slit (which may be scanned across the back face) is measured by a down-stream detector. Essentially, two measurements are carried out. a) Measurement of the spatial pendellösung pattern is made by fixing the orientation of the crystal (and thus the wavelength) and scanning the back slit across the Borrmann fan. This is indicated in Fig. (2.12) where the results of scans are shown for the same crystal at two different wavelengths.

b) Measurements of wavelength pendellösung are made by fixing the location of the scanning slit (usually at the center of the Borrmann fan) and scanning the diffracted wavelength when a full spectrum beam is incident on the crystal. This is accomplished by rotating the crystal and detector about an axis normal to the plane of scattering which is located at the entrance slit. Fig.(2.13) shows such a scan carried out using a crystal of 0.5552 cm thickness.

In Sections (2.1) and (2.2) we have derived expressions

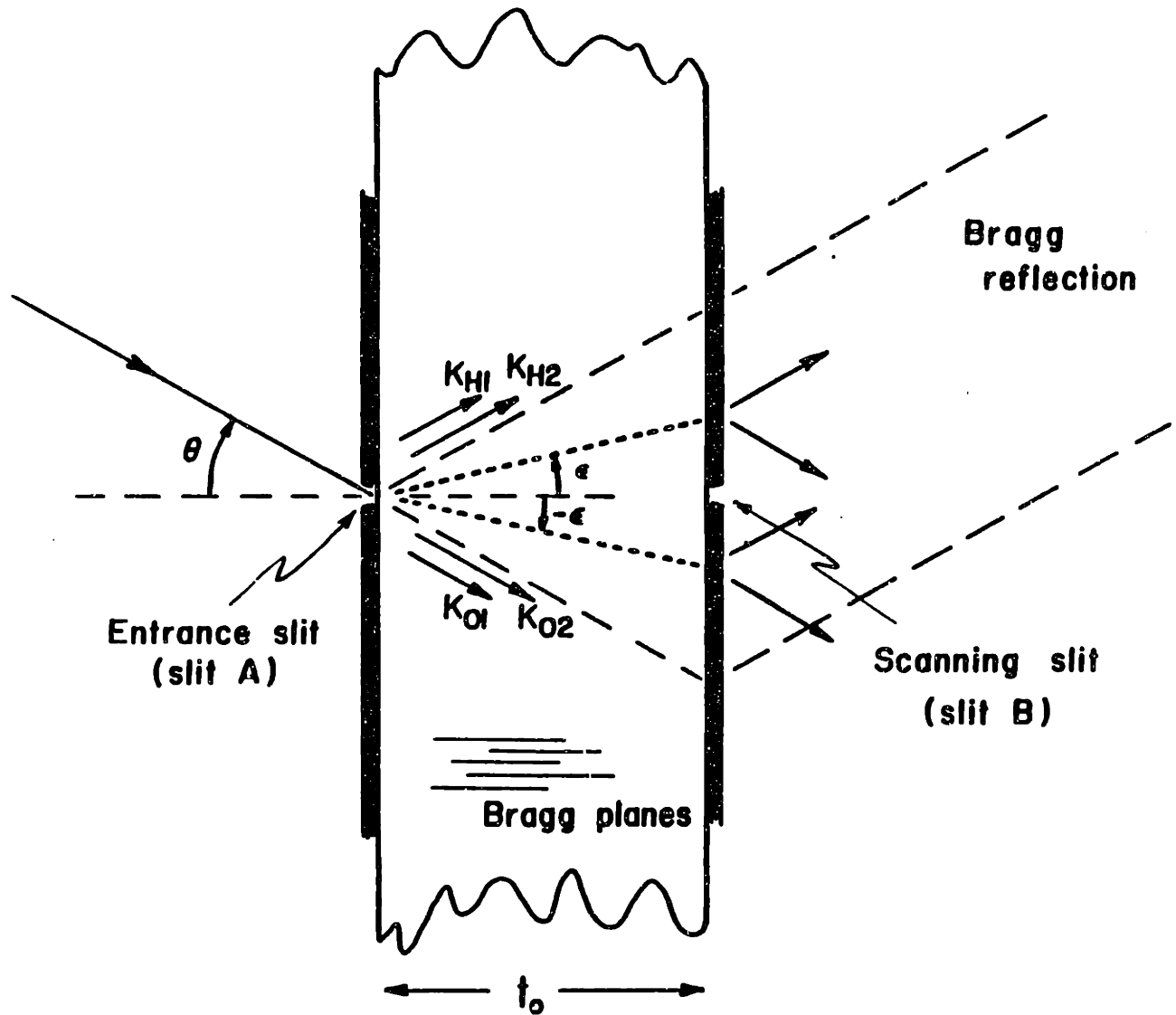


Fig.(2.11) Schematic diagram of Bragg-reflection experiment used to detect pendellösung interference fringes. The perfect silicon crystal is arrayed for symmetric Laue transmission and neutron beam defining slits are positioned on the front and back faces. The dashed lines form the edges of the Borrmann fan and the dotted lines represent two possible directions of wave flow in the fan.

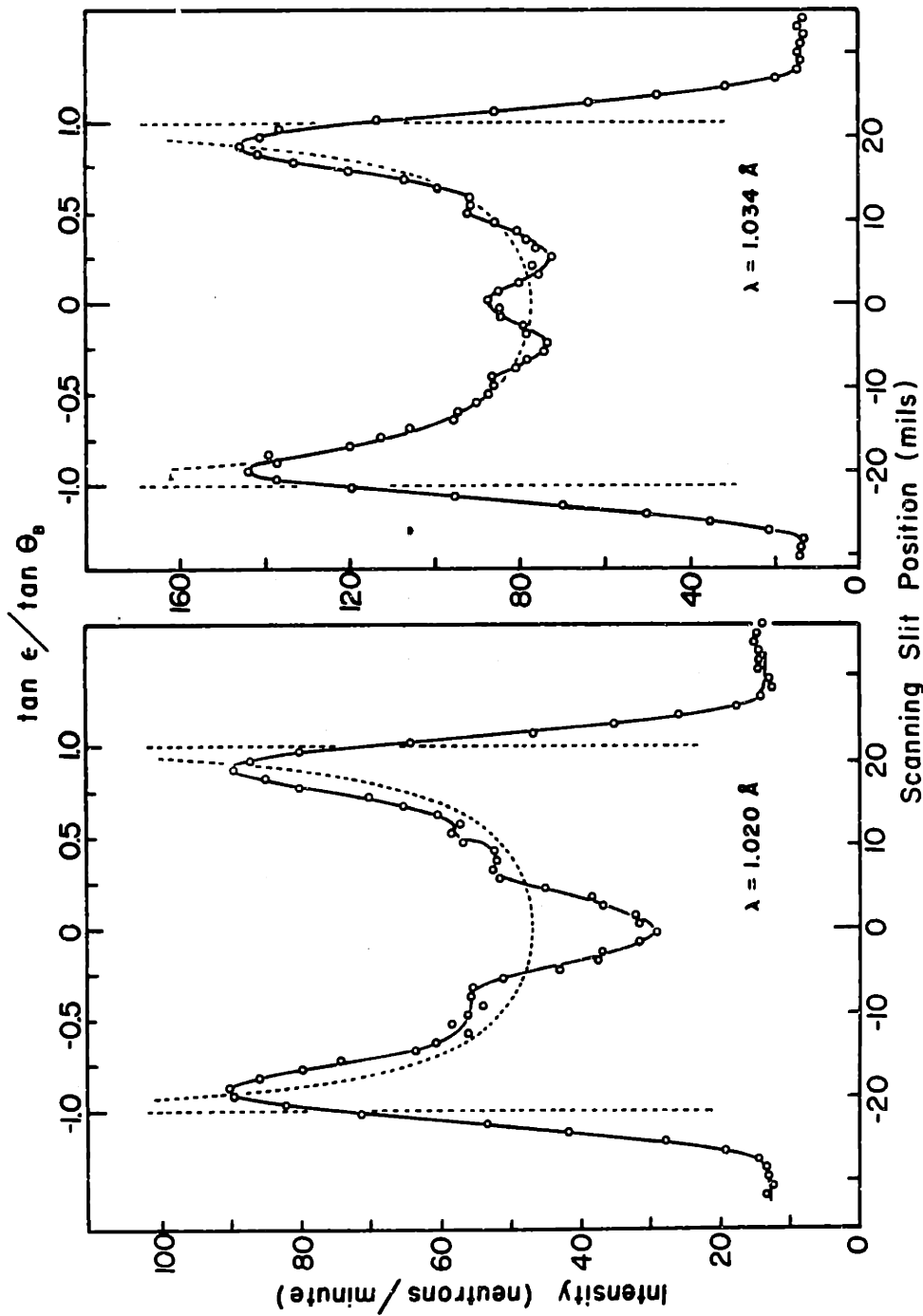


Fig. (2.12) Intensity distribution within the (111) silicon Bragg reflection showing interference-fringe structure for two different incident neutron wavelengths. The measurements are performed by scanning a slit along the back face of the crystal. The limiting Kato profile (discussed in section (2.2)) is shown as dotted curves.

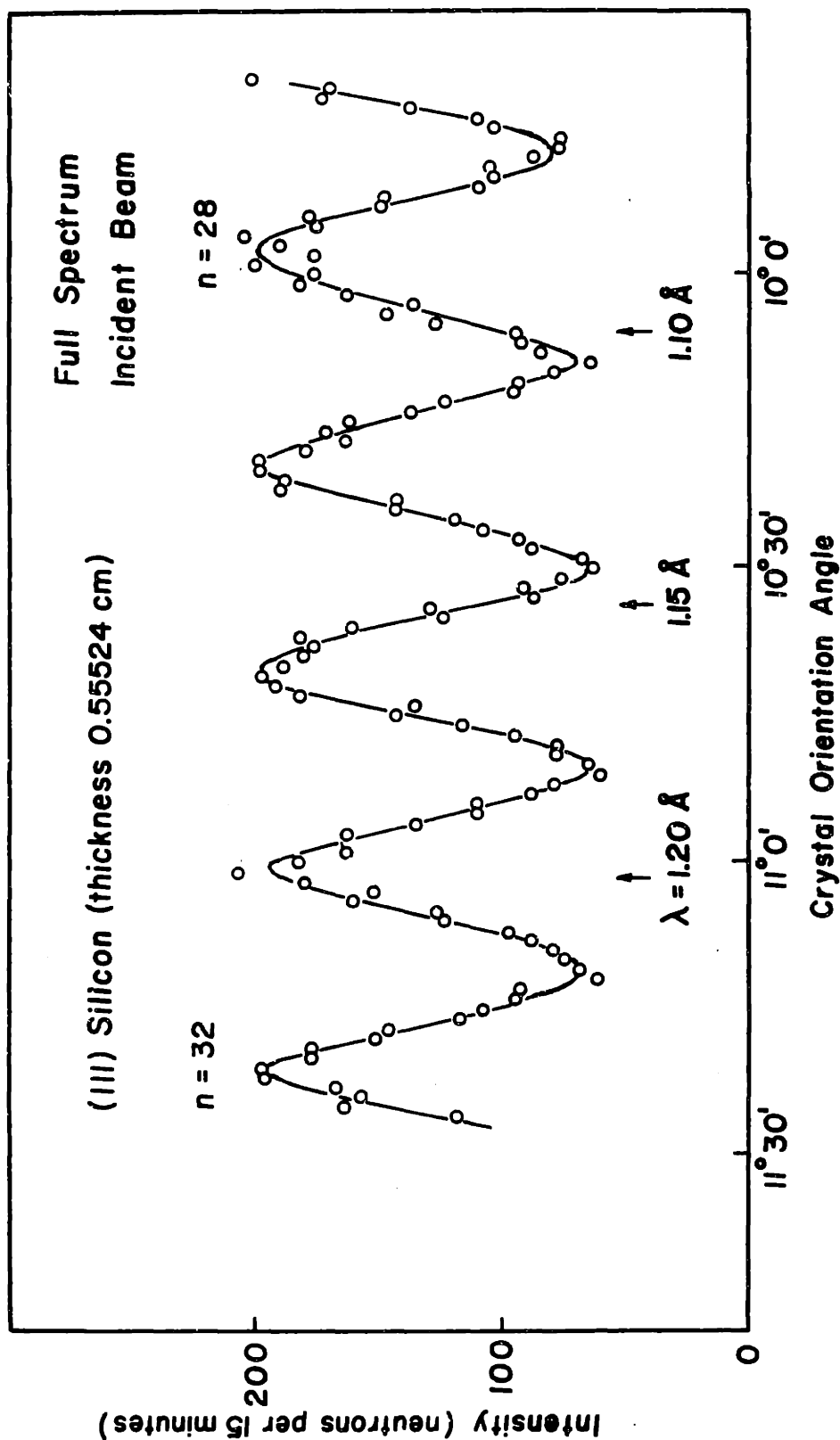


Fig. (2.13) Fringe development at the center of the Bragg reflection as the wavelength is increased. The fringe pattern corresponds to a crystal thickness of 0.5552 cm. Fringe order numbers and wavelengths are indicated.

(2.1.8) and (2.2.1a,b) which give respectively the diffracted amplitude (at crystal depth t) associated with a single incident plane wave (characterized by the direction parameter y), and for a quasi-point source. We use these expressions to write the intensity in the Bragg directed radiation in terms of crystal thickness (t), slope parameter (Γ), and pendellösung length (Δ_0) for two cases:

Plane wave incidence (P. W. Theory)

$$I_{PW}(\Gamma) = C' \frac{1}{\sqrt{1-\Gamma^2}} \sin^2 \left(\frac{\pi t}{\Delta_0} (1-\Gamma^2)^{-1/2} \right) \quad (2.4.1a)$$

Quasi-point source (S. W. Theory)

$$I_{SW}(\Gamma) = C' \frac{1}{\sqrt{1-\Gamma^2}} \sin^2 \left(\frac{\pi}{4} + \frac{\pi t}{\Delta_0} (1-\Gamma^2)^{1/2} \right) \quad (2.4.1b)$$

where $\frac{\pi t}{\Delta_0} = 2tN d(hkl) F(hkl) \tan \theta_B$.

The important difference between these two expressions is the Γ dependence of the phase in the sine functions. Shall set out to determine which expression best describes his experimental conditions. With the back slit positioned approximately at the center of the Borrmann fan ($\Gamma=0$) he

adjusts the wavelength so as to be on the rising side of the pendellösung wavelength-fringe intensity (i.e. fringe number= $n+1/4$). At this wavelength the scanning slit was carefully displaced from its central location thereby producing a fringe shift. The sign of this shift is determined by the direction of change in the measured intensity. Fig. (2.14) gives the results, clearly establishing agreement with the spherical wave theory.

The experimental conditions responsible for the spherical wave nature of the radiation are, of course, the slits. The reason they are chosen to be so narrow may be seen from the expressions (2.4.1). This experiment may be said to measure interference between the coherent wave fields discussed in Sections (2.1), but it is more correct to say that the experiment measures the coherence inherent in the point source excitation of the crystal described in Section (2.2) . The interference contrast depends on the phase definition in expressions (2.4.1). Experimentally the uncertainty in the phase depends on the variation in crystal thickness, the wavelength band diffracted by the crystal, and the range, in r , of radiation exiting the crystal through the back slit. All three are affected by slit size. They will be discussed in detail in the chapter dealing with the present experiment. It is the necessity for good fringe contrast that dictates the use of narrow slits. In turn the slits result in wide coherence over the angular range of radiation passing through

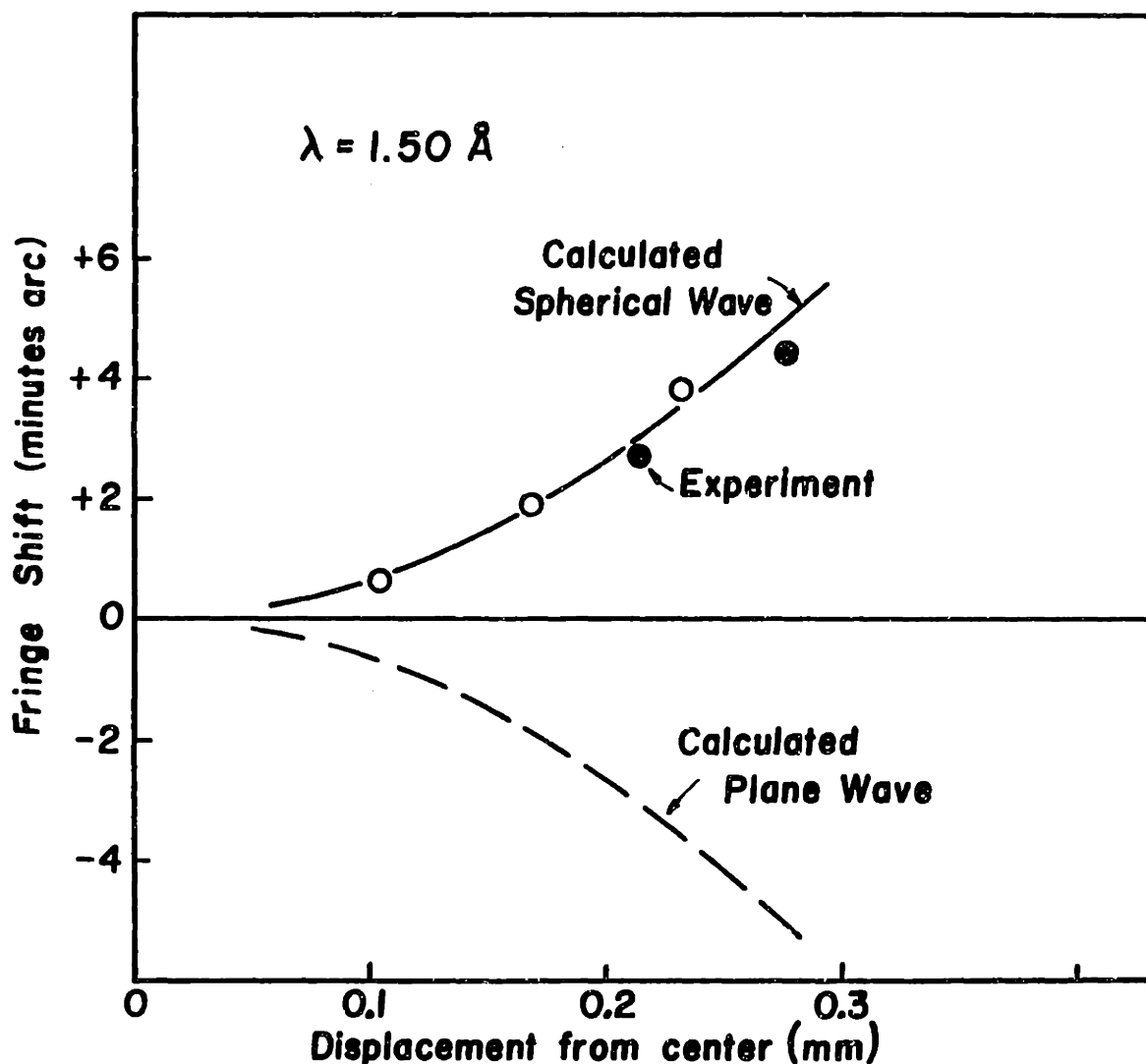


Fig.(2.14) The change in intensity, for radiation exiting the pendellösung crystal, when the back slit is displaced from the central position in the Bragg reflection. This intensity change may be thought of in terms of a fringe shift (as discussed in the text) and is plotted that way to compare to predictions of plane and spherical wave theory. The results imply that the neutron wavefront passing through the crystal must be considered to be spherical.

the crystal, and thus the spherical nature of the radiation measured.

After establishing the formula necessary for interpreting his results, Shull uses the symmetry of the spatial pendellösung fringe intensity to carefully locate his scanning slit at $r=0$. With this position established a study of wavelength pendellösung follows. The full spectrum fringe pattern (Fig. (2.13)) are obtained by diffraction on both sides of the entrance beam direction. By matching the left and right side patterns the Bragg angle corresponding to successive fringe minima and maxima may be tabulated. The result of this is an accurate measure of the wavelength dependence of the fringe spacing. Through the use of (2.4.1b) Shull determines $F(111)$, and thus the scattering amplitude. His value for the scattering length in silicon times the Debye-Waller factor of the reflection has a precision of better than one part in 5000, it is $0.41053(8) \times 10^{-12} \text{ cm}$.

Another feature of his work worth mentioning is the discovery of a regular variation from the expected location of interference maxima. The variation changes from crystal to crystal and seems to change with each remounting of the same crystal. Shull explains that this effect is consistent with a curvature-type distortion of the crystals. He points out that this distortion is very small (characterized by a radius of

curvature of between 8 and 23 kilometers), and that it emphasizes the extreme sensitivity of the fringe patterns to crystal perfection.

Section 2.4.2 - Spin-Orbit Scattering of Slow Neutrons

The first measurements of the SO scattering of thermal neutrons were carried out by Shull in 1963. Using polarized neutrons, he demonstrated that the potential (2.3.3) leads to two asymmetries in scattering from an absorbing crystal: a) for a single direction of neutron polarization, scattering from left to right as opposed to from right to left leads to different scattered intensities b) for a single direction of scattering, the measured polarization ratio is not unity. In other words the ratio of scattered intensities for two opposite neutron polarization states is different from one.

It should be emphasized that this diffraction experiment made use of mosaic crystals for which our dynamical diffraction analysis (characteristic of perfect crystals) is not applicable. The experimental arrangement consists of a beam polarized normal to the plane of scattering along with a mechanism to flip the polarization of the incident beam. A very weak, guide magnetic field is used to avoid depolarization of the beam. Finally a double axis spectrometer is used for orienting the monochromater and target crystals, as well as the detector.

As discussed in Section (2.3), the SO scattering potential may be described as asymmetric relative to the nuclear potential. Shull illustrates the combined potentials schematically in the figure below. In the bottom of the

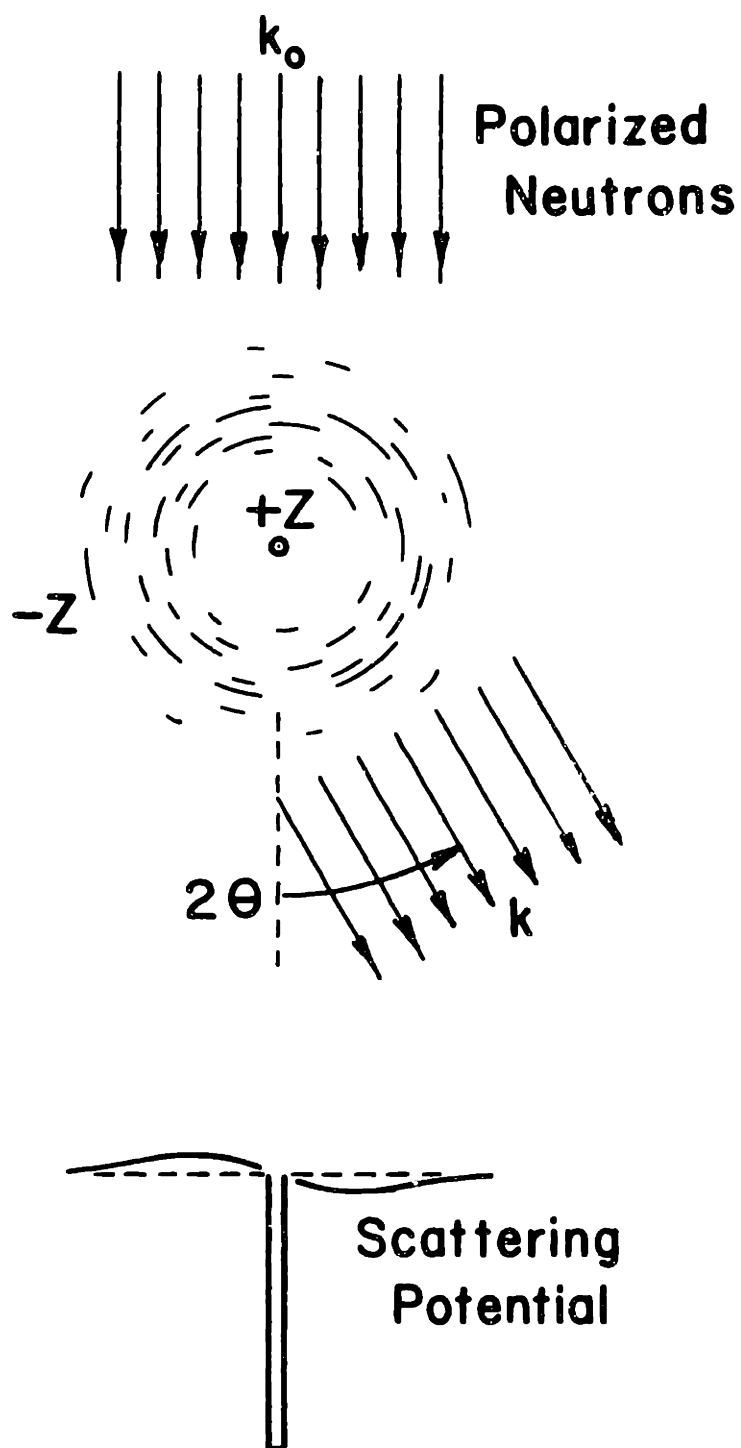


Fig.(2.15) Schematic diagram of polarized neutron scattering by an atom illustrating both the deep symmetric nuclear potential well and the shallow asymmetrical neutron spin-neutron orbit scattering potentials.

figure, one may consider the deep and narrow nuclear "well" to consist of both a real and imaginary contribution. The real part is attributable to coherent nuclear scattering while the imaginary component accounts for true absorption of neutrons by the nuclei. Schwinger[18] showed that in Born approximation the total coherent scattering amplitude becomes

$$f(\theta) = b_N + ib'_N + i(\hat{P} \cdot \hat{n} \gamma \cot \theta). \quad (2.4.2)$$

The first two terms represent the real and imaginary components of the nuclear scattering amplitude while the third is that arising from the SO scattering potential. \hat{P} and \hat{n} are unit vectors describing respectively the neutron polarization and sense of scattering. \hat{n} points up, out of the plane of scattering, for left to right scattering, and reverses direction for the opposite sense of scattering. γ describes the strength of SO scattering and its value is given by

$$\gamma = \frac{\mu_n}{2} \frac{e^2}{mc^2} Z \{1 - f\}. \quad (D2.4.1)$$

The Born approximation scattering amplitude is proportional to the Fourier transform of the potential, it thus contains an imaginary term for SO scattering because of the spatial asymmetry. The Bragg reflected intensity depends upon

$$|f(\theta)|^2 = b_N^2 + b'_N{}^2 + y^2 \cot^2 \theta \pm 2b'_N y \cot \theta. \quad (2.4.3)$$

Note that the last (or interference) term gives the interference between imaginary nuclear and SO contributions to scattering. Vanadium was used in the experiment because it has an unusually small coherent nuclear scattering amplitude b_N , while b'_N is relatively modest. With neutrons of wavelength 1.06 Å, the interference term then becomes a small but measurable contributor to the total scattering intensity. In the experiment, the ratio of Bragg diffracted intensity for the two polarization states (up and down parallel to \hat{n}) were measured.

The results are summarized in Fig. (2.16) where the measured ratios are illustrated for the two orientations of \hat{n} . These results are in reasonable agreement with the calculated values of the polarization ratio R . Taking the uncertainties in each measurement as independent, one finds the relative error (uncertainty compared to measured effect) to be about 35%. We thus have a convincing demonstration of SO scattering but not a precision measurement. It should be mentioned that the term $y \cot \theta$ is about the same for this experiment as in the present silicon NSPR experiment. Shull points out that the real nuclear scattering in silicon is much larger than in vanadium, and he demonstrates that the corresponding value of R for silicon becomes immeasurably close to unity.

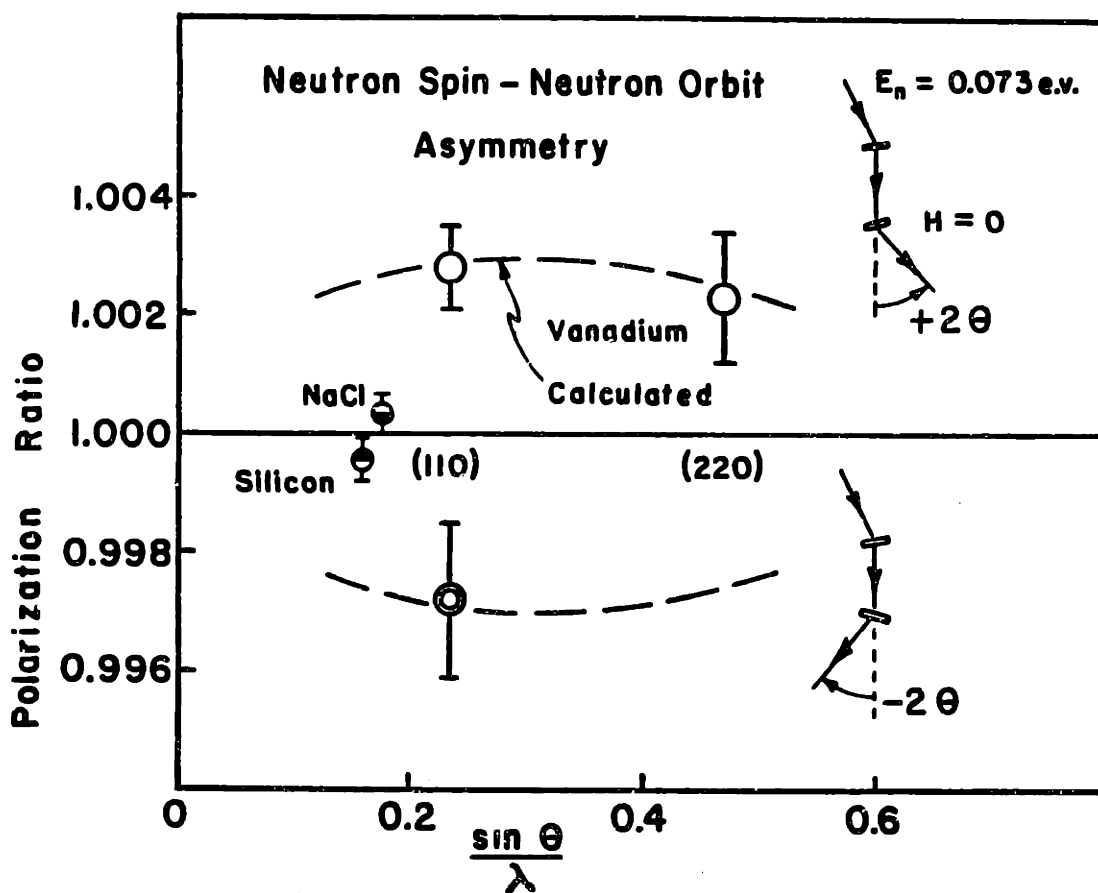


Fig.(2.16) Neutron polarization dependent asymmetry in the scattering of slow neutrons by vanadium with zero applied magnetic field. Two types of polarization ratio measurements were carried out: one for scattering from left to right, the second for the reversed direction of scatter.

Appendix A2.3

What is sought is the G -th coefficient in the Fourier transform of the SO scattering potential (2.3.3); we begin by Fourier transforming the electric field inside the crystal.

$$\begin{aligned}\vec{E}(\vec{r}) &= \sum_{\vec{G}} \vec{\epsilon}_{\vec{G}} e^{i\vec{G} \cdot \vec{r}} \\ &= -\vec{\nabla}_{\vec{r}} \left\{ \int_{crystal} \frac{N(\vec{R})}{|\vec{r} - \vec{R}|} d^3\vec{R} + \int_{crystal} \frac{n(\vec{r}')}{|\vec{r} - \vec{r}'|} d^3\vec{r}' \right\}.\end{aligned}\tag{A2.3.1}$$

Both the nuclear and electronic charge densities may be expanded in Fourier series,

$$\begin{aligned}N(\vec{R}) &= \sum_{\vec{G}} N(\vec{G}) e^{i\vec{G} \cdot \vec{R}} \\ n(\vec{r}') &= \sum_{\vec{G}} n(\vec{G}) e^{i\vec{G} \cdot \vec{r}'}.\end{aligned}\tag{A2.3.2}$$

We define the following change of variables:

$$\vec{r} - \vec{R} = -\vec{R}', \quad \vec{r} - \vec{r}' = -\vec{\rho}.$$

Using these expressions and the charge densities, the electric field (A2.3.1) may be written

$$\vec{E}(\vec{r}) = -\vec{\nabla}_{\vec{r}} \sum_{\vec{G}} e^{i\vec{G} \cdot \vec{r}} \left\{ N(\vec{G}) \int \frac{e^{i\vec{G} \cdot \vec{R}'}}{|\vec{R}'|} d^3\vec{R}' + n(\vec{G}) \int \frac{e^{i\vec{G} \cdot \vec{\rho}}}{|\vec{\rho}|} d^3\vec{\rho} \right\}. \quad (A2.3.3)$$

The integrals are evaluated by using a relation of Fourier transforms [19] which says that they are each equal to $\frac{4\pi}{G^2}$.

The crystal electric field is thus

$$\begin{aligned} \vec{E}(\vec{r}) &= \sum_{\vec{G}} \vec{\epsilon}_{\vec{G}} e^{i\vec{G} \cdot \vec{r}} = -\vec{\nabla}_{\vec{r}} \left(\sum_{\vec{G}} e^{i\vec{G} \cdot \vec{r}} \frac{4\pi}{G^2} \{N(\vec{G}) + n(\vec{G})\} \right) \\ &= -\sum_{\vec{G}} e^{i\vec{G} \cdot \vec{r}} \left(\frac{i4\pi\vec{G}}{G} \{N(\vec{G}) + n(\vec{G})\} \right), \end{aligned} \quad (A2.3.4)$$

and the Fourier coefficients of the field are therefore

$$\vec{\epsilon}_{\vec{G}} = \frac{-i4\pi\vec{G}}{G} \{N(\vec{G}) + n(\vec{G})\}. \quad (A2.3.5)$$

The aim of this appendix is to evaluate the SO potential coefficients in terms of known quantities such as crystal structure factors, G vector magnitude, nuclear charge number, and fundamental constants. To do this it is necessary to determine the Fourier coefficients of the nuclear and electronic charge density in terms of such quantities. The

expression for the nuclear charge density may be evaluated in the same manner as the nuclear potential coefficients (2.3.1) since

$$N(\vec{R}) = eZ \sum_j \delta(\vec{R}_j)$$

$$N(\vec{G}) = \frac{1}{U} \sum_j eZ e^{-i\vec{G} \cdot \vec{R}_j} = \frac{eZ}{v_c} F'(\vec{G}). \quad (A2.3.6)$$

In this expression v_c is the volume per unit cell, Z is the charge number of the nucleus, e is the electron charge, and $\frac{1}{U} = \frac{1}{v_c}$. Because the electronic charge is continuously, rather than discretely distributed in the crystal, the evaluation of $n(\vec{G})$ is slightly more involved. However if the crystal is considered to be composed of identical atoms, and the effect of bonding between atoms is ignored, then it can be shown [20] that

$$n(\vec{G}) = -\frac{e}{v_c} f(\vec{G}) F'(\vec{G}) \quad (A2.3.7)$$

where $f(\vec{G})$ is the atomic scattering form factor associated with the atoms that compose the crystal. This expression differs from the nuclear coefficient (A2.3.6) only in the substitution of $f(\vec{G})$ for Z . These atomic form factors are calculated using sophisticated electronic wavefunctions, and are expressed as the ratio of the amplitude of X-rays

scattered from the atom to the amplitude for classical (Thompson) scattering from a single electron. The form factors are tabulated [21] versus scattering vector magnitude (G).

The G -th Fourier coefficient of the crystal electric field is finally written

$$\vec{\epsilon}_{\vec{G}} = -\frac{i4\pi\hat{G}F'(\vec{G})}{v_c G} e\{Z - f(\vec{G})\}. \quad (A2.3.8)$$

Only the electric field depends explicitly on the position vector \vec{r} .

Therefore the Fourier transform of the SO potential follows immediately from (2.3.3) and the expression for the momentum operator given in Section (2.3)

$$\begin{aligned} V_{so}(\vec{G}) &= \mu_n \left(\frac{eh}{2m^2 c^2} \right) \vec{\sigma} \cdot \left(\vec{\epsilon}_{\vec{G}} \times (-ih\vec{\nabla}) \right) \\ &= -2\pi\mu_n \left(\frac{eh}{mc} \right)^2 \frac{1}{v_c} \{Z - f(\vec{G})\} F'(\vec{G}) \frac{\vec{\sigma} \cdot (\hat{G} \times \vec{\nabla})}{G} \\ &= -C F'(\vec{G}) \frac{\vec{\sigma} \cdot (\hat{G} \times \vec{\nabla})}{G} \end{aligned} \quad (A2.3.9)$$

where $C = 2\pi\mu \left(\frac{eh}{mc} \right)^2 \frac{1}{v_c} \{Z - f(G)\}.$

End Notes

1. H.Rauch and D.Petrascheck, in Neutron Diffraction, edited by H.Dachs (Springer, Berlin,1978).
2. N.Kato,Naturforsch. **28a**, 604-609 (1973).
3. N.W.Ashcroft, N.D.Mermin Solid State Physics, Saunders College Phila. P.A.
Pg. 139.
4. S. Takagi, Acta Cryst. **15**, 1311-1312 (1962).
5. P.P.Ewald, Acta Cryst. **11**, 887 (1958).
6. N.Kato, Acta Cryst. **11**, 885 (1958).
7. C.Kittel, Introduction to Solid State Physics (Wiley,New York,1976), 5-Th. Ed., Pg. 219.
8. Anton Zeilinger, et.al., Phys.Rev.Lett. **57**, 3089 (1986).
9. Kato,N. Z.Naturforsch. **15a**, 369 (1960).
10. Handbook of Mathematical Functions (edited by M.Abramowitz and I.A.Stegun), N.B.S. publication AMS 55, 409 (1964).
11. J.Arthur, M.A.Horne Phys. Rev. B **32**, 5747 (1985).
12. C.G.Shull, Neutron Interactions with Atoms, from the proceedings of a conference at Georgia Institute of Technology, published by Oak Ridge National Laboratory
13. H.Rauch and D.Petrascheck, Neutron Diffraction, edited by H.Dachs (Springer-Verlag,Berlin,1978), p.306.
14. M.L.Goldberger and F.Seitz, Phys. Rev. **71**, 294 (1947).
15. C.G.Shull and J.A.Oberteuffer, Phys. Rev. Lett. **29**, 871 (1972)
16. J.Schwinger, Phys. Rev. **73**, 407 (1948)
17. C.G.Shull, Phys.Rev.Lett. **10**, 297 (1963).
18. J.Schwinger op. cit.
19. G.L.Squires, Introduction to the Theory of Thermal Neutron Scattering (Cambridge Univ. Press, Cambridge,England 1978) Appendix B, (B.11).
20. C.Kittel, op.cit., 4-th. edition, pg. 77.
21. See the reference to The International Tables of X-Ray Crystallography in Chapter III.

Chapter III - Neutron Spin-Pendellösung Resonance

The discussion in the previous chapter presented a description of two independent phenomena, namely (a) the existence of a pendellösung structure in the propagation of diffracting neutrons through a crystal and (b) the identification of a neutron spin-neutron orbit interaction in the scattering of thermal neutrons. The present chapter will demonstrate that there is a coupling between the two effects which becomes very pronounced under resonant conditions and it is this phenomenon which forms the topic of this thesis. Before presenting the rigorous quantum mechanical treatment which is necessary in describing the effect, some introductory concepts will be given which may offer the reader some intuition into the basic physics behind the topic.

Section 3.1 - Introductory Concepts of NSPR

Following the early definitive experiments on pendellösung and spin-orbit scattering effects, it had occurred to Shull[1] that the two effects could be resonantly coupled so as to enhance the visibility of the spin-orbit interaction in an experiment. As has been seen in Section (2.4), the magnitude of the SO effects are generally very small relative to contributions from nuclear interactions, thus, any improvement

in sensitivity to measurements of SO effects would aid experimental searches for unrecognized forms of SO interaction. He reasoned that pendellösung oscillations are representative of a repetitive scattering process in which the momentum expectation vector alternates between the forward and Bragg directions as the neutron propagates into the crystal. The periodicity of this is spatially characterized by the pendellösung length (typically of the order 0.1 mm).

Recalling the discussion in Section (2.4), one can say that the sense of scattering defined by the unit vector \hat{n} changes sign every half pendellösung length. It also implies that the contribution of the SO potential relative to the nuclear interaction potential changes sign periodically (providing there is no change of neutron polarization) with the depth of neutron flow in the crystal. This SO perturbation would thus be self-cancelling over an even number of half pendellösung lengths and a crystal of this thickness would show forward directed Bragg diffraction unperturbed by SO interaction. However, for diffraction in the Bragg direction, there must be an odd integral number of half pendellösung lengths matched to the thickness, and this would imply that the SO perturbation would be effective only in the last half-pendellösung-length layer of the crystal.

On the other hand, if in some way the sense of neutron polarization is reversed during the neutron flight through the crystal in a matched way to the pendellösung periodicity, one

might expect a cumulative contribution of the SO interaction when combined with the fixed nuclear interaction. It also might be expected that the net amplification would depend upon the number of pendellösung oscillations being experienced by the neutrons in passing through the crystal. The oscillatory neutron polarization can be obtained most easily by exploiting Larmor precession in a suitably directed magnetic field applied to the crystal.

This phenomenological model is very suggestive of a simple mechanical analog, namely that of a swinging pendulum when subjected to a periodic tapping force. If the taps are presented at the swing extremes (where the time rate of momentum change is greatest) with reversed sense at successive extremes relative to the gravitational force, the net effect averaged over an even number of half swings would be zero. It follows also that observation during the last of an odd number of half swings would show only the effect of a single tap impulse. This corresponds to the case of constant neutron polarization.

Continuing with the tapped pendulum analog, if the taps are presented at the extremes in the same sense as the gravitational force, a resonant condition develops with resultant pendulum amplitude being determined by the number of oscillations before observation. This corresponds to the case of neutron polarization being reversed and matched to the pendellösung oscillation. Although this simple model is not

helpful in a quantitative interpretation of the neutron effects, some of its features are very helpful in a conceptual viewing of the physics that is involved in NSPR. It represents an extension of the coupled-pendula model that Ewald had used in the very earliest days to justify some of the remarkable phenomena predicted by dynamical diffraction theory and in fact led to his selection of the name pendellösung.

Section 3.2 - Dynamical Diffraction Description of NSPR

Our first goal is to derive the T.T. equations that properly take account of the potential which was illustrated in Fig. (2.10). This potential is composed of three contributions.

$$V(\vec{r}) = V_{Nuc.}(\vec{r}) + V_{SO}(\vec{r}) + V_{Ext.} \quad (3.2.1)$$

The first two terms have the spatial periodicity of the crystal and hence may be expanded as a Fourier sum over the reciprocal lattice vectors and using the notation of (D2.1.1) one finds

$$v(\vec{r}) = \sum_{\vec{G}'} v_N(\vec{G}') e^{i\vec{G}' \cdot \vec{r}} + \sum_{\vec{G}'} v_{so}(\vec{G}') e^{i\vec{G}' \cdot \vec{r}} + v_{ext}. \quad (D3.2.1)$$

In Section (2.3) we derived the exact form of these potential coefficients. It was found that the last two terms in (D3.2.1) represent the potential energy of a neutron magnetic moment in a magnetic field. The quantum mechanical prescription for such a potential implies that the coefficients of these terms may be represented as 2x2 matrices. It is also useful to write the neutron wave function in the form of a 2-element column, accounting for the two components of neutron spin.

$$\psi(\vec{r}) = \sum_{\vec{G}} \begin{pmatrix} a_{\vec{G}}^+(\vec{r}) \\ a_{\vec{G}}^-(\vec{r}) \end{pmatrix} e^{i(\vec{K} + \vec{G}) \cdot \vec{r}} \quad (3.2.2)$$

As in Section (2.1) the functions $a(\vec{r})$ will be assumed to vary slowly on the scale of the neutron wavelength. Their position (and + , - designation) in the column vector imply that they are the amplitude components for spin along and against some quantization axis.

In appendix (A3.2) the procedure laid out in Section (2.1) is followed to arrive at the following form for the T.T. equation. In the two beam approximation this set of coupled differential equations becomes

$$\left[i\vec{I}\vec{K} \cdot \vec{\nabla} - \frac{\vec{v}_{ext}}{2} \right] \begin{pmatrix} a_0^+ \\ a_0^- \end{pmatrix} - \left[\vec{I} \frac{v_N(-G)}{2} - i \frac{CF(-G)}{2|G|} \overleftrightarrow{\sigma} \cdot (\vec{G} \times \vec{K}) \right] \begin{pmatrix} a_c^+ \\ a_c^- \end{pmatrix} = 0 \quad (3.2.6)$$

$$- \left[\vec{I} \frac{v_N(G)}{2} + i \frac{CF(G)}{2|G|} \overleftrightarrow{\sigma} \cdot (\vec{G} \times \vec{K}) \right] \begin{pmatrix} a_0^+ \\ a_0^- \end{pmatrix} + \left[i\vec{I}(\vec{K} + \vec{G}) \cdot \vec{\nabla} - \frac{\vec{v}_{ext}}{2} \right] \begin{pmatrix} a_c^+ \\ a_c^- \end{pmatrix} = 0.$$

The double headed arrow notation is used to indicate the 2x2 matrix representation of the elements in this set of equations. The matrix "I" is simply the diagonal unit matrix and the potential coefficients inside the square brackets were derived in Section (2.3). A few observations about the wavefunction and T.T. equation may lend the reader some insight into their physical significance.

- a) The wavefunction (3.2.2) contains four functions which give the amplitudes for the neutron to be in any of four states: forward, spin up or down; Bragg, spin up or down.
- b) If we chose to re-write (3.2.6) such that the amplitude components are grouped together as a 4 element column, the T.T. equation becomes a 4x4 matrix equation. Assuming this is the case, each element of the large matrix is itself composed of sub-matrices and these sub-matrix elements represent the kinetic and potential energy of the neutron. In the spirit of Feynman[2] we can see from the large matrix that only the nuclear and SO potential coefficients (the off-diagonal terms) are capable of mixing forward and Bragg amplitudes. This is

physically reasonable (see Section (2.3)) because these terms represent the periodic potential of the diffracting lattice. On the other hand, the diagonal elements are made up of kinetic energy and external magnetic field operators. They are not periodic in space and thus do not represent processes that produce forward to Bragg amplitude transitions.

c) Within each element (square brackets) of the larger matrix are the terms that affect the neutron spin component amplitudes. The kinetic and nuclear potential terms are proportional to the diagonal unit matrix, they cannot mix orthogonal spin components. It is physically reasonable to expect that only the magnetic field derived potential terms will be responsible for representing precession of the neutron spin.

To proceed further we need to associate the quantization axis with a direction in space. The choice is now made that up (and down) are along (and against) the direction of the external magnetic field. To fix ideas the external magnetic field will point along the direction $-\vec{c}$ (i.e. along the Z-axis in the crystal). It will be shown (Section (3.4)) that the resonance behavior, to be derived shortly, will occur as long as the external field lies in the plane of scattering. Fig. (3.1) illustrates the geometry associated with spin and space coordinates.

We can now write the T.T. equation for this problem in the form in which it was originally considered. M.A. Horne [3]

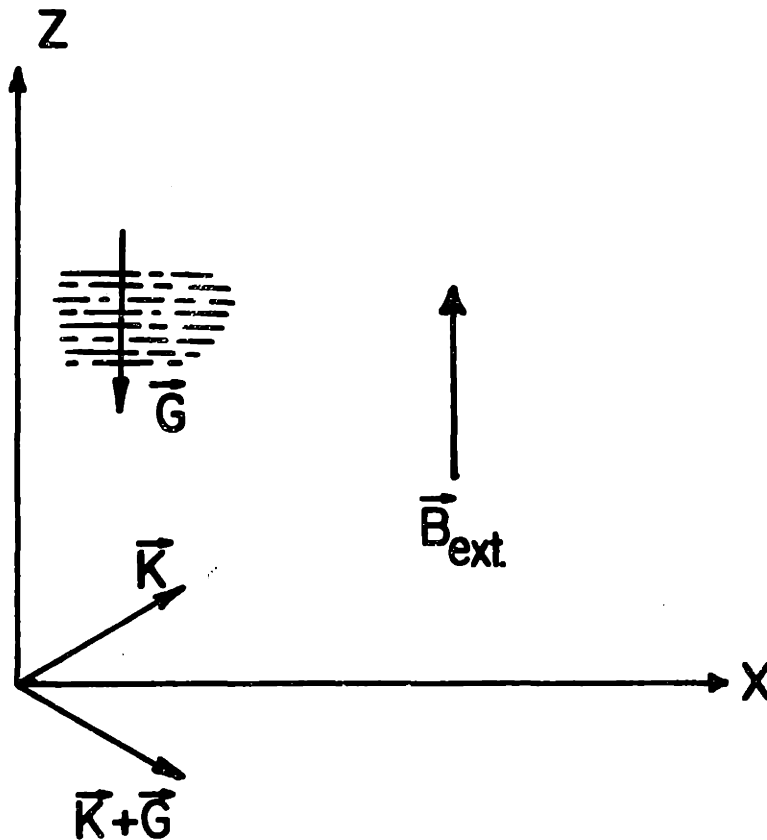


Fig.(3.1) The directions in the crystal associated with the spin and space coordinates discussed in the text. The axis of spin quantization, as well as the direction chosen for the applied magnetic field, is along Z .

first guessed the form of (3.2.7) by considering how each component of the potential we have discussed contributes to the behavior of a diffracting neutron.

$$\begin{pmatrix} -i\left(\frac{\partial}{\partial x} + \tan \theta \frac{\partial}{\partial z}\right) - \delta & 0 & A(-G) & H(-G) \\ 0 & -i\left(\frac{\partial}{\partial x} + \tan \theta \frac{\partial}{\partial z}\right) + \delta & -H(-G) & A(-G) \\ A(G) & -H(G) & -i\left(\frac{\partial}{\partial x} - \tan \theta \frac{\partial}{\partial z}\right) - \delta & 0 \\ H(G) & A(G) & 0 & -i\left(\frac{\partial}{\partial x} - \tan \theta \frac{\partial}{\partial z}\right) + \delta \end{pmatrix} \begin{pmatrix} a_0^+(\vec{r}) \\ a_0^-(\vec{r}) \\ a_c^+(\vec{r}) \\ a_c^-(\vec{r}) \end{pmatrix} = 0 \quad (3.2.7)$$

In the equation above, the off diagonal terms have the dimensions of reciprocal length and are written out explicitly as

$$A(G) = \frac{mV(G)}{h^2 K \cos \theta_B} = \frac{\pi}{\Delta_0}, \quad H(G) = \frac{mCF'(G)}{h^2 G} = \frac{\pi}{\Delta_{SO}}, \quad \delta = \frac{m\mu B_{ext}}{h^2 K \cos \theta_B} = \frac{\pi}{L_{precession}}. \quad (D3.2.2)$$

These three quantities characterize the strength of the nuclear, spin-orbit, and external magnetic field interactions respectively. The three energies $V(G)$, C , and $\mu B(ext)$, as well as the term $F'(G)$, were defined in Section (2.3). It may be recognized that $A(G)$ is one-half the distance, along the diameter (minimum distance between the branches), separating

the two branches of the hyperbola in Fig. (2.2).

The solutions to this set of four coupled differential equations (analogous to our Type 1 solutions in Section (2.1)) were found by H. Bernstein [4]. Although he solved the general problem we will be most interested in solutions that are independent of the z coordinate. These are the appropriate solutions when there are no entrance slits on the crystal and the incident neutron wave exactly satisfies Bragg's law. Below we "unstack" the 4 element column of (3.2.7) and define some short-hand notation as follows:

$$\begin{aligned} a^+ &= \begin{pmatrix} 1 \\ 0 \end{pmatrix} \left[e^{i\vec{k} \cdot \vec{r}} - e^{i(\vec{k} + \vec{c}) \cdot \vec{r}} \right] \\ a^- &= \begin{pmatrix} 0 \\ 1 \end{pmatrix} \left[e^{i\vec{k} \cdot \vec{r}} - e^{i(\vec{k} + \vec{c}) \cdot \vec{r}} \right] \\ b^+ &= \begin{pmatrix} 1 \\ 0 \end{pmatrix} \left[e^{i\vec{k} \cdot \vec{r}} + e^{i(\vec{k} + \vec{c}) \cdot \vec{r}} \right] \\ b^- &= \begin{pmatrix} 0 \\ 1 \end{pmatrix} \left[e^{i\vec{k} \cdot \vec{r}} + e^{i(\vec{k} + \vec{c}) \cdot \vec{r}} \right]. \end{aligned} \tag{D3.2.3}$$

The terms written in (D3.2.3) are reminiscent of the α and β states discussed in Section (2.1). The a^+ term describes a neutron with spin "up" relative to the quantization axis and where the spatial distribution of probability (like an alpha

state) is localized between the lattice planes. The remaining terms can be described in similar ways. The solutions of (3.2.7) which are independent of Z , and hence analogous to the on-Bragg ($y=0$) solutions given in (2.1.14) are

$$\begin{aligned}\alpha'_+(x, \delta) &= e^{i\sigma x} \{ (A + \delta + \sigma) a^+ - H b^- \} \\ \alpha'_-(x, \delta) &= e^{i\mu x} \{ (A - \delta + \mu) a^- + H b^+ \} \\ \beta'_+(x, \delta) &= e^{-i\mu x} \{ (A - \delta + \mu) b^+ - H a^- \} \\ \beta'_-(x, \delta) &= e^{-i\sigma x} \{ (A + \delta + \sigma) b^- + H a^+ \}\end{aligned}\tag{3.2.8}$$

$$\text{where } \sigma = \sqrt{(A + \delta)^2 + H^2} \quad , \quad \mu = \sqrt{(A - \delta)^2 + H^2} .\tag{D3.2.4}$$

The states (3.2.8) are the 3-potential generalizations of the nuclear α and β states derived in Section (2.1). The following properties of these states are worthy of mention.

1) They form a complete basis of states for the description of our NSPR problem as expressed in (3.2.7). Any incident neutron wave, satisfying Bragg's law exactly, may be expressed as a superposition of the states (3.2.8).

2) They are extremely simple functions of spin and space coordinates in that each describes two standing waves (along the Z direction) in the lattice: one associated with each of the two orthogonal spin states. The entire function is

multiplied by an overall phase in X . A physical meaning for these states will be presented in Section (3.4).

3) In the limit where $H = \delta = 0$ (no SO potential, no external field) the wavefields (3.2.8) reduce to the α and β states of the pure nuclear diffraction problem where each state is multiplied by a spinor corresponding to either of the two possible spin orientations.

4) Finally, it should be noted that we have not presented the solutions of (3.2.7) that correspond to off-Bragg wave propagation in the crystal. They will be discussed in Section (3.4). In addition, the quasi-point source solutions to this problem have, at this writing, not been found.

Section 3.3 - The NSPR Wavefunction; Predictions of Resonant Behavior

It is now appropriate to use the solutions of the NSPR problem, as stated in (3.2.8), to make predictions about the behavior of the neutron in a perfect crystal when there is a magnetic field present. These solutions are composed of plane waves that exactly satisfy Bragg's law inside the crystal and are now used to match the wavefunction associated with a plane wave incident on the crystal at the boundary. The goal is to calculate the intensity of the radiation exiting the crystal in the Bragg direction. First the wavefunction inside the crystal is written as a linear combination of the four functions of (3.2.8).

$$\Psi_{inside}(\vec{r}, \delta) = c_1 \alpha'_+ + c_2 \alpha'_- + c_3 \beta'_+ + c_4 \beta'_- \quad (3.3.1)$$

In keeping with the conditions which prevail in our experiment (Chapter IV) we assume the external magnetic field is uniform, existing both inside and around the crystal. The incident beam wavefunction, representing a pure spin state, may be written as a product of space and spin functions. We will consider radiation directed forward onto the crystal (with no slit on the entrance face) possessing one of the two

orthogonal spin orientations (i.e. along or against the external field direction). The two incident states may be written:

$$\text{Incident wave forward, spin up } \psi_+^F = \begin{pmatrix} 1 \\ 0 \end{pmatrix} |F\rangle \quad (3.3.2a)$$

$$\text{Incident wave forward, spin down } \psi_-^F = \begin{pmatrix} 0 \\ 1 \end{pmatrix} |F\rangle \quad (3.3.2b)$$

Matching (3.2.1) to each of these states at the crystal surface ($X=0$) leads to somewhat complicated forms for the wavefunction inside the crystal. Instead of writing them out explicitly we list the coefficients (the c 's of (3.3.1)) appropriate to the two incident states. For the state (3.3.2a) they are:

$$c_1 = \frac{1}{4\sigma}, c_2 = \frac{-H}{4\mu(A - \delta + \mu)}, c_3 = \frac{1}{4\mu}, c_4 = \frac{-H}{4\sigma(A + \delta + \sigma)}.$$

For the state (3.3.2b) one finds for the coefficients:

$$c_1 = \frac{H}{4\sigma(A + \delta + \sigma)}, c_2 = \frac{1}{4\mu}, c_3 = \frac{H}{4\mu(A - \delta + \mu)}, c_4 = \frac{1}{4\sigma}.$$

The symbols found in these coefficients are defined in Section (3.2).

The portion of the wavefunctions that represent the Bragg amplitude inside the crystal and that correspond to each of the two states (3.3.2) outside may be written:

$$\psi_{+}^B(x, \delta) = \frac{1}{2} \left\{ \begin{pmatrix} 1 \\ 0 \end{pmatrix} [\cos \mu x - \cos \sigma x] - i \left[\begin{pmatrix} A + \delta \\ -H \end{pmatrix} \frac{\sin \sigma x}{\sigma} + \begin{pmatrix} A - \delta \\ -H \end{pmatrix} \frac{\sin \mu x}{\mu} \right] \right\} \quad (3.3.3a)$$

$$\psi_{-}^B(x, \delta) = \frac{1}{2} \left\{ \begin{pmatrix} 0 \\ 1 \end{pmatrix} [\cos \sigma x - \cos \mu x] - i \left[\begin{pmatrix} H \\ A + \delta \end{pmatrix} \frac{\sin \sigma x}{\sigma} + \begin{pmatrix} H \\ A - \delta \end{pmatrix} \frac{\sin \mu x}{\mu} \right] \right\}. \quad (3.3.3b)$$

The $+(-)$ subscripts in the notation on the left side in (3.3.3) is meant to imply that these functions correspond to incident states with spin up(down) at the crystal entrance surface. The superscript B signifies that they are the Bragg amplitude functions inside the crystal.

An incident beam possessing any particular spin orientation may be written as a superposition of the two states (3.3.2a,b). An unpolarized beam would be written as a 50%-50% mixture (i.e. not a superposition) of these two states. Likewise, a beam written as a superposition of (3.3.2a,b) at the surface would imply the same superposition of (3.3.3a,b) representing the wavefunction inside. An unpolarized incident beam would imply a 50%-50% mixture of (3.3.3a,b) inside the crystal.

The wavefunctions (3.3.3) yield all possible information about the intensity and polarization of Bragg directed

neutrons inside (or exiting) the crystal.

We now examine the results of calculating the intensity associated with the functions (3.3.3).

1) The first important feature found is that both functions (3.3.3a,b) yield the same result for the intensity as a function of depth X and field parameter δ . This implies that the theory predicts an unpolarized beam may be used to search for the NSPR. This property of the diffracted intensity will allow for an important simplification in the design of an experiment.

2) The expression for the Bragg directed intensity exiting a crystal of thickness t , when a magnetic field (with field parameter δ) is present may be written:

$$I^B(t, \delta) = \frac{1}{2} \left\{ 1 - \cos \sigma t \cos \mu t + \frac{A^2 - \delta^2 + H^2}{\sigma \mu} \sin \sigma t \sin \mu t \right\} \quad (3.3.4)$$

where the symbols were defined in (D3.2.2) and (D3.2.4).

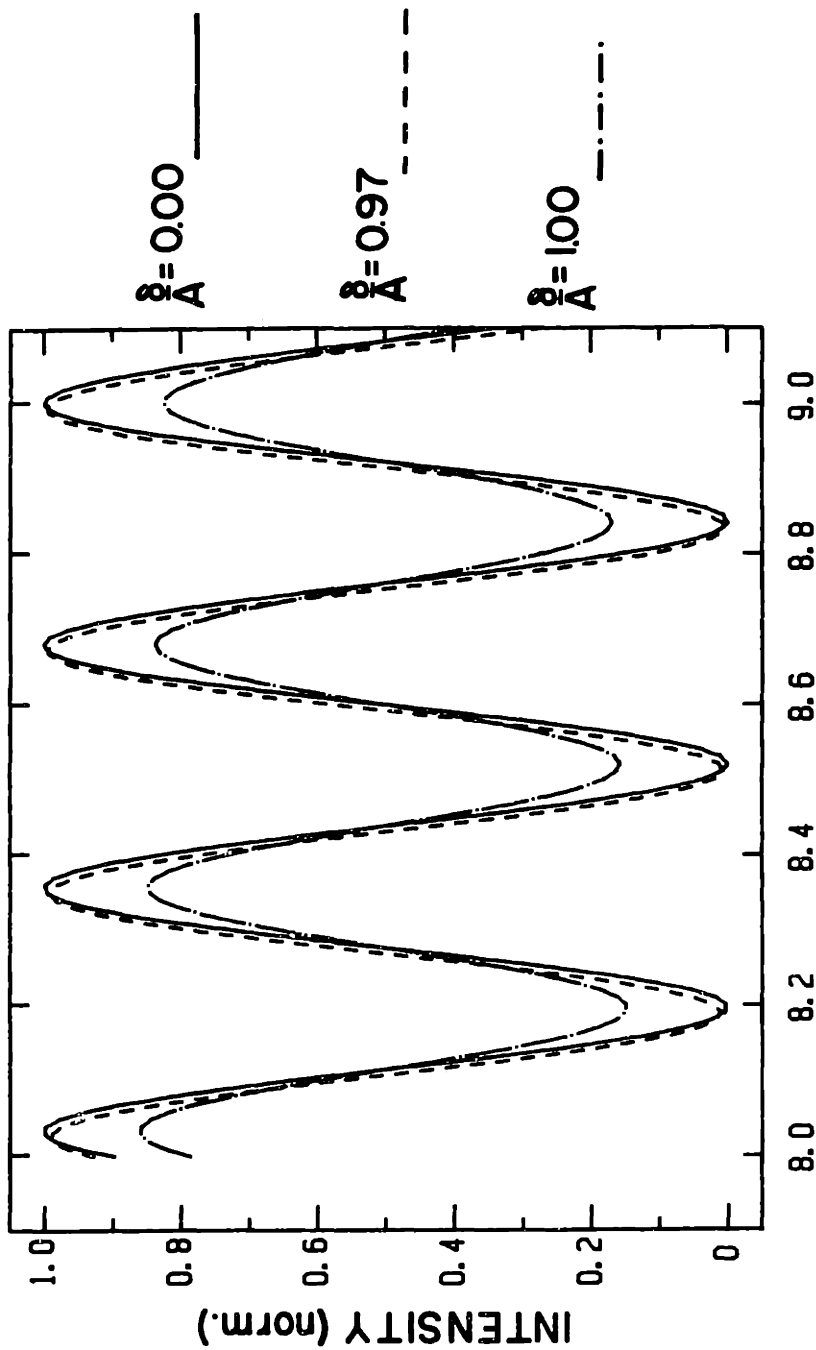
An important parameter must now be defined which gives the ratio of the strengths of SO to nuclear scattering. It can be written in terms of the inverse length parameters H and A of (D3.2.2) as follows:

$$\theta_{SO} = \frac{H}{A} = \frac{\Delta_0}{\Delta_{SO}} \quad (D3.3.1).$$

3) We plot this function in Fig. (3.2) below. The figure indicates the intensity as a function of wavelength. We have set the crystal thickness $t = 0.6\text{cm.}$ and, even though it has a wavelength dependence, we have fixed the parameter $\theta_{so} = \frac{1}{100}$.

The function is plotted for 3 different values of the normalized magnetic field parameter: $\delta/A = 0, 0.97, 1.00$. At $\delta/A = 0$ (no magnetic field) one finds the nuclear pendellösung behavior previously illustrated in Fig. (2.13). When $\delta/A = 1.00$ the resonance condition is satisfied and we see a dramatic change in the intensity. The plot for $\delta/A = 0.97$ looks much like that of the zero field case suggesting that the intensity changes occur only very close to the resonance condition. We may infer from Fig. (3.2) the possibility of some interesting measurements. For example, tuning the wavelength to produce a minimum pendellösung intensity at zero magnetic field should, at the resonance field, lead to an increase in measured intensity. The reverse situation is predicted at a pendellösung maximum.

4) Another view of (3.3.4) is given in Fig. (3.3) below. Here we have fixed the wavelength (and therefore A) to give a minimum in the pendellösung intensity at zero magnetic field. The figure shows the effect of scanning the magnetic field through the resonance condition. The result is given for 3 different thickness crystals: $t = (25, 35, 50) \lambda_0$. Again the parameter $\theta_{so} = 1/100$. Fig. (3.3) illustrates the type of



Bragg Angle (degrees)

Fig.(3.2) Theoretical prediction for the NSPR Bragg reflected intensity as a function of Bragg angle using (3.3.4) with $\frac{\theta_{SO}}{100}$.

The results are given for three different values of the applied magnetic field: 0, 97 and 100 percent of the resonance field. The results indicate that the influence of SO scattering is expected to appear only when the resonance condition is very nearly satisfied.

experiment which has actually been carried out (see Chapter IV) as part of this thesis.

5) Two important features of the resonance structures displayed in Fig. (3.3) are the height and width of each peak. Both of these quantities depend on the strength of the SO potential and the pendellösung fringe order (i.e. the ratio of crystal thickness to pendellösung length). It is interesting to evaluate (3.3.4) at resonance ($\delta = A$) and express the result in terms of the two pendellösung lengths defined in (D3.2.2). The result for the intensity, at resonance is

$$I^B(x, \delta = A) \cong \frac{1}{2} \left\{ 1 - \cos \frac{\pi x}{\Delta_{SO}} \cos \frac{2\pi x}{\Delta_0} \right\} + \text{Order} \left(\frac{\theta_{SO}}{4} \right)$$

Using some trigonometric identities this expression can be rewritten as

$$I^B(x, \delta = A) \cong \frac{1}{2} \left\{ \sin^2 \pi \left(\frac{1}{2\Delta_{SO}} + \frac{1}{\Delta_0} \right) x + \sin^2 \pi \left(-\frac{1}{2\Delta_{SO}} + \frac{1}{\Delta_0} \right) x \right\} + \text{Order} \left(\frac{\theta_{SO}}{4} \right)$$

Each of the sine terms in this last expression has the form of the (perfect Bragg) pendellösung oscillations discussed in section (2.4). The spatial frequencies associated with the two terms differ slightly from one another and from the case without SO interaction. One may think of the NSPR Bragg

NSPR Theory (pendellosung minimum)

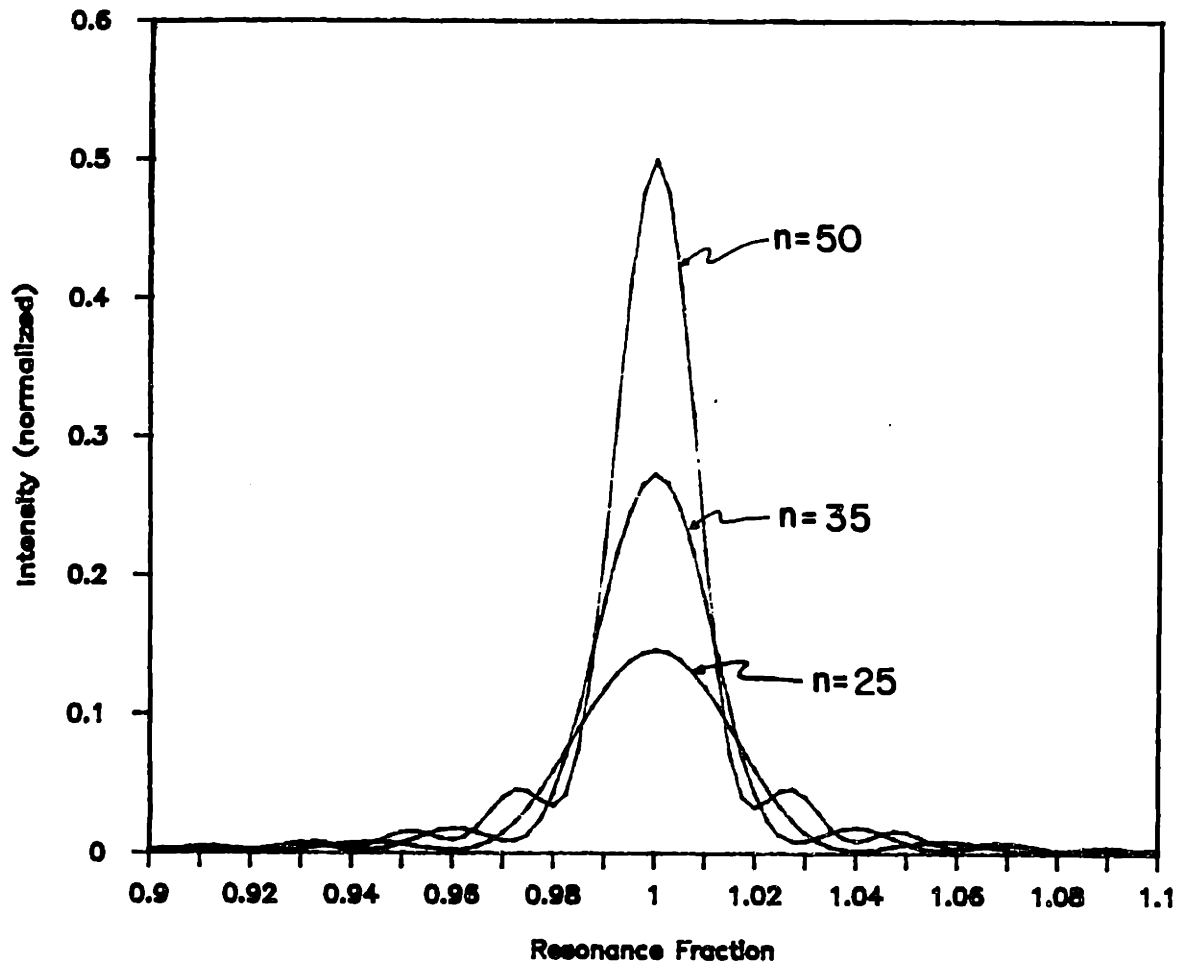


Fig.(3.3) Expected variation in NSPR intensity of Bragg diffracted radiation as a function of applied magnetic field strength. Results are given for three crystal thicknesses: 25, 35, and 50 pendellösung length units. The intensity is calculated using (3.3.4) which has a maximum value of 1. The field strength is normalized using the resonance field value and the strength of SO scattering is $\theta_{so} = \frac{1}{100}$.

directed intensity at resonance as being contributed to by two separate pendellösung processes. We shed light on these two processes in the next section.

Section 3.4 - An Alternative Derivation of NSPR Theory

We shall now discuss an alternative derivation of the solutions (3.2.8) which describe dynamical diffraction in a lattice where the nuclear, spin-orbit, and applied magnetic field potentials all act on the neutron. In so doing an effort will be made to elucidate the physics underlying our quantum mechanical treatment of the NSPR problem. It is hoped that the ideas presented in this section can provide a model with which to think about the problem of a neutron propagating in the 3-potentials described in Section (2.3). The discussion will rely heavily on three preliminary concepts.

- a) The 3-potential diagram, Fig. (2.10) which is discussed in Section (2.3).
- b) The α and β states (including spin) of the nuclear diffraction problem which were derived in Section (2.1).
- c) The quantum mechanical description of a magnetic moment in a magnetic field.

The 3-potential picture of the crystal lattice with an external magnetic field is presented in Fig. (3.4) with the lattice planes (dashed lines) drawn through the center of the nuclear potential. This re-positioning of the planes (from Fig. (2.10)) represents no change in the physics, but it does simplify the expression (3.4.1). By recognizing the 90 degree

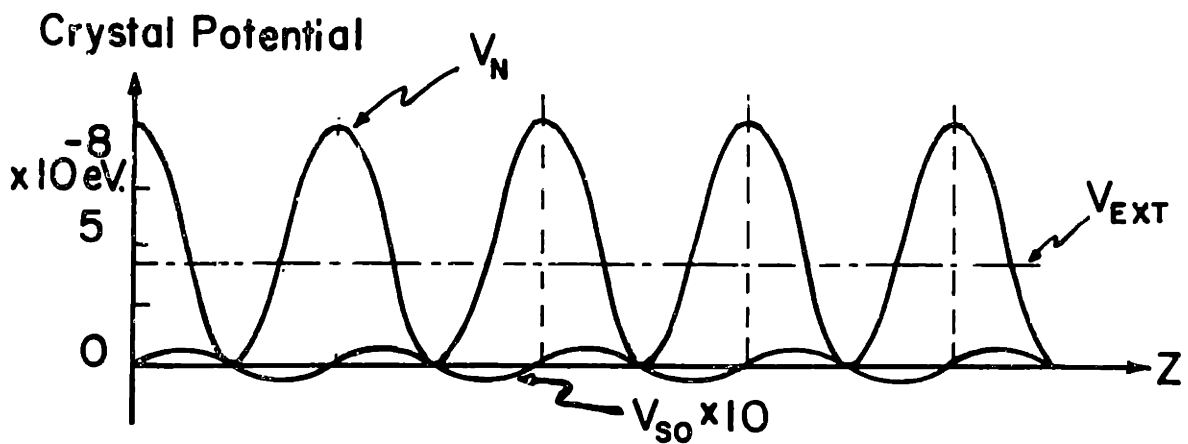


Fig.(3.4) The three potentials used in the description of NSPR which were originally displayed in Fig.(2.10) and discussed in Section (2.3).

(1/4 lattice spacing) phase shift between the two corrugated potentials in the figure we can re-express their sum so that the total potential may be written

$$V(Z) = V_N(0) + V_{ext.}(\delta) + \sqrt{V_N^2 + V_{so}^2} \cos\left(\frac{2\pi Z}{d} + \phi\right) \quad (3.4.1)$$

where $\phi = \tan^{-1}\left(\frac{V_{so}}{V_N}\right) \cong \tan^{-1}\left(\frac{1}{100}\right).$

Let us recall the α and β , or natural base states, of the neutron-nuclear diffraction problem and consider only the states that correspond to perfect-Bragg wave propagation inside the crystal. These two states are represented on the dispersion hyperbola (see Fig. (2.2)) by the diameter tie-points; their spatial frequencies differ by $2A(G)$. They may be interpreted as probability waves which are periodic in the direction normal to the lattice planes (along Z) and propagate (in the X direction) along the planes at a constant speed

$$v_x = \frac{P_x}{m} = \frac{\hbar K \cos \theta B}{m}. \quad (D3.4.1)$$

These states are represented on the left side in Fig. (3.5). After multiplying them by the two orthogonal spinors, these states are rewritten using the notation of (D3.2.3) on the right side of the figure.

The diagram illustrates wavefields α and β originating from points on the left. From point α , two lines extend to the right: an upper line labeled $\alpha_+ = \begin{pmatrix} 1 \\ 0 \end{pmatrix} e^{i\Lambda x} (|F\rangle - |B\rangle)$ and a lower line labeled $\alpha_- = \begin{pmatrix} 0 \\ 1 \end{pmatrix} e^{i\Lambda x} (|F\rangle - |B\rangle)$. From point β , two lines extend to the right: an upper line labeled $\beta_+ = \begin{pmatrix} 1 \\ 0 \end{pmatrix} e^{-i\Lambda x} (|F\rangle + |B\rangle)$ and a lower line labeled $\beta_- = \begin{pmatrix} 0 \\ 1 \end{pmatrix} e^{-i\Lambda x} (|F\rangle + |B\rangle)$.

Fig.(3.5) The α and β wavefields of the nuclear diffraction problem are re-written to include the possible orientations of the neutron spin on the right side of this figure. The exponential phase factor may be associated with either the spin component or the momentum part of the wavefields.

In these expressions the following notation was used for simplification: $|F\rangle = e^{i\vec{K} \cdot \vec{r}}$, $|B\rangle = e^{i(\vec{K} + \vec{c}) \cdot \vec{r}}$.

In reviewing the quantum mechanical description of a magnetic moment in a magnetic field we defer to the excellent presentations of Bohm [5], Baym[6], and others. It is sufficient to report that the natural states of such a problem are the ones for which the moment lies along and against the field. If the moment has a positive sign, the spin aligned with the field is said to have an associated energy $E = -\mu B$ with B being the magnitude of the magnetic field. There is a quantum mechanical phase associated with this energy which is written $e^{\frac{i\mu B T}{\hbar}}$.

In general in these diffraction problems, neutrons travel at a constant drift speed (given by (D3.4.1)) parallel to the lattice planes [7]. In our problem the time (T) may therefore be replaced by distance along the planes, X. Thus if this magnetic field is present and the spin is aligned along it, the afore-mentioned quantum phase would be written $e^{\frac{i\mu_B X}{\hbar v}}$. The opposite orientation of the spin implies the opposite sign for the phase.

Before beginning the alternative derivation of the functions (3.2.8) it should be noted that this approach is not an approximation. It is an exact translation of the mathematics expressed in the T.T. equation (3.2.7).

Consider the process of diffraction due to the nuclear lattice. The phases of the functions listed in Fig. (3.5) are a result of this process. It is however, interesting to interpret these phases as being associated with the spinors instead of with the spatial part of the wavefunctions. Making this association immediately implies that the 4 states break up into two pairs. By virtue of the particular combination of phase with spin for each state we would naturally connect the phases of our states with pseudo-magnetic fields as follows:

α_-, β_- are the natural
states in the field \vec{B}_N .

α_+, β_+ are the natural
states in the field \vec{B}'_N .

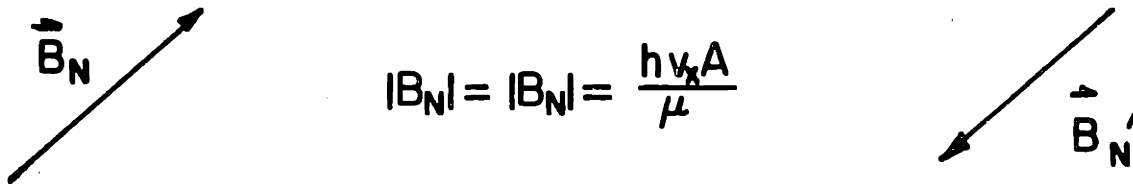


Fig.(3.6) A pseudo-magnetic field may be used to represent the nuclear potential when a neutron interacts with a crystal and the dynamical diffraction description (for exact Bragg incident radiation) is used.

In Fig. (3.6) we have interpreted the corrugated nuclear lattice potential in terms of two pseudo-magnetic fields. The

magnitude of the fields depends on the strength of the lattice potential and wavelength of the neutrons. In the case of 1\AA neutrons and the (111) reflections in silicon, $B_N \approx 6500$ Gauss.

Next, consider the case of the nuclear and SO potentials. Together they form another corrugated lattice potential, the strength of which is given in (3.4.1). One can show that the diffraction phase associated with this new lattice changes A to $\sqrt{A^2 + H^2}$. Because A and H add as the sum of their squares, the corresponding pseudo-fields must be orthogonal. The magnetic fields associated with this new lattice are illustrated in Fig. (3.7) where the magnitude of the SO pseudo-field is about 55 Gauss. Note that the 4 states of Fig. (3.5) are no longer eigenstates in the combined fields of Fig. (3.7).

Finally we consider the additional effect of our external magnetic field. In Section (3.2), the axis of quantization was chosen along this field. It is a simple matter to include this adjustable magnetic field (which we denote B_0) along with the two pseudo-fields. This is done in the figure that follows.

One may add the three fields, in each case, to produce an effective field. These are drawn as dashed lines in Fig. (3.8). On the right side of the figure we see that for an appropriate value of applied field, the effective field matches the SO field. Because of the relative sizes of SO and nuclear fields, this matching is very sensitive to the size of the external field. No such matching condition occurs on the

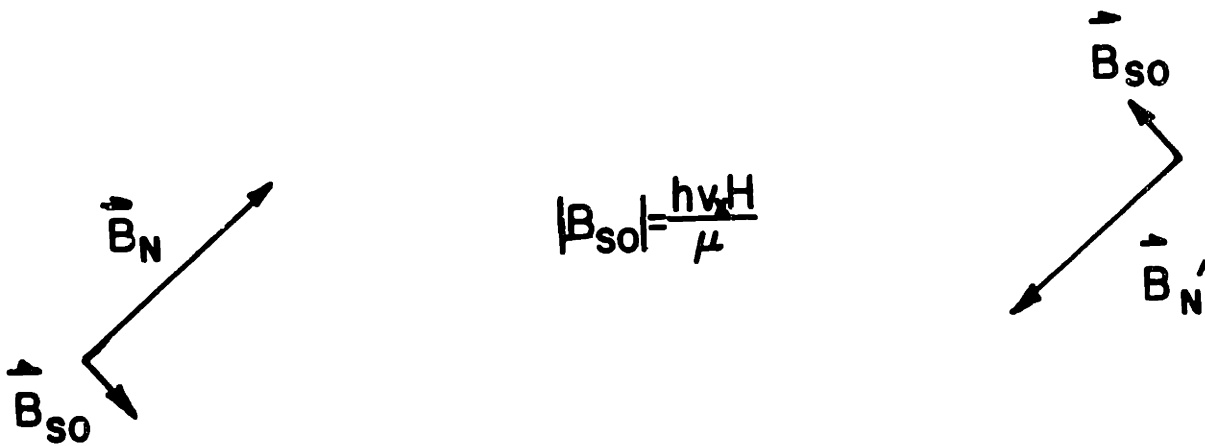


Fig.(3.7) The pseudo-field representation of the neutron-crystal potential when both the nuclear and SO interactions are considered.

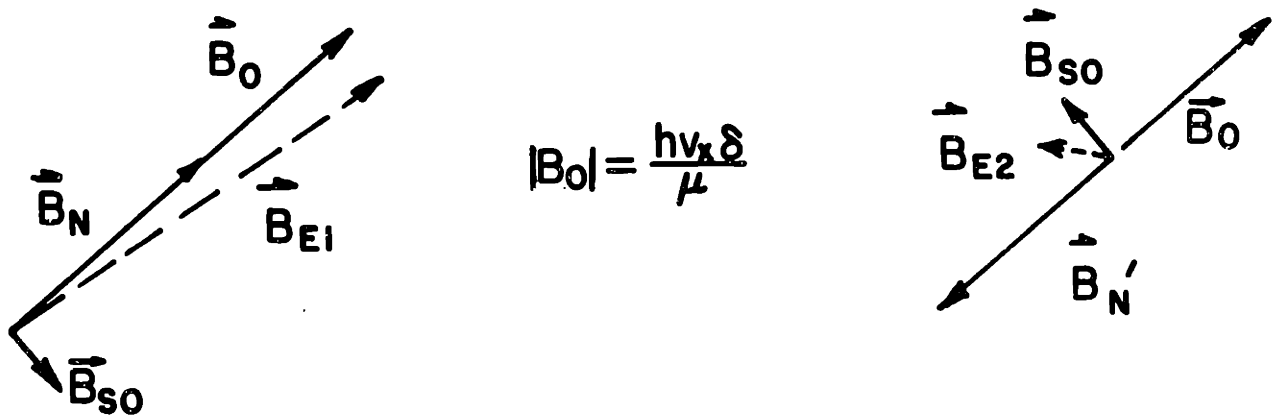


Fig.(3.8) With all three potentials (of Fig.(3.4)) present, the pseudo-fields may be added together to form an effective field, which in the case illustrated on the left, can be very sensitive to the size of the external magnetic field.

left side of the figure. We denote the right side field, resonant while the left side is anti-resonant.

Now that the three potentials have been represented in the form of fields, the problem is to find the natural states associated with the two effective fields. We know they must be the states with spin along and against the effective field in each case. On the left side in Fig. (3.8) the natural states will be a superposition of the orthogonal states α^+ and β^- , while on the right side the superposition will be made up of the states α^- and β^+ . We again refer to standard quantum mechanics texts, for the method of obtaining the desired solutions. The solution is given below in (3.4.2) as

$$\begin{aligned}\alpha'_{+} &= e^{i\sigma x} \left\{ [B_N + B_0 + B_{E1}] \alpha^+ - B_{S0} b^- \right\} & \alpha'_{-} &= e^{i\mu x} \left\{ [B_N - B_0 + B_{E2}] \alpha^- + B_{S0} b^+ \right\} \\ \beta'_{-} &= e^{-i\sigma x} \left\{ [B_N + B_0 + B_{E1}] b^- + B_{S0} \alpha^+ \right\} & \beta'_{+} &= e^{-i\mu x} \left\{ [B_N - B_0 + B_{E2}] b^+ - B_{S0} \alpha^- \right\}\end{aligned}\tag{3.4.2}$$

where we have used $\sigma = \frac{\mu_n B_{E1}}{h v_x}$, $\mu = \frac{\mu_n B_{E2}}{h v_x}$.

The subscript, n is used here to distinguish the inverse length μ from the neutron magnetic moment μ_n .

Using the relations between the fields and parameters A, H, and δ , it can be shown that (3.4.2) is identical to the solutions (3.2.8). The following features of this new way to view NSPR are worth mentioning.

- 1) The NSPR crystal diffraction problem has been re-cast into the quantum mechanical problem of a spin in a magnetic field. From this perspective, the four solutions (3.2.8) are clearly the natural states of the 3 potentials of our problem.
- 2) One symmetry of this problem is that the quantization axis (thus external field) may take any orientation in a plane perpendicular to the SO pseudo-field without affecting the result. In Section (2.3) it is shown that the SO magnetic field points normal to the plane of scattering. Therefore the external field may lie anywhere in that plane without changing the predicted results.
- 3) From Section (3.3) it is known that an incident wave will excite a superposition of (3.2.8) states at the crystal boundary. Our present discussion allows us to think of such a superposition as a spinor which in general is found to have amplitude associated with each of the two fields in Fig. (3.8). The wavefunction inside the crystal is simply the sum of these two amplitudes and describes the precession about the two fields.
- 4) This new way of viewing the NSPR problem may be extended to derive the solutions of the T.T. equation (3.2.7) that correspond to off-Bragg incident waves at the crystal boundary. This extension is quite straight forward, but it will not be discussed in detail in this thesis.

Appendix A3.2

This appendix will bridge the gap between the Schrödinger equation (SE) (2.1.1) and the T.T.equation (3.2.6) that describes the NSPR crystal diffraction problem. We use (D3.2.1) as the expression representing the three potential discussed in Section (2.3), and the wavefunction (3.2.2). The procedure follows exactly the same steps, and uses the same assumptions that were used in Section (2.1.1) to derive the T.T. equations in the case of the nuclear crystal potential.

It is useful to begin by grouping the potential expression (D.3.2.1) in two parts, separating the constant and position dependent terms.

$$v(\vec{r}) = (v_N(0) + v_{ext.}) + \sum_{\vec{G} \neq 0} e^{i\vec{G} \cdot \vec{r}} (v_N(\vec{G}) + v_{so}(\vec{G})) \quad (D3.2.1')$$

Inserting this expression into the SE along with the wavefunction (3.2.2) allows the equation to be written in a form analogous to (2.1.3).

$$\begin{aligned} \sum_{\vec{G}} \left\{ \left(-(\vec{K} + \vec{G})^2 + \nabla^2 + (k^2 - v_N(0) - v_{ext.}) \right) \begin{pmatrix} a_{\vec{G}}^+ \\ a_{\vec{G}}^- \end{pmatrix} + 2i\vec{\nabla} \begin{pmatrix} a_{\vec{G}}^+ \\ a_{\vec{G}}^- \end{pmatrix} \cdot (\vec{K} + \vec{G}) \right\} e^{i(\vec{K} + \vec{G}) \cdot \vec{r}} \\ - \sum_{\vec{G} \neq 0} e^{i\vec{G} \cdot \vec{r}} (v_N(\vec{G}) + v_{so}(\vec{G})) \begin{pmatrix} a_{\vec{G}}^+ \\ a_{\vec{G}}^- \end{pmatrix} e^{i(\vec{K} + \vec{G}) \cdot \vec{r}} \} = 0 \end{aligned} \quad (A3.2.3)$$

As in Section (2.1), we assume that $a(\vec{r})$ varies slowly and this implies that certain term in the previous expression are much smaller than others. In the present case two terms are small enough to ignore, one is the term $\nabla^2 a(\vec{r})$ and the other is found by examining the second part of (A3.2.3),

$$- \sum_{\vec{G}' \neq 0} e^{i(\vec{K} + \vec{G}' + \vec{G}) \cdot \vec{r}} \left\{ \left[v_N(\vec{G}') + i \frac{2mC}{h^2} F'(\vec{G}') \frac{\vec{\sigma} \cdot (\vec{G}' \times (\vec{K} + \vec{G}))}{G} \right] \begin{pmatrix} a_{\vec{G}}^+ \\ a_{\vec{G}}^- \end{pmatrix} + \frac{2mC}{h^2} \frac{F'(\vec{G}')}{G} \cdot \vec{\sigma} \cdot (\vec{G}' \times \vec{\nabla}) \begin{pmatrix} a_{\vec{G}}^+ \\ a_{\vec{G}}^- \end{pmatrix} \right\}$$

The third term in the last expression is can be shown to be about one million times smaller than the term that proceeds it, by ignoring it we may write (A3.2.3) as follows

$$\begin{aligned} \sum_{\vec{G}} \left\{ \left([-(\vec{K} + \vec{G})^2 + (k^2 - v_N(0) - v_{ext.})] \begin{pmatrix} a_{\vec{G}}^+ \\ a_{\vec{G}}^- \end{pmatrix} + 2i \vec{\nabla} \begin{pmatrix} a_{\vec{G}}^+ \\ a_{\vec{G}}^- \end{pmatrix} \cdot (\vec{K} + \vec{G}) \right) e^{i(\vec{K} + \vec{G}) \cdot \vec{r}} \right\} \\ - \sum_{\vec{G}} \sum_{\vec{G}' \neq 0} e^{i(\vec{K} + \vec{G} + \vec{G}') \cdot \vec{r}} \left[v_N(\vec{G}') + iC \frac{F'(\vec{G}')}{\vec{G}'} \vec{\sigma} \cdot (\vec{G}' \times (\vec{K} + \vec{G})) \right] \begin{pmatrix} a_{\vec{G}}^+ \\ a_{\vec{G}}^- \end{pmatrix} = 0 \end{aligned} \quad (A3.2.4)$$

The two beam (single set of diffracting planes) approximation now leads to a coupled set of equations

$$\begin{aligned} \left([-K^2 + (k^2 - v_N(0) - v_{ext.})] + 2i \vec{K} \cdot \vec{\nabla} \right) \begin{pmatrix} a_0^+ \\ a_0^- \end{pmatrix} - \left[v_N(-\vec{G}) - iC \frac{F(-\vec{G})}{\vec{G}} \vec{\sigma} \cdot (\vec{G} \times (\vec{K} + \vec{G})) \right] \begin{pmatrix} a_{\vec{G}}^+ \\ a_{\vec{G}}^- \end{pmatrix} = 0 \\ \left([-(\vec{K} + \vec{G})^2 + (k^2 - v_N(0) - v_{ext.})] + 2i(\vec{K} + \vec{G}) \cdot \vec{\nabla} \right) \begin{pmatrix} a_{\vec{G}}^+ \\ a_{\vec{G}}^- \end{pmatrix} - \left[v_N(\vec{G}) + iC \frac{F(\vec{G})}{\vec{G}} \vec{\sigma} \cdot (\vec{G} \times \vec{K}) \right] \begin{pmatrix} a_0^+ \\ a_0^- \end{pmatrix} = 0 \end{aligned} \quad (A3.2.5)$$

Finally, by using the matrix forms of the kinetic and potential energy coefficients and the relation

$$K^2 = -v_N(0) + k^2$$

we obtain the T.T. equation for the NSPR problem.

$$\left[i\vec{l}\vec{K} \cdot \vec{\nabla} - \frac{\vec{v}_{ext}}{2} \right] \begin{pmatrix} a_0^+ \\ a_0^- \end{pmatrix} - \left[\vec{l} \frac{v_N(-G)}{2} - i \frac{CF(-G)}{2|G|} \vec{\sigma} \cdot (\vec{G} \times \vec{K}) \right] \begin{pmatrix} a_c^+ \\ a_c^- \end{pmatrix} = 0 \quad (3.2.6)$$

$$- \left[\vec{l} \frac{v_N(G)}{2} + i \frac{CF(G)}{2|G|} \vec{\sigma} \cdot (\vec{G} \times \vec{K}) \right] \begin{pmatrix} a_0^+ \\ a_0^- \end{pmatrix} + \left[i\vec{l}(\vec{K} + \vec{G}) \cdot \vec{\nabla} - \frac{\vec{v}_{ext}}{2} \right] \begin{pmatrix} a_c^+ \\ a_c^- \end{pmatrix} = 0.$$

End Notes

1. C.G.Shull, private communication.
2. R.P.Feynman R.Leighton M.Sands, Feynman Lectures on Physics Vol.3, (Addison-Wesley, Reading, Mass. 1965).
3. M.A.Horne unpublished (1985).
4. H.Bernstein, unpublished (1985).
5. D.Bohm, Quantum Theory (Prentice Hall, New York, 1951).
6. G.Baym, Lectures on Quantum Mechanics (Benjamin/Cummings Publishing Co., Reading, Mass. 1969).
7. C.G.Shull et.al., Phys.Rev.Lett. **44**, 1715 (1980).

Chapter IV - The Experimental Investigation of NSPR

The previous chapters have presented the basic concepts underlying pendellösung and neutron spin-neutron orbit scattering phenomena in crystals, and have given an analytic description of how the two effects may be coupled to form novel neutron spin-pendellösung resonance (NSPR) action. As emphasized in earlier discussion, the interest in this resonance effect arises from the possibility that it can provide a new regime of sensitivity in the experimental determination of spin-orbit scattering effects and indeed that it can encourage the search for new unrecognized interactions between neutrons and scattering atoms. The theoretical analysis leads to predictions about the sharpness and magnitude of the resonant effects and it remains for experiment to test these features and to exploit the observations in establishing spin-orbit parameters.

Before presenting the results of the present NSPR experiments, we shall discuss the experimental conditions that are necessary for the study of these effects and how they were met in practice in the present experiments. Basically, the measurement consists of first characterizing the pendellösung structure for the crystal by wavelength scanning and then performing magnetic field scanning at selected pendellösung phase positions. The NSPR structure that is expected should vary with the pendellösung phase position. After discussion

of the principal experimental factors to be addressed in preparing for a successful measurement, we illustrate the apparatus that was used to obtain the results given in Chapter V. In outlining the important features of this design, we discuss some of the problems (and their solutions) encountered in performance of the experimental study.

Section 4.1 - Necessary Conditions for Observation of NSPR

The conditions under which one would expect to observe pendellösung effects are also those that severely limit the diffracted signal intensity. In this section we outline the important design considerations in the NSPR experiment; we see the results of this effort presented in the following chapter. The first type of constraint that must be fulfilled to preform a successful experiment applies to pendellösung measurements in general, while the second type of condition is specifically due to the nature of NSPR phenomena.

Section 4.1.1 - Considerations in Controlling Pendellösung Phase

The first set of conditions which must be satisfied are the same as those needed to successfully observe pendellösung oscillations in a diffracting crystal. The expression (2.4.1b) gives the intensity of exiting radiation when a wave satisfying Bragg's law is incident, through a narrow slit on a thick, perfect crystal (arrayed for symmetric Laue transmission). This expression for the exiting intensity in the Bragg direction is re-written using (D2.1.3) and becomes

$$I^B(t, \theta_B, \Omega) = \frac{1}{\sqrt{1 - \left(\frac{\tan \Omega}{\tan \theta_B}\right)^2}} \sin^2 \left\{ At \sqrt{\tan^2 \theta_B - \tan^2 \Omega} + \frac{\pi}{4} \right\}. \quad (4.1.1)$$

In this expression t is the crystal thickness and Ω describes the energy flow direction within the crystal. Further, we recall from chapter II that

$$At \tan \theta_B = \frac{\pi}{\Delta_0}, \quad |\Omega| \leq \theta_B.$$

The geometrical factors are illustrated in Fig. (4.1).

The triangular area originating at the entrance point with opening angle $2\theta_B$, is called the Borrmann fan, it represents the span of diffracted neutron wave flow directions in the crystal. Let us consider radiation in the central part of this region (i.e. $\Omega \approx 0$). In this case the behavior of (4.1.1) is dominated by the pendellösung phase $\phi = \left\{ At \sqrt{\tan^2 \theta_B - \tan^2 \Omega} + \frac{\pi}{4} \right\}$.

Obtaining good, high contrast pendellösung structures implies that this phase must be well defined. In particular, for the present experiment, we shall want the values of crystal thickness and Bragg angle such as to produce a minimum in intensity corresponding to a phase of 25.00π radians. The adjacent maxima would then correspond to 24.50π and 25.50π radians on either side. Without considering background radiation effects, a phase uncertainty $\delta\phi$ less than about $\pi/20$ is required to insure a well defined minimum. This implies that the fractional uncertainty in phase should be less than about 1:500. Therefore the crystal thickness (t), Bragg angle (θ_B) and range of Ω exiting the crystal must be well controlled.

The experiment was performed with a perfect silicon

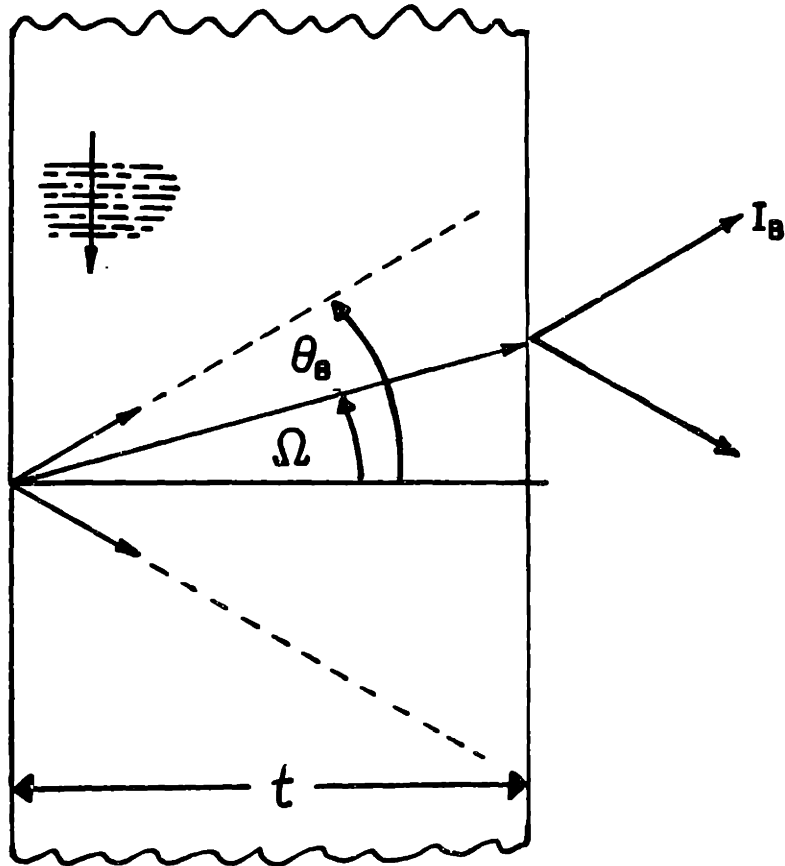


Fig.(4.1) The coordinates in the crystal that are relevant to the discussion of the pendellösung phase are the thickness t and wave flow direction Ω .

crystal the orientation of which allowed for symmetric Laue transmission using the (111) reflecting planes. Crystal thickness was controlled by a polishing method which guaranteed that the critical front and back faces be parallel. These faces were mechanically polished in successive steps and finally chemically polished to remove the mosaic surface layer. The final crystal thickness, ascertained by multiple measurements across the face, was $t = 5.5524(8)$ mm so that this parameter was more than adequate in meeting the above uncertainty criterion. For comparison, if variation in crystal thickness were the only factor contributing to $\delta\phi$ the 1:500 fractional uncertainty would imply an uncertainty in thickness of $\frac{\Delta_0}{20} \approx 0.010$ mm.

An uncertainty in Bragg angle $\delta\theta$, implies, by Bragg's law, an uncertainty in wavelength $\delta\lambda = 2d \cos\theta_B \delta\theta_B$. Control of this uncertainty is accomplished by high collimation of the incident beam. Two neutron limiting slits are used for this purpose one placed on the crystal entrance face (width 0.15 mm), and the other (width 1.00 mm) located 1.355 m upstream, between the NSPR crystal and a monochromating crystal next to the reactor face. The geometry of this slit configuration permits rays to enter the crystal over an extreme range of 3.0 minutes arc. Since the graphite monochromating crystal is highly mosaic, this implies that the perfect silicon crystal will be excited by wavelength

components whose Bragg angles will also range over an extreme of 3.0 minutes arc. Considered by itself, this range in θ , would produce a fractional uncertainty in the pendellösung phase (4.1.1) of 1:700 at the phase position of 25.00π radians, which again satisfies our above criterion for obtaining suitable pendellösung fringe visibility.

The critical entrance slit was fabricated from two sheets of cadmium (thickness 0.9 mm) with tapered edges defining the slit opening. The sheets were attached lightly to the polished face of the crystal with small dots of Duco cement placed well away from the opening, and the slit width was determined by optical microscopy. A reference face (accurately parallel to (111) planes) was available on one side of the crystal plate, and this was used to align the slit axis parallel to (111) planes. In order to reduce transparency of the cadmium sheets to possible higher order wavelength components in the collimated beam, a secondary oversize slit opening in boron-plastic was added over the assembly.

In observing pendellösung structure, it is also necessary to have spatial definition of the rays leaving the crystal. Accordingly a duplicate of the entrance slit assembly was prepared and attached to the exit face of the crystal. Again using the side reference surface of the crystal plate, the two slit axes could be made parallel and positioned so that their centers were accurately along the internal (111) planes. In this configuration, the mean angle of passage of radiation

through the slits is zero but there is a symmetrical range of the parameter α allowed by the use of finite slits. It can be shown that this introduces a fractional uncertainty in pendellösung phase of 1:300. This dominates over the other effects and represents the limiting resolution of the presently-used system.

Section 4.1.2 - Requirements on Controlling the Magnetic Field

The second set of conditions necessary for observing NSPR involve the magnetic field used to affect the resonance. By expanding the NSPR intensity function (3.1.12) in δ , about the resonance value $\delta = A$, it can be shown that the resonance width ϵ behaves like

$$\epsilon \propto \frac{\theta_{so}}{n}. \quad (4.1.2)$$

In this expression n is the fringe order, that is, the thickness of the crystal in pendellösung length units. We previously defined $\theta_{so} = H/A$.

The expression (4.1.2) is reasonable on physical grounds. The larger the strength of SO (relative to nuclear) scattering, the larger should be the range of magnetic field over which the influence will be felt. Less sensitivity in fulfillment of the resonance condition is then implied. Such a situation could have been anticipated by considering the relative sizes of the pseudo-fields discussed in connection with Fig.(3.8). The dependence of the width on n is justified by recognizing the resonance condition to mean that spin precession remains in phase with pendellösung momentum changes. A more stringent matching would be required as the number of cycles (pendulum lengths) increases. This is analogous to the conclusion for a

one-dimensional diffraction grating, namely that the sharpness of the diffraction pattern increases with the number of lines in the grating.

The expression (4.1.2) provides qualitative insight into factors affecting the width of the resonance peak. However it is more useful to quantitatively display the NSPR structure as it is expected to appear under the conditions appropriate to this experiment. In particular it is important to anticipate three features of the resonance action:

- a) the magnitude of magnetic field needed to satisfy the resonance condition,
- b) the width of the resonance structure relative to the size of the resonance field and,
- c) the expected change in neutron intensity (signal) as the magnetic field is adjusted through the resonance field value.

The resonance condition, first discussed in Section (3.1), implies that the Larmor precession length (the distance over which a neutron precesses by 2π radians as it travels through a uniform magnetic field) should equal the pendellösung length. Referring to (D3.2.2) the resonance condition thus implies

$$A(G) = \delta$$

and this implies

$$V(G) = \mu B_{ext}. \quad (4.1.3)$$

In the last expression $V(G)$ is the G -th Fourier component of the neutron-nuclear crystal potential (see (2.3.2)) and the neutron magnetic moment μ , has a magnitude of 1.913 nuclear magnetons. The strength of the externally applied magnetic field is given by B_{ext} .

Using (2.3.2) and Shull's [1] value for the product of the coherent nuclear scattering amplitude and Debye-Waller factor of the (111) reflection in silicon $(0.41053(8) \times 10^{-12} \text{ cm})$ gives

$$B_{ext.} \mid \text{at resonance} = 6279.3 \text{ Gauss.}$$

Note that the resonance condition (4.1.3) is independent of wavelength; it depends only on the nuclear scattering amplitude.

There is no simple expression that gives a precise value for the width of the resonance. One must first evaluate the ratio H/A and then plot the resonance function (3.3.4) appropriate to the experimental conditions. Again using (D3.2.2) and (2.3.2) one finds

$$\theta_{so} = \frac{H(G)}{A(G)} = \frac{\frac{\mu}{2} \{Z - f(G)\} \left(\frac{a^2}{mc^2} \right) \cot \theta_B}{b_{\text{silicon}}}. \quad (4.1.4)$$

Note this ratio is independent of Debye-Waller factor and that the numerator in the last term of (4.1.4) is the SO scattering length defined by Shull[2] and discussed in connection with (2.4.2). Evaluating (4.1.4) in the case of this experiment (where the Bragg angle will be adjusted to be around 8.7 degrees) gives

$$\theta_{so} \cong \frac{1}{120}.$$

In a typical NSPR experiment one begins the resonance measurement by adjusting the wavelength (at zero magnetic field) to produce, for instance, a minimum in the pendellösung pattern. The external magnetic field is then varied over a range through the resonance value. This provides a mapping of the resonance structure. Fig.(4.2) is a plot of the NSPR Bragg intensity (3.3.4) versus field parameter δ/A . The experimental parameters of crystal thickness, H/A , and Bragg angle have been chosen to match those used in this experiment. The Bragg angle is fixed to produce a minimum in the pendellösung intensity exiting the crystal, in the Bragg direction, at zero field (fringe order $n=25.00$). The resonance function (3.3.4) is normalized so as to have a maximum value of 1. In Fig.(4.2), it has been scaled (by 355 neutron/30 minutes) and a baseline has been added (180 neutrons/30 minutes). These numbers reflect the maximum

NSPR at Pendellosung Minimum

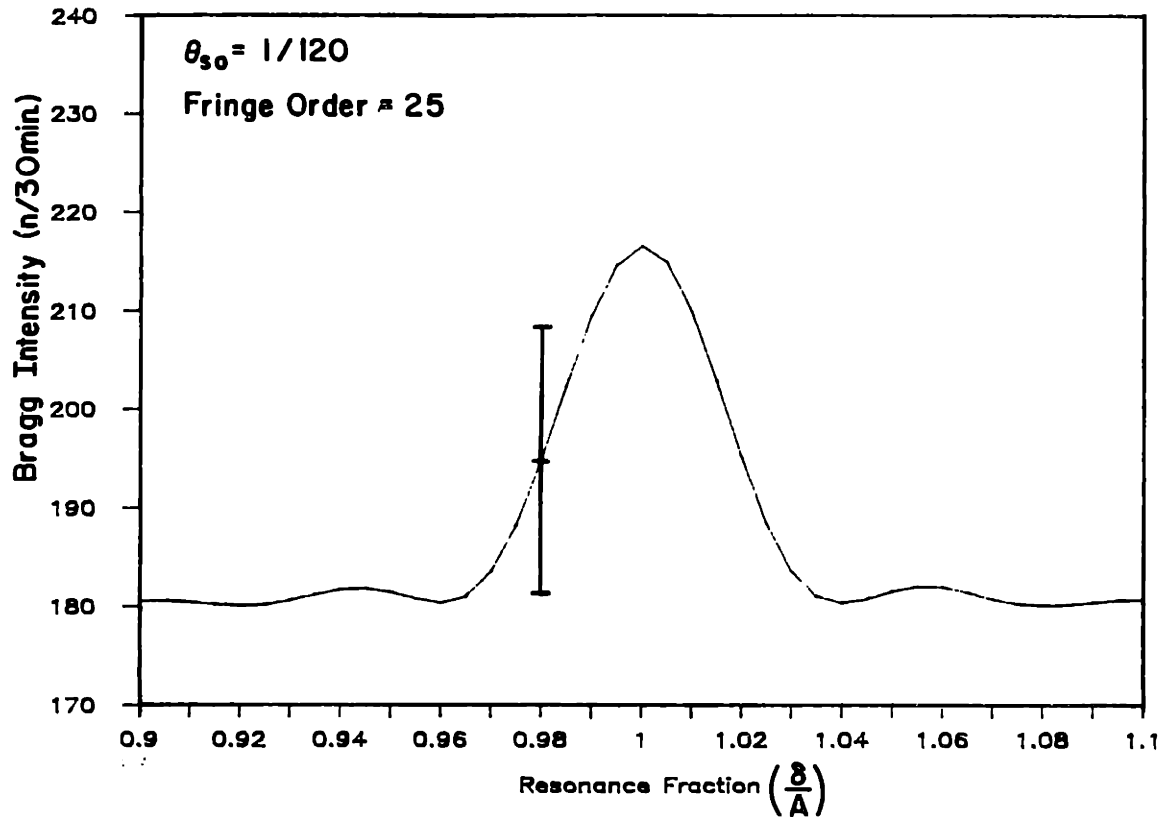


Fig.(4.2) The expected NSPR Bragg intensity calculated using the conditions expected to be present in the experiment. The error bar signifies the statistical error associated with the measurement of intensity.

change in intensity that has been observed in the pendellösung pattern (at zero field) as one scans over Bragg angle; the baseline is the minimum intensity recorded in the pendellösung pattern (see chapter V). For convenience, the horizontal axis is a normalized magnetic field parameter and the resonance condition is therefore $\frac{\delta}{A} = 1$.

The magnetic field width of the resonance peak (FWHM) is seen to be about 4% of the resonance field value for our experimental conditions. In order to resolve this structure it will be useful to examine it in small increments of perhaps 0.5%. Therefore the magnetic field must be tunable in fractional steps of 0.5% and possess stability commensurate with this definition. We have chosen to scan in magnetic field from below to above the NSPR position, over a range of 10-13%. By this procedure one obtains also a measurement of the reference baseline. Thus each resonance scan will involve 20-26 data points and between these points the magnetic field must be incremented in strength by about 30 out of 6000 Gauss. We discuss the magnet and field scan apparatus in Section (4.2.2).

The error bars indicated in Fig.(4.2) denote the statistical uncertainty (the square root of the number of counts) that would be expected from the measurement of NSPR intensity with counting intervals of 30 minutes. The signal sizes are small, typically 6-10 neutrons/minute. This is the

result of several factors: the flux available for the experiment which depends on absolute reactor power, reactor/beam port design, and location of the selected wavelength in the thermal neutron spectrum, along with the large sacrifice in intensity associated with the elaborate collimation required to observe pendellösung phenomena. Given the small signal strength, and in particular, the small difference in intensity $\Delta I(50)$ between background and NSPR peak, long counting times are required. One half hour count periods were chosen in this experiment. This time interval represents a compromise between short (1 minute period reactor power fluctuations) and long (6-12 hour drifts in reactor power) time scale changes in the flux of the incident beam. A summary of requirements for tuning the magnetic field is given below.

- 1) The resonance condition implies that the field strength be held fixed at about 6000 Gauss.
- 2) Resolving the resonance structure by field scanning implies a field scan step size of 0.5% (30 Gauss) or less.
- 3) Small neutron signals imply long count periods and many repetitions of a given field scan. These conditions require control of the magnetic field that is stable over periods of at least a week, and reproducible over many scans during that period.

Section 4.2 - The NSPR Experimental Arrangement

We begin this section with an overview of the experimental arrangement which is presented in Fig. (4.3). Following a brief introduction, the discussion of the apparatus in the figure is divided into parts which focus on three subsystems: the spectrometer system, magnet and control electronics, and the thermal isolation and temperature control system. As can be seen in the figure, a beam of thermal neutrons from the reactor source is incident on a pyrolytic graphite (mosaic) monochromating crystal oriented for (002) reflection. This beam of neutrons has a peak in its Maxwell-Boltzmann spectrum at wavelength about 1.1 Å. Before reaching the crystal the beam passed through a soller slit collimator which restricted the horizontal beam divergence to about 0.35 degrees. The graphite crystal, mounted with a vertical rotation axis, removes much of the gamma radiation and diffracts a neutron beam with a 4% range of wavelengths at 1 Å. The diffracted beam is then restricted by a boron-plastic slit of 1 mm width (previously described) located 16.5 cm from the monochromater axis. The beam then passes through a 42 cm long steel channel (not shown) surrounded by masonite and other neutron attenuating materials. Besides shielding stray neutron and gamma radiation this channel acts in limiting the beam height to about 2.5 cm

Before entering the thermally shielded region around the silicon (specimen) crystal, another boron-plastic slit of width 3 mm defines the beam in the horizontal plane. The silicon crystal (with slits described in Section (4.1)) is mounted so as to be centered between the poles of a large electromagnet. The field produced by the magnet points normal to the (111) reflecting planes of the crystal. This magnet and crystal assembly are supported by a table centered on a second rotation axis. The axis of rotation is centered in the neutron beam and lies along the 0.15 mm wide vertical entrance slit on the front face of the crystal. Both the crystal table and a 2.5 meter long arm can rotate freely and independently about the axis on a conical bearing assembly. The arm is used to support a cylindrical, neutron absorbing drum that shields the neutron detector. That portion of the incident neutron beam which is diffracted and exits through the back slit of the silicon crystal will pass through a masonite shield 70 cm long, along the drum axis and into the detector.

Finally, the crystal table and support bearing are supported on a massive plate which can move along a steel track anchored to the floor in the reactor building. In order to change the center of the wavelength band incident on the silicon specimen crystal, it is necessary to translate the second axis along the track. This movement changes the scattering angle relative to the direction of the beam

incident at the monochromator crystal. The first axis is then adjusted in order to maximize the radiation diffracted toward the specimen.

4.2.1 -**The Spectrometer System**

Although a general description of the spectrometer has been given, a few salient points require extra consideration. The choice of a semi-monochromated (narrow band) beam spectrometer rather than one using white radiation incident from the reactor source, was made primarily so as to minimize the neutron background radiation. As the discussion in Section (4.1.2) indicates, the signals we expect to measure are quite small. Further, in order to provide a uniform magnetic field, the gap between poles of the electromagnet is only large enough to permit the placement of the crystal. It was therefore judged that a broad spectrum (white) neutron beam in close proximity to the iron poles of the magnet would produce an excess in scattered background and this would increase the difficulty in performing the measurements. In addition the lessening of non-Bragg radiation scattered by the specimen crystal would prove helpful. A third factor in favor of using a semi-monochromated beam was the difficulty in safe handling of the intense radiation in a direct beam from the reactor.

One feature in the use of narrow band incident radiation proves to be troublesome. This problem can be recognized by considering the pendellösung wavelength fringes studied in the earlier investigation by Shull and discussed in Section (2.4.1) (see Fig. (2.13)). They were measured by rotation of

the pendellösung crystal about the front slit centered in a (white) beam with essentially uniform intensity over the range of wavelengths indicated. In contrast to this is the experiment done using a narrow band spectrometer where neutron radiation reaching the specimen crystal contains intensity only over a narrow wavelength window. The range of this window is determined by the angular width of the beam incident on the monochromating crystal and the mosaic width of this crystal. What one measures in rotating the pendellösung crystal in this case is the convolution of the pendellösung transmission function and the (approximately rectangular) band of wavelengths reflected by the monochromator. If the wavelength bands incident on the specimen were truly rectangular the resultant fringe pattern would be composed of well defined sections (with sharp cutoff edges) in the pendellösung oscillation. Unfortunately nature does not provide sharp edges in this case and it becomes quite possible to misinterpret the resulting distorted wavelength fringe pattern. This point is raised because just such a situation created problems in our experiment.

4.2.2 - The Magnet and Magnet Control System

The electromagnet used in the experiment is illustrated schematically in Fig. (4.3). It is composed of two iron cores which taper to a 2 inch diameter, flat pole surface adjacent to the crystal. Concentrically mounted on each core are two current coils wound with copper tape. The coils are individually water cooled by copper cooling plates that make up the coil side faces. The cores are each bolted to 14 inch square steel end plates and these end plates are bolted together by four threaded steel rods to form two sides of a box. Outside dimensions of the electromagnet are approximately 14 x 18 inches and the assembly weights about 400 pounds. The gap between pole surfaces can be precisely set by adjustment of the nuts used to hold the steel plates rigid to the rods. After assembly, the magnetic field between the poles was mapped using a Hall probe with sensitive area of 1 square mm. In the central section of the gap, the field was found to be uniform to within 0.04% (at the expected resonance field value) over the region of neutron propagation within the silicon crystal. One constraint imposed by this magnet geometry is that the large coils limit the permitted Bragg angle to a maximum of about 12 degrees with the selected gap width.

One of the conclusions from the discussion in Section (4.1.3) is that the magnetic field will need to be incremented

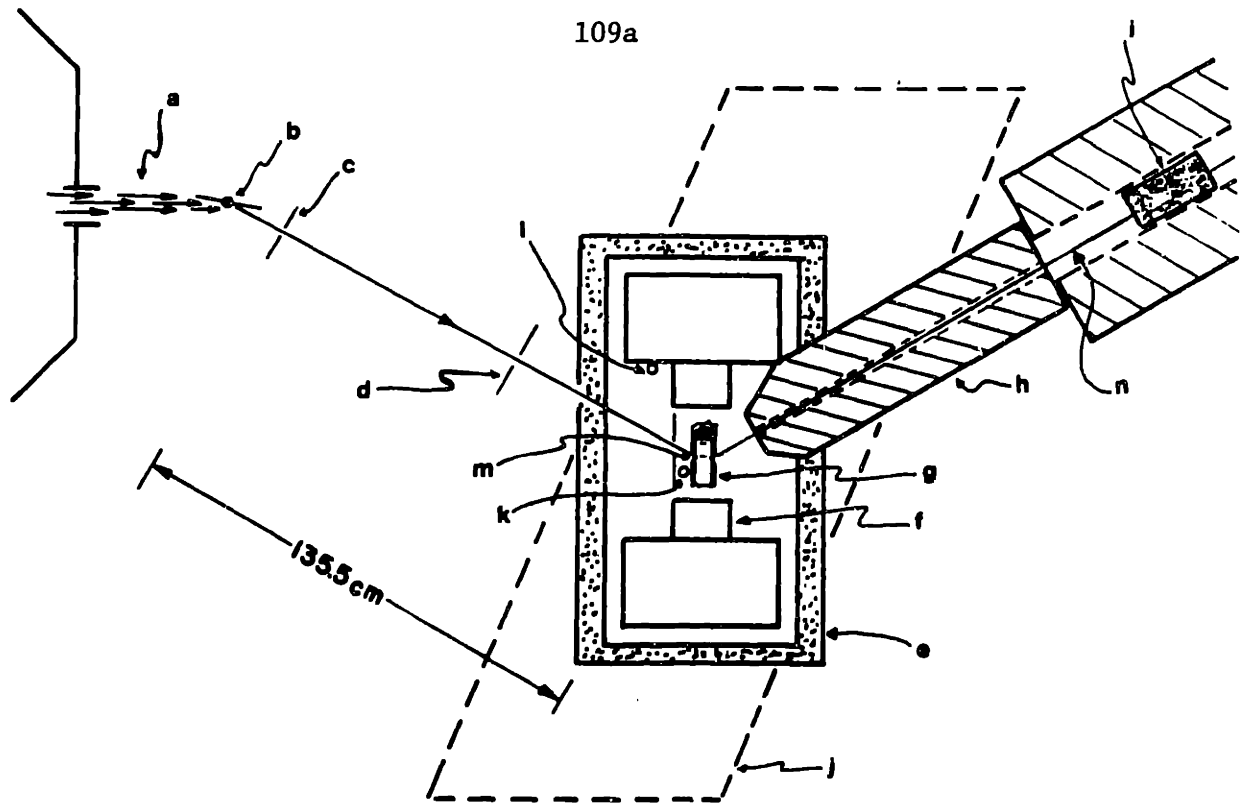


Fig.(4.3) An overview of the experimental apparatus used in the measurement of NSPR signals. A legend given here specifies the important parts of the assembly.

Legend:

- a) thermal neutron beam from reactor source
- b) mosaic monochromator crystal (first crystal rotation axis)
- c) 1 mm boron-plastic slit
- d) oversized, 3 mm, beam defining slit
- e) thermal shield around specimen crystal
- f) electromagnet (pole)
- g) specimen crystal (silicon (111) reflection orientation)
- h) masonite shield passing diffracted beam
- i) neutron detector
- j) spectrometer track
- k) Hall probe
- l) temperature sensor (for magnet cooling water control system)
- m) specimen crystal rotation axis (second axis)
- n) diffracted (signal) beam entering detector

in 0.5% steps over a range of roughly 12% about the resonance field value. The full field scan will take 12 hours (one half hour per step) and will be repeated 6-8 times per week. A principal criterion chosen to determine the design of instruments used to provide this degree of field stability and reproducibility was that these properties shall not vary by more than 0.1% while at the resonance field. As will be discussed, the magnet and crystal are enclosed in an environment in which temperature is held constant to within a range of 0.2 degrees C. Therefore the magnet current will be the limiting factor in fulfilling the above criteria.

Magnet current is provided by a Hewlett Packard 6269B General Purpose power supply. It is used as a remotely programmable, constant current source and with our magnet, the current at resonance is about 17.5 Amps. The magnet current is controlled by supplying the current source with a remotely derived D.C. voltage level equivalent to 10 mV input per 1 Ampere output. This voltage is obtained from a digitally controlled incrementing voltage reference (IVR) built specifically for this experiment. We describe this reference briefly as follows. It consists of three principle elements, all manufactured by Analog Devices, Inc. They are: a precision (constant) voltage reference (-5 Volts) model AD-584, a 3 1/2 digit binary coded decimal (BCD) monolithic CMOS digitally controlled potentiometer model AD-7525, and an ultra low offset voltage operational amplifier model AD-OP-07.

This system simply divides a very precise reference voltage into 2000 parts. It produces this signal in order to program the current supply, through an extremely stable, unity gain impedance buffer, that is the op-amp. The IVR can be preset manually by four BCD thumb wheel switches or it can increment in preset steps (as small as 0.001 of the resonance field current) on receiving a logic signal from a neutron pulse counting scalar. The general design of this IVR can be found in a data book published by Analog Devices [3]. In the table below are listed the manufacturers specifications that are relevant to our design criteria.

Output Spec.	HP-6269B	AD-584	AD-7525	AD-OP-07	Unit
Regulation	0.032	0.02	N/A	10E-4	%
Stability	0.09/8hr	0.0025/40d	Excellent	10E-6/30d	%
Tmp Coeff	0.011	0.003	0.005	10E-6	%/dg
Accuracy	N/A	0.03	0.05	N/A	%

In the table: hr = hour, d = day, dg = degrees C., N/A = not applicable.

The actual magnetic field strength has been monitored with a Hall probe, permanently mounted next to the crystal. Again, it has a stability limited by the Hall current provided to it. This current was measured to be stable to 0.0013%/week. The measured Hall voltage has been calibrated using a standard magnet with field strength calibrated against a standard

magnet at the Francis Bitter National Magnet Laboratory. The measured Hall voltages indicates that the original field criteria are being adhered to. All measurements of current and voltage are done using a Keithley Instruments 5 1/2 digit microvolt meter.

Section 4.2.3 - The Temperature Control System

The final aspect of the experimental arrangement which we discuss is the temperature control system. The critical need for a temperature control system was not appreciated until after the experiment was underway. The NSPR study began by ascertaining at zero magnetic field, the location of pendellösung wavelength fringes in terms of the experimentally controlled quantities. These quantities are: track position, and silicon crystal and monochromator crystal angle. Some of the results of these measurements are discussed in Chapter V. Subsequently, the central fringe minimum was chosen in order to study the stability, in time, of the pendellösung intensity. The results indicated that the intensity (at zero field) followed a daily cycle, closely correlated with room temperature changes. A typical example of this behavior is given in Fig.(4.4).

The indicated temperature data were obtained using thermocouples positioned on and around the silicon crystal. Subsequent experiments involving active heating of the crystal environment were carried out. They suggested that the pendellösung intensity was strongly influenced by temperature gradients, both in the space around the crystal, and in time. This evidence suggested that these gradients might be creating microscopic distortions in the crystal which in turn affected the pendellösung phase (Section (4.1)). It was this finding

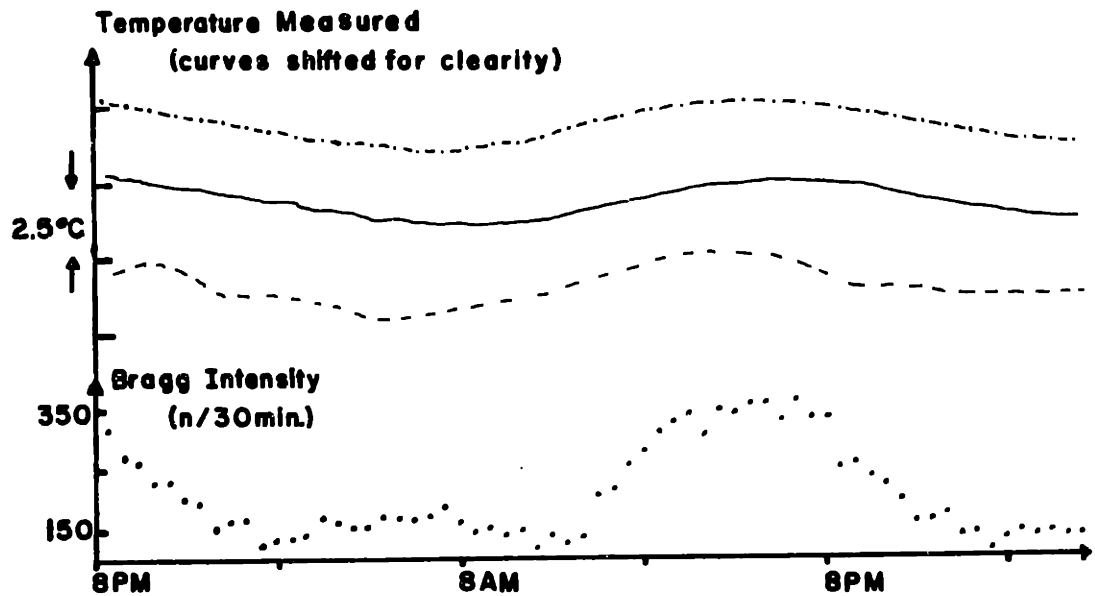


Fig.(4.4) The effect on the measured pendellösung intensity c_{\perp} changes in temperature in the environment of the crystal. The upper portion of the figure shows the temperature measured on and near the crystal; in the lower section the intensity measured at the fringe minimum is displayed on a common time axis.

which motivated the construction of the temperature control system described below.

In order to overcome the effects resulting from this temperature instability, steps were taken to thermally isolate the crystal from the room environment and the surrounding magnet coils. Regulation of the temperature of the magnetic cooling water was necessary so that the magnet coils could be held at a constant temperature over the power range necessary for field scanning. The silicon crystal and its plastic support pedestal were wrapped in a multiple layered blanket of aluminized mylar "superinsulation". Furthermore, the crystal, magnet, and support table were enclosed in a styrofoam box with a wall thickness of 1 inch. The neutron beam enters this enclosure through sealed windows made of two layers of mylar separated by the wall thickness. All four magnet coils were isolated from the crystal to prevent convective heat transfer to the crystal. In Fig. (4.3), a temperature sensor is indicated, mounted on the inner face of one of the magnet cooling plates. The response of this temperature sensor is fed back to the control unit of a Neslab RTE-4 water chiller which supplies temperature controlled cooling water for the electromagnet. The chiller contains a reservoir which is being cooled by a 600 Watt refrigerator and simultaneously heated by an immersion heater. The heater power is arranged to be proportional to the difference in temperature between the magnet coil and a controllable set point. A great

advantage of this arrangement is that magnet temperature remains constant throughout the 25% change in magnet power dissipation which accompanies a typical field scan.

With this control system, the crystal temperature remains within +/- 0.1 degrees C of the set point over long times irrespective of magnet power. Both the magnet and chiller unit are kept operating continuously in order to prevent the possibility of thermal shock to the crystal and to its mounting.

End Notes

1. C.G.Shull, op.cit.
2. C.G.Shull, op.cit.
3. 1984 Databook: Integrated Circuits Vol. 1, pp. 9-181.
(Analog Devices, Inc. 1984).

Chapter V - Results of Experimental Study

The conceptual description of pendellösung phenomena and of the NSPR has been presented in Chapters II and III. The conditions which must be fulfilled in order to measure these effects experimentally have been discussed in Chapter IV. In the present chapter, the results of measurements carried out to explore these predicted behaviors are outlined. We begin by presenting the measurements of pendellösung wavelength oscillations obtained at zero applied magnetic field. Next, the results of NSPR field scanning performed at three locations in the pendellösung fringe pattern are given. The results reported here support the prediction of a resonant enhancement of SO scattering. Further, theory suggests that the magnetic resonance structures obtained at a minimum, a maximum, and a point of inflection of the pendellösung intensity will be clearly distinguishable. Good agreement is found between measurement and the suggested variation in shape of the resonance curves. A Chi-squared minimization procedure is used to fit the measured NSPR field scan data to theory. From this analysis a quantitative measure of the strength of SO scattering for the silicon (111) reflection is obtained. An average value for this SO strength is assessed by applying this method to the entire body of data, collected over

approximately 1200 hours during the experiment. Finally, we compare the results of these measurements to an independently derived value for this same quantity.

Section 5.1 - Pendellösung Fringe Measurements

Before attempting to measure NSPR data it is necessary to adjust and measure the pendellösung phase, for it is this phase along with the strength of SO scattering that determines the size and shape of the NSPR peak structures. The method used in measuring the pendellösung wavelength fringes is dictated by the constraints imposed on experiment by the choice of a narrow band neutron spectrometer. These constraints are discussed in Section (4.2.2). Measurement of the wavelength fringe pattern is accomplished by determining the intensity of the Bragg diffracted radiation exiting the pendellösung crystal as the incident neutron wavelength is varied. The results of this measurement are given in Fig. (5.1) below.

The method employed in this measurement is quite straight forward. The variation in the wavelength diffracted by the silicon crystal is accomplished in a three step procedure which begins by translation of the pendellösung crystal along the spectrometer track shown in Fig. (4.1). With this movement, the angle of the radiation scattered off the monochromating crystal and incident on the pendellösung crystal is changed. It follows that the central wavelength in the band of wavelengths reaching the pendellösung crystal has been shifted. The second step is then to adjust the monochromater crystal to maximize the intensity reaching the

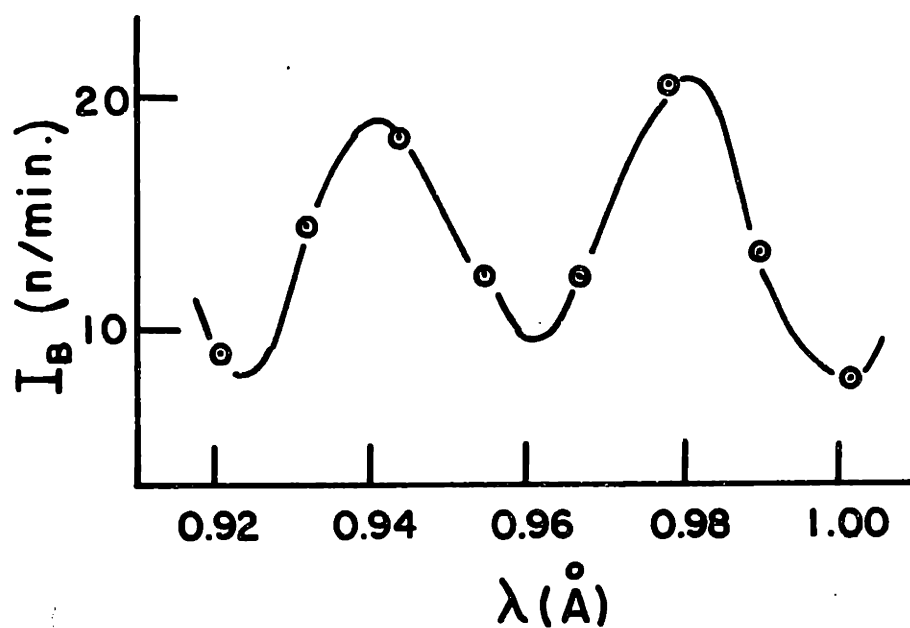


Fig.(5.1) Results of the measurement of pendel-lösung intensity (for the silicon (111) reflection) with changes in neutron wavelength. The experimental conditions are described in the text. The vertical axis is Bragg diffracted intensity in counts per minute.

silicon crystal and, finally, the pendellösung crystal angle is adjusted to accommodate this change in wavelength. A single absolute assessment of the wavelength diffracted by the pendellösung crystal is made near the center of the range of movement along the track. This measurement, along with knowledge of the spectrometer geometry (discussed in Chapter IV), allows for an accurate establishment of the wavelength of the radiation diffracted by the silicon crystal at every other track position.

The results given in Fig. (5.1) do not represent a precision measurement of pendellösung oscillations, but they were not meant to. These data indicate the broad features of the pendellösung structure in terms of the experimentally adjustable variables of track position, pendellösung crystal and monochromator crystal angle. In addition, this scan gives the first indication of visibility of the fringes and provides a bench mark against which to gauge the results of improvements in the experimental arrangement. Based on the results of this scan, improvements in the pendellösung slit system and mounting procedure were carried out.

Section 5.2 - NSPR Field Scanning Results

What is given in this section are the principal experimental results of this thesis, they are displayed in the form of NSPR magnetic field scan data. It is from these measurements, which were obtained by repeated scanning at three locations in the pendellösung fringe pattern, that the strength of SO scattering is assessed. A method for the quantitative evaluation of this scattering strength is discussed in Section (5.3). Here we discuss the experimental method and display typical field scan profiles obtained at what was the zero field pendellösung intensity minimum, maximum, and point of inflection. One crucial aspect of these measurements is, that they were performed with unpolarized neutrons and the reason that this was possible is discussed in Section (3.3).

The procedure that was followed in the NSPR measurements remained, for the most part, identical over about four months of experiments. Because of the operating schedule at the M.I.T. nuclear reactor the data were divided into four-day packages. Between five and eight complete field scans could be made during each of these periods. A typical field scan was one in which the applied magnetic field was incremented in 0.5% steps, over a 12-13% range in field from below to above the resonance. The scanning was generally performed by field stepping in one direction, namely up, so as to lessen the

effects of hysteresis is the electromagnet. Between scans, when the field is dropped to a low value, the magnet current was decreased in such a way that during the subsequent field scan the magnetic field always followed the same hysteresis curve of the electromagnet.

The first step in beginning a series of measurements (packages) at one fringe location was to characterize that location. This means adjusting the track location and graphite monochromator crystal angle so that the desired wavelength (and thus the appropriate pendellösung phase) is centered in the band of wavelengths incident on the silicon crystal. This procedure insured that the pendellösung crystal received the same intensity of radiation at each wavelength position. If this condition were not satisfied it would not be possible to inter-compare NSPR data obtained at different fringe locations. Next, a measurement of the neutron wavelength was made in order to provide a parameter that was essential to the data analysis described in Section (5.3).

The results of field scanning at the pendellösung maximum (fringe number $n=24.50$), inflection point ($n=24.75$), and minimum ($n=25.00$) are presented in Figs. (5.2), (5.3), and (5.4) respectively. In the case of Figs.(5.2) and (5.3) the points are the average of six consecutive field scans, while seven scans were averaged to give the results in Fig.(5.4). The vertical axis is given in the units of neutrons counted per 30 minutes at a constant reactor power (constant incident

NSPR Chisq. on data

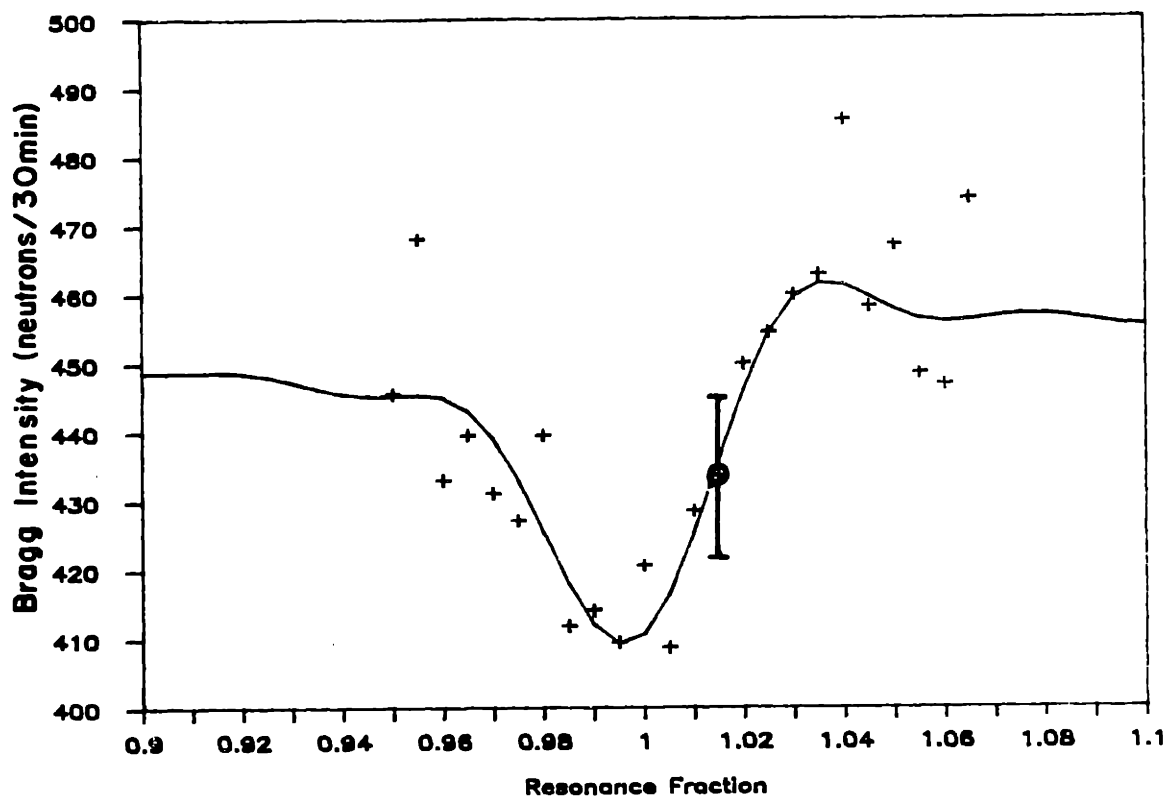


Fig.(5.2) Results of NSPR magnetic field scans taken at the zero field pendellösung maximum intensity position ($n=24.50$) in the silicon (111) Bragg reflection. The error bar indicates the typical measured standard deviation in the mean of the 6 scans which make up these data.

NSPR Chisq. on data

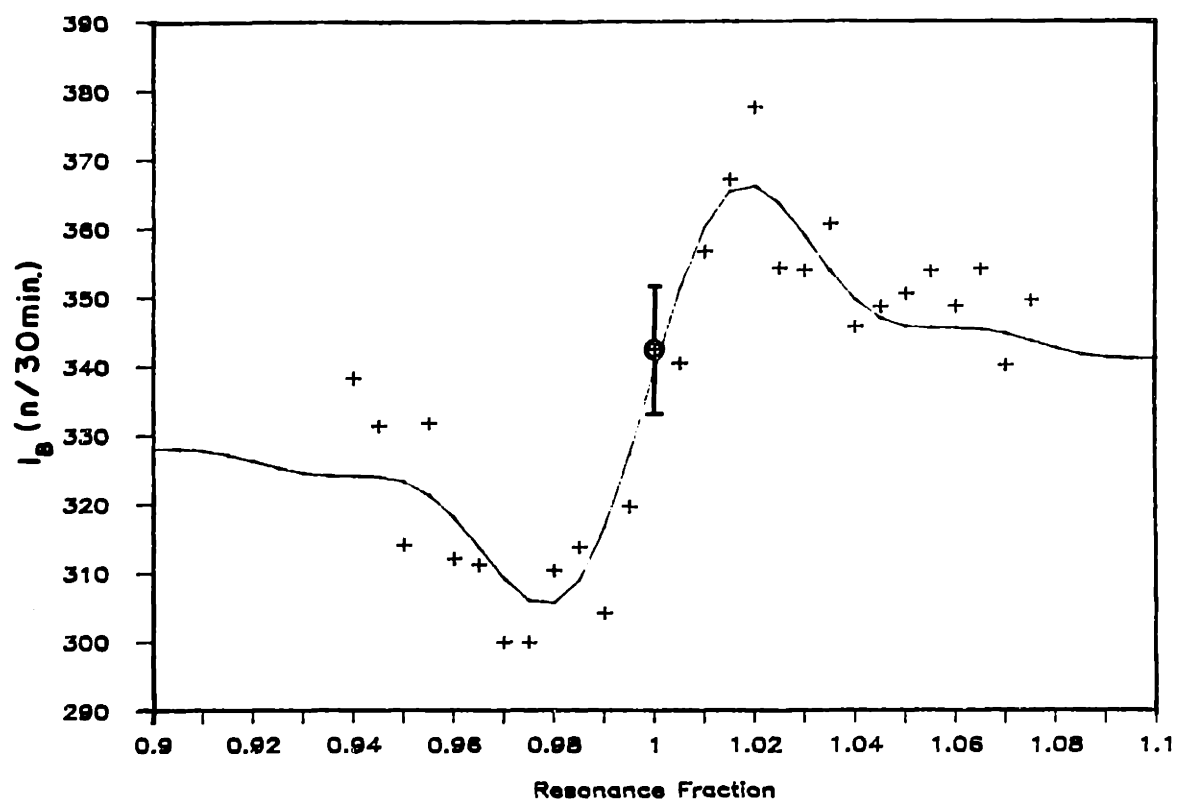


Fig.(5.3) Results, as in Fig.(5.2), but for measurements taken at the zero field half intensity position ($n=24.75$).

NSPR Chisq. on data

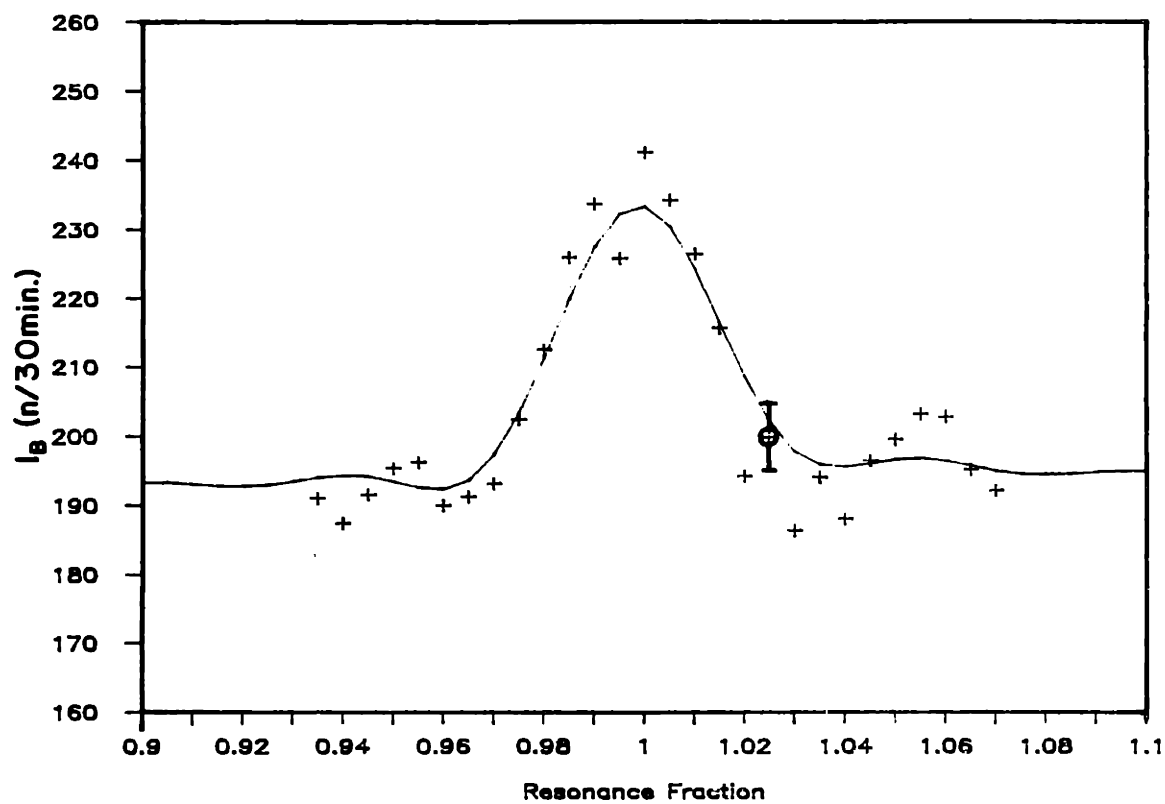


Fig.(5.4) Results, as in Fig.(5.2), but for measurements taken at the zero field minimum intensity position ($n=25.00$). Seven field scans were averaged in this data package.

flux on the crystal). A small monitor counter located in the incident beam was used to monitor changes of incident flux during all of the scans. The horizontal axis represents the applied magnetic field and has been normalized so that 1 corresponds to the expected resonance field value. The error bars in each figure indicate the typical measured standard deviation of the mean (internal error) for data obtained in that package. Two observations can be made about these measured deviations: they generally range from between 1 to 1.5 times the deviation one would expect from purely statistical fluctuations (external error) and secondly the measured deviations in some scans appear larger on the extreme ends of the field scan pattern. No definitive explanation of this second trend has been found, but it may be related to the small changes in temperature which occur around the crystal and are associated with the scanning method. It should be mentioned that the baseline intensity (that is the intensity far away from the resonance peak) is different for each of these scans because they correspond to different pendellösung fringe positions. If we could scan far enough (high or low) in field this baseline intensity should coincide with the zero field pendellösung intensity at that wavelength.

The solid line curves drawn through the data points in each figure were obtained by use of the NSPR intensity function (3.3.4). These are the "best fit" curves determined by a procedure discussed in the next section. We make use of

them here simply to point out that the NSPR field scan data is, qualitatively speaking, in good agreement with the predictions of NSPR theory. Another observation is that the resonance data display slight asymmetries in the baseline on either side of the central structure and this is reflected in the theory curves. This behavior is due to a slight error in adjusting the pendellösung phase (at zero field) to be at the exact fringe positions listed above. The resonance peak shape is very sensitive to this phase; in terms of Bragg angle the asymmetry seen in Fig.(5.2) reflects a mis-positioning of the silicon crystal angle of approximately 0.006 degrees. It is fair to say that the data illustrated in these three figures, as well as all the packages taken in this experiment, demonstrate the expected resonant enhancement of SO scattering.

Section 5.3 - Quantitative Analysis of NSPR Data

The principal result demonstrated in this thesis is a resonant enhancement of SO scattering. This occurs when a pendellösung diffracting neutron is put in a magnetic field of sufficient strength to cause the Larmor precession length of the neutron magnetic moment to match the pendellösung length. An important feature of this enhancement is that it allows for a measurement of the strength of SO scattering with greater

sensitivity than has been previously possible. In this section we give the results from a series of such measurements, discuss the method of analysis and compare the result with a value derived from first principles.

The measurements utilized in this analysis consist of 14 packages of data, (see Section (5.2) for a discussion on data packages). Each package represents about 80 hours of data collection. The resonance experiments were performed at three different neutron wavelengths as described in Section (5.2). What we have extracted from each data package is a measurements of the ratio of the strengths of S0 to nuclear scattering. This ratio arises quite naturally in the NSPR theory presented in Chapter III. We have given this ratio the name θ_{s0} .

The ratio, expressed in (4.1.4) is represented as

$$\theta_{s0} = \frac{\frac{\mu}{2} \{Z - f(G)\} \left(\frac{a^2}{mc^2} \right) \cot \theta_B}{b_{\text{silicon}}} \quad (5.3.1)$$

where the scattering length $b_{\text{silicon}} = 0.41534(10) \times 10^{-12} \text{ cm}$.

It is seen that this ratio depends on the Bragg angle, on the charge number of the scattering atom, and on the atomic scattering form factor $f(G)$. These scattering form factors are listed in tables[1] and as is indicated, for a particular atom, they depend only on the magnitude of the scattering vector (G) .

In order to determine the above ratio, the method of least-squares was used to fit the resonance function (3.3.4) to the averaged magnetic field scan data of each package. The general technique, which is discussed in Bevington[2], involves finding the "best fit" of (3.3.4) to the data by a Chi-squared minimization. The resonance function (3.3.4) is expressed as a function of one variable, the normalized magnetic field, and three parameters: the baseline intensity (the minimum intensity measured in the zero field wavelength pendellösung scan), the pendellösung oscillation height (the measured difference in intensity between the minimum and maximum point in the pendellösung scan), and θ_{so} .

A search of the resultant three-parameter space is carried out in order to minimize the value of Chi-squared, but in such a way that the intensity parameters remain consistent with measured intensities. The search procedure begins by using a computer "spread sheet" program which allows for a visual monitoring of the fit. After a satisfactory minimum in Chi-squared has been determined by this method, a fully computerized parameter-grid search is performed. For all data packages the results from these two methods were found to be in close agreement. Once the "best fit" is determined, the computer program performs a parabolic interpolation at the minimum of Chi-squared along each axis in parameter space.

The degree of curvature at the minimum provides an estimate of the uncertainty in the "best fit" value of each parameter.

The parameter of primary importance in our analysis is θ_{SO} . In Fig. (5.5) we have divided this ratio by the cotangent of the Bragg angle (in order to remove the wavelength dependence) and displayed the results for all 14 data packages. The figure is divided into three sections and from left to right are presented six measurements taken at the minimum, five at the inflection point, and three at the maximum in the pendellösung fringe pattern. A mean (the dashed line) of 142.2 is obtained by considering each of the normalized values to have equal weight. The uncertainty in the mean (standard error) is calculated from the individual deviations from the mean and again taking each deviation to have equal weight. Thus a final value for the normalized ratio is $142.2 \pm (2.5)$, and therefore the error as evaluated by this method is about 1.8%. This result maybe compared to the value calculated from (5.3.1) using the silicon (111) reflection and Shull's value for the silicon nuclear scattering length (see Section (2.4)) which gives 121.00. The measured ratio (142.2) implies for a Bragg angle of 8.75 degrees that nuclear scattering is 108.2 times stronger than SO scattering. The difference between the two values indicates that the measured value of the strength of SO scattering is about 17.8 % larger than what is expected.

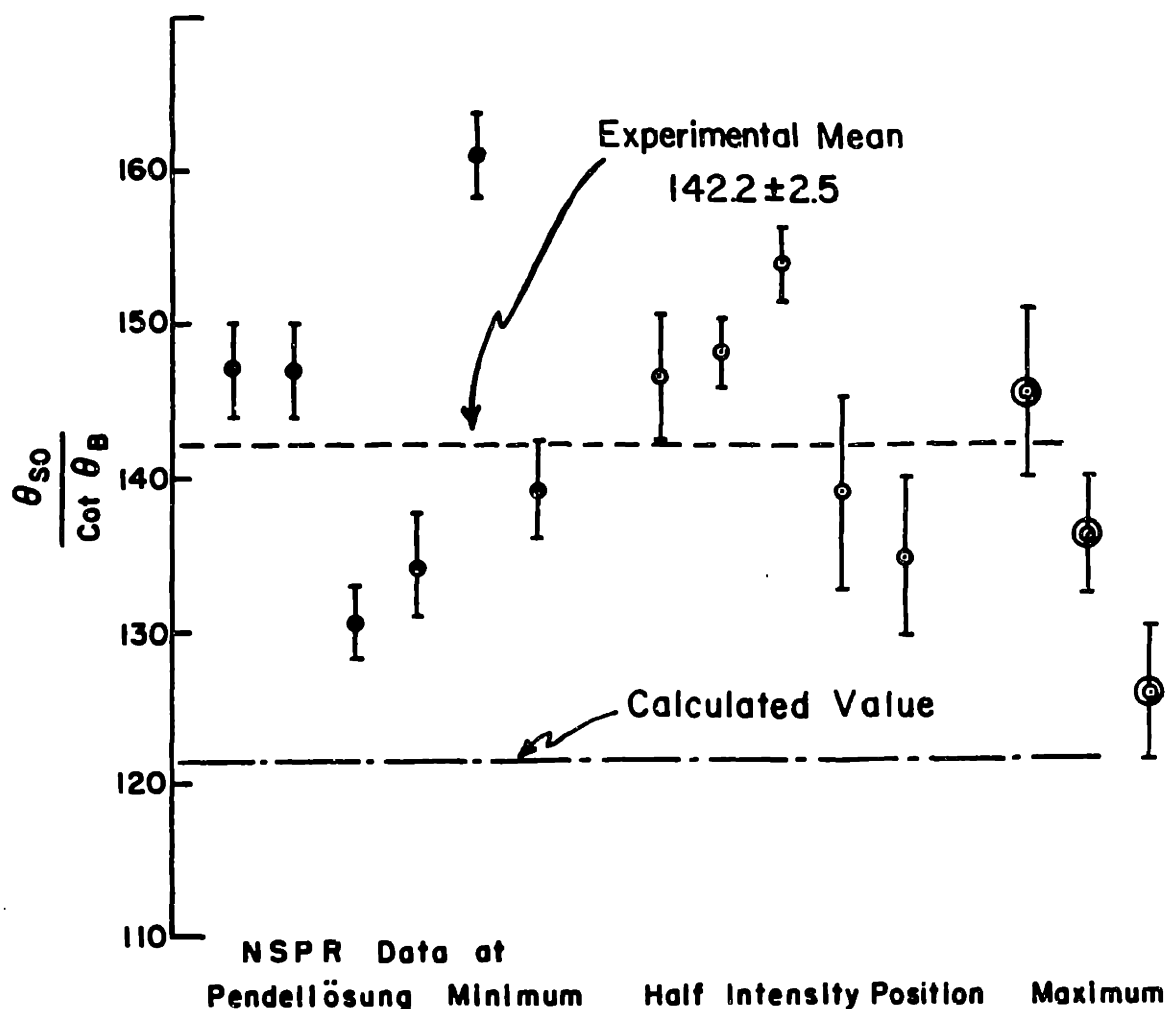


Fig.(5.5) Results for the measurement of the ratio of spin-orbit to nuclear scattering for the silicon (111) reflection. Fourteen data packages, representing about 1200 hours of NSPR field scanning are displayed. The vertical axis is the ratio normalized to remove wavelength dependence.

Three groups of data are presented as well as the weighted average for all 14 packages. A value for this quantity derived from an independent first principles calculation is given for comparison with experiment. The errors are discussed in the text.

This discrepancy between experiment and theory is not yet resolved. Two classes of effects may be responsible for this difference. At this writing the first group, which may best be called experimental uncertainty, is the more likely possibility. There at least four areas worthy of consideration.

1) Our measurement of the absolute pendellösung oscillation height may be in error. It has proved quite difficult to access this quantity with great precision because of the nature of the narrow band spectrometer we have used (see Section (4.2)). An accurate assessment of this parameter is important because the change of NSPR intensity scales linearly with it. Underestimating its size implies an overestimate in the sought for ratio as obtained by the curve fitting procedure. The stated discrepancy could only be accounted for by this factor if the height were underestimated by about 20% and this is very unlikely.

2) Simultaneous reflections are quite possible in silicon at around this wavelength. It is quite possible that such a reflection would affect SO scattering in a different way than it would affect nuclear scattering. This possibility deserves careful consideration.

3) Higher order wavelength components in the beam incident on the silicon crystal are known to exist. Efforts were made to limit this contamination in the experiment, but a contribution

from this effect could help in explaining the discrepancy.

4) Attenuation of the neutron beam inside a silicon crystal of this thickness is usually neglected in calculations. However, it is important to keep in mind the scale of the discrepancy. We are looking for a 10-20% effect in a phenomenon that is itself less than 1% as strong as real nuclear scattering. A preliminary calculation suggests that neutron attenuation in the silicon crystal will affect the measurement of S0 scattering by at least a few percent.

The second category of effects might be called "really interesting possibilities". One such possibility is that there may be another (or other) imaginary (i.e. out of phase with nuclear scattering) interactions which are mediated through the neutron magnetic moment. What is needed to fully account for the discrepancy is an interaction of this same type, which has the same sign as S0 scattering, but is 5-10 times weaker. Both of these categories of effects are being studied at the present time.

End Notes

1. International Tables for X-Ray Crystallography, Vol. III, Pg.202, edited by C.H.Macgillavry & G.D.Rieck, (The Kynoch Press, Birmingham, England, 1962).
2. P.R.Bevington, Data Reduction and Error Analysis for the Physical Sciences, Chapter 11, (McGraw-Hill Book Co., New York, 1969).

Chapter VI -**Summary**

The purpose of this thesis has been to study the influence of spin-orbit (SO) scattering in the perfect crystal diffraction of thermal neutrons. The investigation may be divided into three areas. First, we have extended the dynamical diffraction description of neutron propagation in perfect crystals to include the SO interaction along with the neutron-nuclear interaction. It is shown that these two effects are coupled by the influence of an external magnetic field and the prediction of a resonant enhancement of SO scattering is made. Second, this enhancement, called Neutron Spin-Pendellösung Resonance (NSPR), is demonstrated to exist in a series of experiments using unpolarized neutrons, where the Bragg diffracted neutron intensity is studied with variation in the strength of an externally applied magnetic field. Finally, the results of these NSPR field scan measurements are used for a precision determination of the strength of SO scattering in silicon.

The results that have been accomplished in each of these categories are summarized as follows. The three-potential description of the crystal lattice with externally applied magnetic field is given in Section (2.3) and it is shown that this potential leads to a modified form for the T.T. (or master) equations of diffraction (3.2.7). The solutions to these equations, in the case of exact Bragg incident radiation

are given in (3.2.8) and from these solutions the resonant behavior of the Bragg diffracted intensity (3.3.4) is predicted. An alternative derivation of the solutions (3.2.8) is then given in which the NSPR crystal diffraction problem is re-cast into the quantum mechanical problem of a spin in a magnetic field. From this perspective the solutions are seen to arise quite naturally and in addition some extensions of the NSPR theory may be inferred.

On the experimental side, a comprehensive description of the experimental arrangement is given in Chapter IV, and the results of NSPR field scans are presented in Section (5.2). Here it is seen that good qualitative agreement exists between theory and experiment. The results of a quantitative analysis on the entire series of NSPR measurements, representing about 1200 hours of field scanning are given in Fig. (5.5). In this figure the measured ratios of the strength of SO to nuclear scattering (normalized to remove wavelength dependence) for each of the 14 data packages are shown. The mean value of this ratio for all packages is found to be $(142.2 \pm 2.5) \times 10^{-5}$ and this result is compared to that of a first principles calculation for the same quantity. The measured mean ratio implies for a Bragg angle of 8.75 degrees (typical in these experiments), that nuclear scattering is 108.2 times larger than SO scattering in silicon for the (111) reflection. The overall precision for this measurement, estimated from the quoted error, is 1.8% and this may be compared to the only

previous measurements, performed by a completely different method, where the precision was about 40%.

The measured ratio is about 17% larger than what is predicted by a first principles evaluation for this quantity using (5.3.1) where the strength of SO scattering is expressed in terms of an accepted value for the silicon atomic scattering form factor (a measure of the charge density in the atom). This discrepancy between theory and experiment may result from some source of experimental error or possible from a previously unknown interaction, the presence of which has been revealed by the enhanced sensitivity afforded by the NSPR technique.

Acknowledgements

I would first of all like to thank my parents for their encouragement and support and for giving me the freedom to do what I wanted to. Secondly I am grateful to have had the privilege of working with and learning from Professor Clifford Shull. His example as a scientist and constant encouragement were of immeasurable benefit to my graduate education. I have also had many valuable exchanges with Professor Michael Horne, whose insistence on pursuing the essential elements in a physical problem will long remain a model for my work. Professor Herbert Bernstein provided an important contribution to this work, I thank him for this and for the many inspiring discussions we have had. I would also like to acknowledge Professor Anton Zeilinger for his expert assistance with all the experiments that I have participated in while working at the M.I.T. Neutron Diffraction Laboratory. It has been my great good fortune to have been associated with this very special group of scientists over the past 5 years.

I am also grateful for the ever present support of my wife, Lois, especially for the help she has provided in assembling this thesis. Marv Goldschmitt has provided friendship, understanding, and a computer which made the data analysis and word processing for this thesis much easier. The people at the M.I.T. Nuclear Reactor have been extremely helpful. It would take far too much space to thank them each personally, but I appreciate the contribution they have made to my work. I would especially like to thank Paul Menadier for advising me on some technical problems and for the many spare parts he has collected that became integral components of the experiment. One last staff member at the reactor who I am grateful to for many reasons is Gordon Kohse.

Finally, I would like to thank Professor Thomas Greytak for the loan of his computer and plotter, and Professor Robert Birgeneau's group for the use of the power supply that made the magnet sweeps possible.

Biographical Note

The author was born in Ellenville, New York on September 8, 1951 to Sam and Lillian Finkelstein. After graduation from Ellenville High School he attended S.U.N.Y. at New Paltz receiving his B.S. in physics in 1977. One year of study at the University of Illinois was followed by several years as a staff member at the Research Division of Raytheon Company. In 1982 he entered M.I.T. as a graduate student in physics. He married a fellow student, Lois Pollack, in 1985. He has accepted a position as a staff scientist at the Cornell High Energy Synchrotron Source (CHESS).